Benjamin Wuitz, BSc

Regularization of nearly singular integrals for the Boundary Element Mehtod

MASTER'S THESIS

to achieve the university degree of

Diplom-IngenieurIn

Master's degree programme: Civil Engineering and Structural Engineering

submitted to

Graz University of Technology

Supervisor

Priv.-Doz. Dipl.-Ing. Dr.techn. Christian Dünser

Institute of Structural Analysis

Graz, October 2018

AFFIDAVIT

I declare that I have authored this thesis independently, that I have not used other than the declared sources/resources, and that I have explicitly indicated all material which has been quoted either literally or by content from the sources used. The text document uploaded to TUGRAZonline is identical to the present master's thesis.

Graz, October 2018 _____

Abstract

The master's thesis deals with the regularization of the nearly singular Somigliana Displacement and Stress Identities for the Boundary Element Method (BEM). The involved effects on interior results obtained for points close to the boundary are discussed on the basis of four test examples. For this purpose a BEM-application for 3-D isotropic elasticity problems was developed. It includes algorithms for the numerical evaluation of the Displacement Boundary Integral Equation and the standard and regularized formulations of the Somigliana Displacement and Stress Identities. The relevant integral equations and the methods used to implement the BEM are discussed and explained in detail. Finally, numerically computed displacements and stresses of the test examples were discussed and compared with either an analytical or a reference solution. It was found that interior results obtained from the regularized formulations of the Somigliana Identities are very accurate for points very close to the boundary and they do not require special integration schemes for their numerical evaluation.

Zusammenfassung

Die vorliegende Masterarbeit behandelt die Regularisierung der quasi singulären Somigliana Integralgleichungen für Verformungen und Spannungen in der Randelementmethode (REM, engl. Boundary Element Method oder kurz BEM). Die damit verbunden Auswirkungen auf im geringen Abstand vom Rand berechnete Resultate im Inneren eines Gebietes werden anhand von vier Testbeispielen erörtert. Dafür wurde eine REM-Anwendung für dreidimensionale, isotrope Elastizitätsprobleme entwickelt, die Algorithmen für die Auswertung der Randintegralgleichung und der allgemeinen sowie regularisierten Somigliana Integralgleichungen enthält. Schließlich werden die numerisch berechneten Verformungen und Spannungen der Testbeispiele ausgewertet und mit analytischen Lösungen beziehungsweise Referenzlösungen verglichen. Dabei stellte sich heraus, dass mit den regularisierten Somigliana Integralgleichungen sehr genaue Resultate in der Nähe des Randes erzielt werden können und dafür keine speziellen numerischen Integrationsmethoden notwendig sind.

Contents

List of Figures

List of Tables

1 Preliminaries

1.1 Introduction to the Boundary Element Method

Nowadays numerical methods such as the Boundary Element Method (BEM) have a widespread range of applications and they are very powerful tools in engineering. BEM can be applied to many physical problems, e.g. elastostatics, elastodynamics and potential problems just to name a few. The approach of the BEM is that the solutions of the governing differential equations, which describe physical problems in terms of boundary values, are satisfied exactly inside a domain, whereas boundary conditions are approximated. This approach was first proposed by Trefftz in 1926. It allows that only the boundary of the domain has to be discretized for numerical evaluation and since the solutions also satisfy conditions at infinity, infinite domains can be handled simply, too. The fundamental solutions which satisfy the differential equations should be as simple as possible, whereby those involving concentrated loads or sources are proven to be the most appropriate functions. These functions have singularities and thus requiring special consideration [3]. While many mathematical approaches which are applied in modern BEM-applications have been proposed earlier, the origin of the BEM is dating back into the 1960's when the direct BEM was developed for potential problems and elastostatics based on Green's and Somigliana's Identity, respectively. Since then many well-known researchers have been devoted themselves to steadily improve the BEM and to extend its field of applications to many other physical problems such as electrodynamics and fluid mechanics. Special attention was given to cope with the singularities that appear in the integral equations [6]. Still nowadays the development of the BEM is an ongoing process and we can expect that it will become even more efficient in future.

1.2 Introduction into this work

Singularities of the fundamental solutions may be the main difficulty the BEM has to deal with, as they can significantly influence the accuracy of numerical results. Regularization of the governing integral equations is one approach to mitigate these adverse impacts and to achieve accurate results. The regularization of nearly singular integrals of the Somigliana Displacement and Stress Identities [11] for 3-D isotropic elasticity problems is the topic of the present work. These regularizations make use of Rigid Body Motion to regularize the nearly singular Somigliana Displacement Identity (SDI) and assumes a low-order iso-stress state based on a linear displacement field in order to regularize the nearly singular Somigliana Stress Identity (SSI). These approaches require a point on the boundary, the so called regularizing point, for which displacements, strains and stresses have to be known from the solution of the Boundary Integral Equation (BIE).

The aim of the present work was to develop a BEM-application in order to study if and how regularization of the nearly singular Somigliana Displacement and Stress Identities influence the behaviour of the corresponding results. This also implies the knowledge of boundary results. They were computed using the direct BEM with collocation. The results are boundary displacements and tractions obtained from the usual displacement form of the BIE which can be derived from the SDI by a limiting process. Rigid Body Motion was applied to evaluate the arising strong singular integral in sense of the Cauchy principal value. Boundary stresses were computed locally from the boundary displacements and tractions using Hook's law. Based on the boundary results, interior results were determined with the regularized forms of the nearly singular SDI and SSI. Also the non-regularized (standard) forms of the Somigliana Identities, for which the concept of element subdivision is applied to cope with

singularities, were used to compute results in order to compare them with the ones obtained from the regularized formulation of the nearly singular Somigliana Identities. Finally, test examples for which either an analytical solution or a reference solution exists were set up to verify the implemented algorithms. Thus, the BEM- application not only contains codes for numerical evaluation of the different integral equations (main processing), but also for pre-processing (input and mesh generation) and post-processing (displaying results). The results of the test examples were then used to discuss and explain the difference between the standard and regularized formulations of the SDI and SSI and to show how regularization of the nearly singular integrals of the SDI and SSI influences and improves results.

As it is essential to give a broad insight in the topic, the relevant integral equations are discussed in this work whereas emphasis is given to the regularization of the nearly singular SDI and SSI. Furthermore, also knowledge of the discretization of the integral equations and background informations about the concepts used to implement the BEM-application are important and thus explained in this work too. That should provide a fundamental understanding to follow the discussions of results in the test examples.

1.3 Annotations

The BEM-application developed for this work is implemented as Matlab®-code [10]. It became part of the EduBEM-application of the Institute of Structural Analysis at Graz University of Technology. It was the basis of the development of the application as it already provided implementations for 2-D isotropic elasticity problems. Thus, many of the developed algorithms were implemented in analogy to the already existing codes. The BEM-application also make use of a software called GMSH [7] in post-processing to enable scalar, vector and tensor field visualization which are displayed in this work as well.

The equations provided in this work are written in vector-matrix notation. Therefore, bold capital Latin letters (e.g. $\mathbf{T}$) are used to denote matrices or tensors and bold lower-case Latin letters (e.g. $\mathbf{t}$) refers to vectors. Bold Greek letters (e.g. $\boldsymbol{\sigma}$) denotes either vectors, matrices or tensors and therefore will be described in the text whether they are vectors, matrices or tensors. Normal letters no matter if they are Latin or Greek ones refer to scalars or variables. Exceptions from these rules will be explained in the text.

This work was written with LaTeX [9]. The sketches and drawings were prepared with the CAD-software ALLPLAN [1].

2 Integral equations in elasticity

2.1 The Displacement Boundary Integral Equation in elasticity

Following equation represents the usual form of the Somigliana Displacement Identity (SDI) to evaluate displacements $\mathbf{u}(p)$ at points p in the interior of a domain Ω. It can be derived by applying Betti's Theorem as explained in Reference [3]. A more general approach deriving the SDI is applying the divergence theorem and Green's symmetric identity to the differential equation for elasticity.

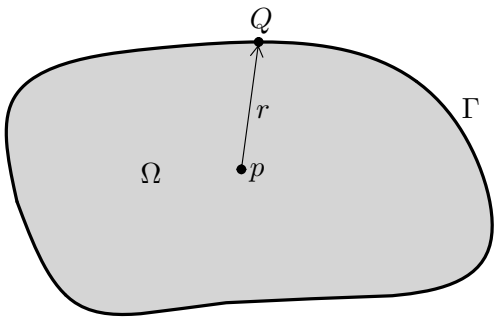

Fig. 1: arbitrary domain for the BEM

$$\mathbf{u}(p) = \int_\Gamma \mathbf{U}(p,Q)\mathbf{t}(Q)d\Gamma - \int_\Gamma \mathbf{T}(p,Q)\mathbf{u}(Q)d\Gamma \tag{1}$$

The 2-D SDI has a weak singularity of type $(ln(\frac{1}{r}))$ in the displacement kernel $\mathbf{U}(p,Q)$ and a strong singularity of type $(\frac{1}{r})$ in the traction kernel $\mathbf{T}(p,Q)$. In 3-D elasticity the weak singularity is of type $(\frac{1}{r})$ and the strong singularity is of type $(\frac{1}{r^2})$, where r denotes the distance between source point p and field point Q as can be seen in Figure 1.

If the source point p is moved towards the boundary Γ $(p \to P)$ a limiting process has to be performed as outlined in Reference [3]. Then the following Boundary Integral Equation (BIE) arises.

$$c\mathbf{I}\mathbf{u}(P) = \int_\Gamma \mathbf{U}(P,Q)\mathbf{t}(Q)d\Gamma - \oint_\Gamma \mathbf{T}(P,Q)\mathbf{u}(Q)d\Gamma \tag{2}$$

where $\mathbf{I}$ is the identity matrix (2x2 for 2-D and 3x3 for 3-D elasticity problems) and c is the limiting value or free term:

$$\begin{aligned} c &= \frac{1}{2} && \text{... if P is located on a smooth surface} \\ c &= 1 - \frac{\gamma}{2\pi} && \text{... in 2-D if P is located on a corner} \\ c &= 1 - \frac{\gamma}{4\pi} && \text{... in 3-D if P is located on a corner} \end{aligned} \tag{3}$$

where γ is the external angle of the corner.

Assuming $c = 1$ in Equation (2), Equation (1) for points p inside the domain Ω will arise and thus Equation (2) is a general form representing the SDI. It is the usual displacement form of the BIE using the Cauchy principal value of the strong singular integral. In order to solve Equation (2), either boundary displacements $\mathbf{u}(Q)$ (Dirichlet boundary conditions) or boundary tractions $\mathbf{t}(Q)$ (Neumann boundary conditions) have to be known, whereas the other boundary condition is unknown and has to be evaluated by solving the BIE.

2.2 Somigliana Identities for interior results

Supposing that both boundary tractions $\mathbf{t}(Q)$ and boundary displacements $\mathbf{u}(Q)$ are already known from solving the BIE, displacements $\mathbf{u}(p)$ at any interior point p can be evaluated using the Somigliana Displacement Identity (SDI) from Equation (1). Recap:

$$\mathbf{u}(p) = \int_\Gamma \mathbf{U}(p,Q)\mathbf{t}(Q)d\Gamma - \int_\Gamma \mathbf{T}(p,Q)\mathbf{u}(Q)d\Gamma \tag{4}$$

By differentiation of Equation (4) the well known Somigliana Stress Identity (SSI) for computing stresses $\boldsymbol{\sigma}(p)$ at interior points p arise [3].

$$\boldsymbol{\sigma}(p) = \int_\Gamma \mathbf{S}(p,Q)\mathbf{t}(Q)d\Gamma - \int_\Gamma \mathbf{R}(p,Q)\mathbf{u}(Q)d\Gamma \tag{5}$$

where $\boldsymbol{\sigma}(p)$ is a pseudo-stress vector. $\mathbf{S}(p,Q)$ and $\mathbf{R}(p,Q)$ are the derived kernels, $\mathbf{S}(p,Q)$ of order $(\frac{1}{r})$ and $\mathbf{R}(p,Q)$ of order $(\frac{1}{r^2})$ in 2-D and $(\frac{1}{r^2})$ and $(\frac{1}{r^3})$ in 3-D, respectively. Thus, they are indicated to be strongly singular ($\mathbf{S}(p,Q)$) and hyper singular ($\mathbf{R}(p,Q)$).

The application of these formulations for numerically computing interior results has its drawbacks. As the interior point p is moved very close towards the boundary, an element subdivision technique has to be applied (see Sections 3.3.3 and 3.4). However, due to reasons mentioned in those sections, results become unacceptable inaccurate when the points p are located at a certain proximity to the boundary. A better approach to obtain accurate interior results near the boundary is regularization, which will be discussed in Sections 2.3 and 3.5.

2.3 Regularization of the Somigliana Identities for interior results

In what follows regularization of the nearly singular Somigliana Displacement and Stress Identities for interior results will be described. The idea is to eliminate the influence of the strong and hyper singularities either by applying Rigid Body Motion in case of the SDI or by taking the tangential expansions of all boundary conditions at point P for the SSI. Regularization of the nearly singular Somigliana Identities requires a regularization point P. It is the nearest point at the boundary Γ to the point p in the interior of the domain Ω as shown in Figure 2. At this point stresses, strains and displacements have to be evaluated from boundary results which are obtained by solving the BIE. Detailed explanations regarding regularization of the Somigliana Identities can be found in References [4] and [5].

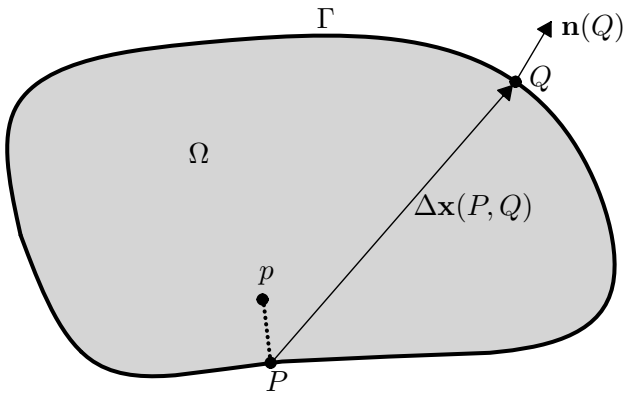

Fig. 2: arbitrary domain for regularization

2.3.1 Regularization of the Somigliana Displacement Identity for finite domains

Starting from the SDI in Equation (4) boundary conditions of a constant displacements field can be assumed, that is, applying Rigid Body Motion. Hence, no tractions arise ($\mathbf{t}(Q) = 0$) and thus the integral with the displacement kernel $\mathbf{U}(p, Q)$ vanishes. Following equation will arise.

$$\mathbf{u}(p) = -\int_{\Gamma} \mathbf{T}(p, Q)\mathbf{u}(Q)d\Gamma \tag{6}$$

As all displacements are constant due to Rigid Body Motion ($\mathbf{u}(Q) = \mathbf{u}(p) = \mathbf{u}(P) = const.$), Equation (6) can be rearranged which yields:

$$0 = \mathbf{u}(P) + \mathbf{u}(P)\int_{\Gamma} \mathbf{T}(p, Q)d\Gamma \tag{7}$$

Then, adding Equation (7) to the SDI in Equation (4) and rearranging again will result in:

$$\mathbf{u}(p) = \mathbf{u}(P) + \int_{\Gamma} \mathbf{U}(p, Q)\mathbf{t}(P)d\Gamma - \int_{\Gamma} \mathbf{T}(p, Q)[\mathbf{u}(Q) - \mathbf{u}(P)]d\Gamma \tag{8}$$

which is the regularized form of the SDI for finite domains Ω. In Equation (8) $\mathbf{u}(P)$ denotes the regularizing displacement at P. Furthermore, the integral with the displacement kernel $\mathbf{U}(p, Q)$ remains with a weak singularity.

2.3.2 Regularization of the Somigliana Displacement Identity for infinite domains

In case of infinite domains an additional integral over the boundary Γ_∞ at infinity has to be considered when applying Rigid Body Motion to the SDI. Thus, Equation (6) is extended by this integral which gives:

$$\mathbf{u}(p) = -\int_{\Gamma} \mathbf{T}(p, Q)\mathbf{u}(Q)d\Gamma - \int_{\Gamma_\infty} \mathbf{T}(p, Q)\mathbf{u}(Q)d\Gamma_\infty \tag{9}$$

Again assuming constant displacements and executing the same scheme as explained above will result in following equation.

$$0 = \mathbf{u}(P) + \mathbf{u}(P) \int_{\Gamma} \mathbf{T}(p,Q) d\Gamma + \mathbf{u}(P) \int_{\Gamma_\infty} \mathbf{T}(p,Q) d\Gamma_\infty \tag{10}$$

Then the regularized SDI for infinite domains will be found by adding the SDI in Equation (4) to Equation (10):

$$\mathbf{u}(p) = \mathbf{u}(P) + \int_{\Gamma} \mathbf{U}(p,Q)\mathbf{t}(P) d\Gamma - \int_{\Gamma} \mathbf{T}(p,Q)[\mathbf{u}(Q) - \mathbf{u}(P)] d\Gamma + \mathbf{u}(P) \int_{\Gamma_\infty} \mathbf{T}(p,Q) d\Gamma_\infty \tag{11}$$

The additional integral over the boundary Γ_∞ at infinity can be solved analytically by assuming an infinite extended auxiliary boundary surface Γ_∞ to which Rigid Body Motion may be applied. For example Γ_∞ could be a circle in 2-D or a sphere in 3-D both of radius R which approaches infinity as outlined in Reference [3]. The analytical solution of that integral is:

$$\int_{\Gamma_\infty} \mathbf{T}(p,Q) d\Gamma_\infty = -\mathbf{I} \tag{12}$$

where $\mathbf{I}$ is the identity matrix (2x2 in 2-D and 3x3 in 3-D elasticity).

2.3.3 Regularization of the Somigliana Stress Identity for finite domains

In order to regularize the SSI a low-order iso-stress state is assumed [5]. It is a constant stress field $\boldsymbol{\sigma}^*$ with corresponding boundary traction $\mathbf{t}^*$ based on a linear displacement field $\mathbf{u}^*$. Applying this to the SSI in Equation (5) yields:

$$\boldsymbol{\sigma}(p) = \int_{\Gamma} \mathbf{S}(p,Q)\mathbf{t}^*(Q) d\Gamma - \int_{\Gamma} \mathbf{R}(p,Q)\mathbf{u}^*(Q) d\Gamma \tag{13}$$

Due to the assumption of constant stresses ($\boldsymbol{\sigma}^* = \boldsymbol{\sigma}(p) = \boldsymbol{\sigma}(P) = \boldsymbol{\sigma}(Q)$), Equation (13) can be rewritten which yields:

$$0 = \boldsymbol{\sigma}(P) - \int_{\Gamma} \mathbf{S}(p,Q)\mathbf{t}^*(Q) d\Gamma + \int_{\Gamma} \mathbf{R}(p,Q)\mathbf{u}^*(Q) d\Gamma \tag{14}$$

Now, the regularized SSI will arise by adding Equation (14) to the SSI in Equation (5):

$$\boldsymbol{\sigma}(p) = \boldsymbol{\sigma}(P) + \int_{\Gamma} \mathbf{S}(p,Q)[\mathbf{t}(Q) - \mathbf{t}^*(P)] d\Gamma - \int_{\Gamma} \mathbf{R}(p,Q)[\mathbf{u}(Q) - \mathbf{u}^*(P)] d\Gamma \tag{15}$$

where $\boldsymbol{\sigma}(p)$ and the so called regularizing stress $\boldsymbol{\sigma}(P)$ are pseudo-stress vectors. $\boldsymbol{\sigma}(P)$ may be evaluated from the boundary tractions and displacements at P.

As constant stresses with a corresponding linear displacement field were assumed, the linearised terms $\mathbf{t}^*(Q)$ and $\mathbf{u}^*(Q)$ may be evaluated as following:

$$\begin{aligned} \mathbf{t}^*(Q) &= \boldsymbol{\sigma}_c^*(P)\mathbf{n}(Q) \\ \mathbf{u}^*(Q) &= \mathbf{u}(P) + \frac{\partial \mathbf{u}(P)}{\partial \mathbf{x}} \Delta\mathbf{x}(P,Q) \end{aligned} \tag{16}$$

where $\boldsymbol{\sigma}_c^*(P)$ is the corresponding Cauchy-stress tensor of the pseudo-stress vector $\boldsymbol{\sigma}(P)$ and $\frac{\partial \mathbf{u}(P)}{\partial \mathbf{x}}$ is the displacement gradient at the regularization point P (see also Section 2.3.5). Furthermore, $\mathbf{n}(Q)$ denotes the outward normal at field point Q and $\Delta\mathbf{x}(P,Q)$ refers to the distance between point P and Q (see Figure 2).

2.3.4 Regularization of the Somigliana Stress Identity for infinite domains

Two supplementary integrals which extend over the boundary Γ_∞ at infinity arise when regularizing the SSI for infinite domains. Considering these integrals in Equation (13) yields to:

$$\begin{aligned} \boldsymbol{\sigma}(p) = \int_\Gamma \mathbf{S}(p,Q)\mathbf{t}^*(Q)d\Gamma + \int_{\Gamma_\infty} \mathbf{S}(p,Q)\mathbf{t}^*(Q)d\Gamma_\infty - \\ \int_\Gamma \mathbf{R}(p,Q)\mathbf{u}^*(Q)d\Gamma - \int_{\Gamma_\infty} \mathbf{R}(p,Q)\mathbf{u}^*(Q)d\Gamma_\infty \end{aligned} \tag{17}$$

Assuming constant stresses $\boldsymbol{\sigma}^* = \boldsymbol{\sigma}(p) = \boldsymbol{\sigma}(P) = \boldsymbol{\sigma}(Q)$ and revising Equation (17) in the same manner as introduced above yields to:

$$\begin{aligned} 0 = \boldsymbol{\sigma}(P) - \int_\Gamma \mathbf{S}(p,Q)\mathbf{t}^*(Q)d\Gamma - \int_{\Gamma_\infty} \mathbf{S}(p,Q)\mathbf{t}^*(Q)d\Gamma_\infty + \\ \int_\Gamma \mathbf{R}(p,Q)\mathbf{u}^*(Q)d\Gamma + \int_{\Gamma_\infty} \mathbf{R}(p,Q)\mathbf{u}^*(Q)d\Gamma_\infty \end{aligned} \tag{18}$$

Finally, the regularized form of the SSI for infinite domains can be obtained by adding Equation (18) to the SSI in Equation (5) which is:

$$\begin{aligned} \boldsymbol{\sigma}(p) = \boldsymbol{\sigma}(P) + \int_\Gamma \mathbf{S}(p,Q)[\mathbf{t}(Q) - \mathbf{t}^*(Q)]d\Gamma - \int_{\Gamma_\infty} \mathbf{S}(p,Q)\mathbf{t}^*(Q)d\Gamma_\infty - \\ \int_\Gamma \mathbf{R}(p,Q)[\mathbf{u}(Q) - \mathbf{u}^*(Q)]d\Gamma + \int_{\Gamma_\infty} \mathbf{R}(p,Q)\mathbf{u}^*(Q)d\Gamma_\infty \end{aligned} \tag{19}$$

whereby the integrals over the infinite extended boundary Γ_∞ can be solved analytically in the same manner as the integral over Γ_∞, which arise when regularizing the SDI for infinite domains.

The integrals over Γ_∞ and its analytical solutions for 2-D elasticity problems are:

$$\int_{\Gamma_\infty} \mathbf{S}(p,Q)\mathbf{t}^*(Q)d\Gamma_\infty = \frac{1}{8(\nu-1)} \begin{bmatrix} 4\nu-5 & 1-4\nu & 0 \\ 1-4\nu & 4\nu-5 & 0 \\ 0 & 0 & 8\nu-6 \end{bmatrix} \boldsymbol{\sigma}(P) \tag{20}$$

$$\int_{\Gamma_\infty} \mathbf{R}(p,Q)\mathbf{u}^*(Q)d\Gamma_\infty = \frac{E}{8(\nu^2-1)} \begin{bmatrix} 3 & 1 & 0 \\ 1 & 3 & 0 \\ 0 & 0 & 1 \end{bmatrix} \boldsymbol{\epsilon}(P) \tag{21}$$

The analytical solutions of the integrals over Γ_∞ for 3-D infinite domains in elasticity are:

$$\int_{\Gamma_\infty} \mathbf{S}(p,Q)\mathbf{t}^*(Q)d\Gamma_\infty = \frac{1}{15(\nu-1)} \begin{bmatrix} 5\nu-7 & 1-5\nu & 1-5\nu & 0 & 0 & 0 \\ 1-5\nu & 5\nu-7 & 1-5\nu & 0 & 0 & 0 \\ 1-5\nu & 1-5\nu & 5\nu-7 & 0 & 0 & 0 \\ 0 & 0 & 0 & 10\nu-8 & 0 & 0 \\ 0 & 0 & 0 & 0 & 10\nu-8 & 0 \\ 0 & 0 & 0 & 0 & 0 & 10\nu-8 \end{bmatrix} \boldsymbol{\sigma}(P) \tag{22}$$

$$\int_{\Gamma_\infty} \mathbf{R}(p,Q)\mathbf{u}^*(Q)d\Gamma_\infty = \frac{E}{30(\nu^2-1)} \begin{bmatrix} 16 & 2+10\nu & 2+10\nu & 0 & 0 & 0 \\ 2+10\nu & 16 & 2+10\nu & 0 & 0 & 0 \\ 2+10\nu & 2+10\nu & 16 & 0 & 0 & 0 \\ 0 & 0 & 0 & 7-5\nu & 0 & 0 \\ 0 & 0 & 0 & 0 & 7-5\nu & 0 \\ 0 & 0 & 0 & 0 & 0 & 7-5\nu \end{bmatrix} \boldsymbol{\epsilon}(P) \tag{23}$$

In Equations (20) to (23) E and ν are material constants. They are the Young's Modulus E and the Poisson's ratio ν of an isotropic material. $\boldsymbol{\epsilon}(P)$ in Equations (21) and (23) indicates the pseudo-strain vector at the regularizing point P.

2.3.5 Relationship between Cauchy-stress tensor and pseudo-stress vector and between displacement gradient and pseudo-strain vector

The object of this section is to clarify the relation between the Cauchy-stress tensor and the pseudo-stress vector. Moreover, the correlation between the displacement gradient and the pseudo-strain vector will be presented.

The pseudo-stress vector $\boldsymbol{\sigma}(p)$ can be written as follows. It is a vector containing the normal and shear stresses at any point p no matter whether p is on the boundary or not.

$$\begin{aligned} \boldsymbol{\sigma}(p) &= \begin{Bmatrix} \sigma_{xx}(p) \\ \sigma_{yy}(p) \\ \sigma_{xy}(p) = \tau_{xy}(p) \end{Bmatrix} \quad \text{... in 2-D} \\ \boldsymbol{\sigma}(p) &= \begin{Bmatrix} \sigma_{xx}(p) \\ \sigma_{yy}(p) \\ \sigma_{zz}(p) \\ \sigma_{xy}(p) = \tau_{xy}(p) \\ \sigma_{yz}(p) = \tau_{yz}(p) \\ \sigma_{xz}(p) = \tau_{xz}(p) \end{Bmatrix} \quad \text{... in 3-D} \end{aligned} \tag{24}$$

The Cauchy-stress tensor $\boldsymbol{\sigma}_c^*(p)$ gathers the values of the pseudo-stress vector $\boldsymbol{\sigma}(p)$ in a symmetric matrix:

$$\begin{aligned}
\boldsymbol{\sigma}_c^*(p) &= \begin{bmatrix} \sigma_{xx}(p) & \tau_{xy}(p) \\ \text{sym.} & \sigma_{yy}(p) \end{bmatrix} && \dots \quad \text{in 2-D} \\
\boldsymbol{\sigma}_c^*(p) &= \begin{bmatrix} \sigma_{xx}(p) & \tau_{xy}(p) & \tau_{xz}(p) \\ & \sigma_{yy}(p) & \tau_{yz}(p) \\ \text{sym.} & & \sigma_{zz}(p) \end{bmatrix} && \dots \quad \text{in 3-D}
\end{aligned} \tag{25}$$

Pseudo-strain vectors $\boldsymbol{\epsilon}(p)$ contain the normal and shear strains which can be evaluated by using the displacement derivatives at point p. The pseudo-strain vector $\boldsymbol{\epsilon}(p)$ can be written as:

$$\begin{aligned}
\boldsymbol{\epsilon}(p) &= \begin{Bmatrix} \epsilon_{xx}(p) = \frac{\partial u_x(p)}{\partial x} \\ \epsilon_{yy}(p) = \frac{\partial u_y(p)}{\partial y} \\ \gamma_{xy}(p) = \frac{\partial u_x(p)}{\partial y} + \frac{\partial u_y(p)}{\partial x} \end{Bmatrix} && \dots \quad \text{in 2-D} \\
\boldsymbol{\epsilon}(p) &= \begin{Bmatrix} \epsilon_{xx}(p) = \frac{\partial u_x(p)}{\partial x} \\ \epsilon_{yy}(p) = \frac{\partial u_y(p)}{\partial y} \\ \epsilon_{zz}(p) = \frac{\partial u_z(p)}{\partial z} \\ \gamma_{xy}(p) = \frac{\partial u_x(p)}{\partial y} + \frac{\partial u_y(p)}{\partial x} \\ \gamma_{yz}(p) = \frac{\partial u_y(p)}{\partial z} + \frac{\partial u_z(p)}{\partial y} \\ \gamma_{xz}(p) = \frac{\partial u_x(p)}{\partial z} + \frac{\partial u_z(p)}{\partial x} \end{Bmatrix} && \dots \quad \text{in 3-D}
\end{aligned} \tag{26}$$

Finally, the displacement gradient $\frac{\partial \mathbf{u}(P)}{\partial \mathbf{x}}$ gathers the derivatives of the pseudo-strain vector $\boldsymbol{\epsilon}(p)$ in a matrix. To paraphrase that, the displacement gradient contains the derivatives of each component of the displacement vector $\mathbf{u}(p)$ with respect to each coordinate (x, y in 2-D and x, y, z in 3-D, also denoted as $\mathbf{x}$).

$$\begin{aligned}
\frac{\partial \mathbf{u}(p)}{\partial \mathbf{x}} &= \begin{bmatrix} \frac{\partial u_x(p)}{\partial x} & \frac{\partial u_x(p)}{\partial y} \\ \frac{\partial u_y(p)}{\partial x} & \frac{\partial u_y(p)}{\partial y} \end{bmatrix} && \dots \quad \text{in 2-D} \\
\frac{\partial \mathbf{u}(p)}{\partial \mathbf{x}} &= \begin{bmatrix} \frac{\partial u_x(p)}{\partial x} & \frac{\partial u_x(p)}{\partial y} & \frac{\partial u_x(p)}{\partial z} \\ \frac{\partial u_y(p)}{\partial x} & \frac{\partial u_y(p)}{\partial y} & \frac{\partial u_y(p)}{\partial z} \\ \frac{\partial u_z(p)}{\partial x} & \frac{\partial u_z(p)}{\partial y} & \frac{\partial u_z(p)}{\partial z} \end{bmatrix} && \dots \quad \text{in 3-D}
\end{aligned} \tag{27}$$

3 Discretization in 3-D

3.1 Discretization of the Boundary Integral Equation

For practical problems the BIE (Equation (2)) has to be solved numerically as analytical solutions are available only for simple problems. Therefore, the boundary is decomposed using isoparametric elements and the BIE is determined for a limited set of discrete points (nodes) on the boundary then. For this purpose the unit source of the fundamental solution is applied on each node (source point P_i) and its response is evaluated for each element. This method is called the collocation method. Therefore, it is necessary to rewrite Equation (2) as follows. The arising equation is the discretized form of the BIE.

$$\mathbf{cu}(P_i) = \sum_{e=1}^{E}\sum_{n=1}^{N} \Delta\mathbf{U}_{ni}^{e}\mathbf{t}_{n}^{e} - \sum_{e=1}^{E}\sum_{n=1}^{N} \Delta\mathbf{T}_{ni}^{e}\mathbf{u}_{n}^{e} \tag{28}$$

where E and N denotes the total number of elements and the number of nodes of an element e, respectively. $i = 1...I$ whereas I denotes the total number of source points P_i.

The displacement kernel $\Delta\mathbf{U}_{ni}^{e}$ and the traction kernel $\Delta\mathbf{T}_{ni}^{e}$ can be evaluated as follows:

$$\begin{aligned} \Delta\mathbf{U}_{ni}^{e} &= \int_{\Gamma_e} N_n(\xi,\eta)\mathbf{U}(P_i, Q(\xi,\eta))d\Gamma(\xi,\eta) \\ \Delta\mathbf{T}_{ni}^{e} &= \int_{\Gamma_e} N_n(\xi,\eta)\mathbf{T}(P_i, Q(\xi,\eta))d\Gamma(\xi,\eta) \end{aligned} \tag{29}$$

where Γ_e is the element area, ξ and η are the intrinsic coordinates of the reference element and N_n denotes the shape function value n.

In this work quadrilateral elements with linear ansatz order (four local nodes n) and quadrilateral serendipity elements with quadratic ansatz order (eight local nodes n) are used to discretize the boundary Γ of the domain Ω. The relevant reference elements in the ξ,η-coordinate system (intrinsic coordinate system) with corresponding local node ordering are depicted in Figure 3.

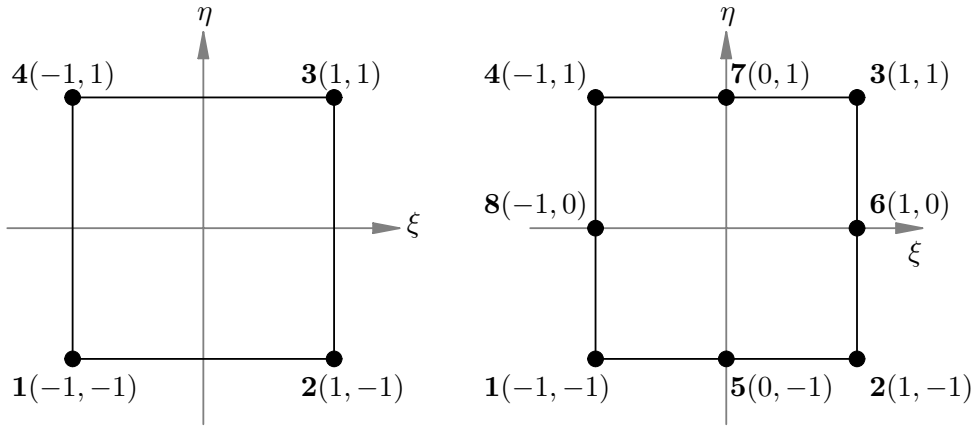

Fig. 3: quadrilateral element with linear ansatz order (left) and quadrilateral serendipity element with quadratic ansatz order (right)

Now, values $\mathbf{y}_P$ at any point P inside the element such as coordinates, displacements and tractions can be approximated using polynomial shape function values $N_n(\xi_P, \eta_P)$ where ξ_P and η_P are the intrinsic coordinates of point P.

$$\mathbf{y}_P = \sum_{n=1}^{N} N_n(\xi_P, \eta_P)\mathbf{y}_n^e \tag{30}$$

In Equation 30 $\mathbf{y}_n^e$ represents a vector containing nodal values at node n of element e.

3.2 Solving the system of equations

As all kernels are calculated, which will be explained in Section 3.3, the system of equations can be solved. Using the global coefficient matrices $[\Delta\mathbf{U}]$ and $[\Delta\mathbf{T}]$, which gather element contributions, the system of equations can be written as.

$$[\Delta\mathbf{T}]\{u\} = [\Delta\mathbf{U}]\{t\} \tag{31}$$

where $[\Delta\mathbf{T}]$ includes the free term and the vectors $\{u\}$ and $\{t\}$ contain displacements and tractions, respectively. Considering predefined boundary conditions of a mixed boundary value problem where displacements and tractions are prescribed on different portions of the boundary, the known values can be shifted to the right and all unknowns to the left of the equation system leading to following form:

$$[\mathbf{B}]\{x\} = \{b\} \tag{32}$$

The matrix $[B]$ contains the coefficients of the unknowns, the vector $\{x\}$ refers to the unknowns itself and vector $\{b\}$ contains the known values. The system of equation can be solved now, e.g. using Gauss elimination. Now the tractions and displacements at each node of the boundary are known. Detailed explanations and some small examples according the assembly process and solving the system of equations can be found in Reference [3].

Note, boundary stresses may be evaluated from the boundary displacements and tractions using Hook's law as outlined in Section 3.6.

3.3 Numerical Integration of the kernels $\Delta\mathbf{U}_{ni}^e$ and $\Delta\mathbf{T}_{ni}^e$

In what follows the numerical integration of the kernels $\Delta\mathbf{U}_{ni}^e$ and $\Delta\mathbf{T}_{ni}^e$ in Equation (29) will be explained. Recap, the 3-D BIE has a weak singularity of type $(\frac{1}{r})$ in the displacement kernel $\Delta\mathbf{U}_{ni}^e$ and a strong singularity of type $(\frac{1}{r^2})$ in traction kernel $\Delta\mathbf{T}_{ni}^e$. Thus, the different types of singularities have to be treated individually by applying proper numerical integration schemes as introduced in this section.

3.3.1 Evaluation of the free term and the strongly singular integral

Strongly singular integrals arise for the traction kernel $\Delta\mathbf{T}^e_{ni}$ if the source point P_i coincides with one of the element nodes. They simply can be evaluated by applying the concept of Rigid Body Motion to Equation (28). Following equation arises then:

$$\mathbf{cu}(P_i) + \sum_{e=1}^{E} \sum_{\substack{n=1 \\ g(n)=i}}^{N} \Delta\mathbf{T}^e_{ni}\mathbf{u}^e_n = -\sum_{e=1}^{E} \sum_{\substack{n=1 \\ g(n)\neq i}}^{N} \Delta\mathbf{T}^e_{ni}\mathbf{u}^e_n \tag{33}$$

Since no tractions arises when applying Rigid Body Motion only the sum containing the traction kernel $\Delta\mathbf{T}^e_{ni}$ and the term including the free term remain. The sum of the traction kernels is separated into the sum involving strongly singular integration ($g(n) = i$) and the sum excluding strongly singular integration ($g(n) \neq i$). g(n) stands for nodes with global node number g and local node number n.

As a consequence of applying Rigid Body Motion strongly singular integration is avoided, since it simply can be computed by taking the negative sum of all off-coefficients. Furthermore, the free term is also calculated at no additional expense.

For infinite domains an additional integral over an infinite extended boundary surface Γ_∞ has to be considered on the right hand side of Equation (33). It can be evaluated analytically in the same manner as introduced in Section 2.3.2. The integral and its analytical solution is:

$$\int_{\Gamma_\infty} \mathbf{T}(P, Q)dS = -\mathbf{I} \tag{34}$$

where $\mathbf{I}$ is a 3x3 identity matrix in 3-D elasticity.

A detailed explanation about Rigid Body Motion can be found in Reference [3].

3.3.2 Weakly singular integration

Weakly singular integrals arise for the displacement kernel $\Delta\mathbf{U}^e_{ni}$ if the source point P_i coincides with one of the element nodes. In this case the element is split into triangular subelements. The individual local coordinate systems for each subelement is chosen in a way that the Jacobian of the transformation tends to zero at the singular point P_i. This transformation is called Lachat-Watson-transformation [8]. Numerical integration over the triangular subelements using Gauss Quadrature as introduced in Section 3.3.3 can be used to determine the displacement kernel $\Delta\mathbf{U}^e_{ni}$ in Equation (29) if $g(n) = P_i$ (see References [3, 6, 8]).

$$\Delta\mathbf{U}^e_{ni} \approx \sum_{s=1}^{N_s} \sum_{m=1}^{M} \sum_{k=1}^{K} N_n(\bar{\xi}_m, \bar{\eta}_k)\mathbf{U}(P_i, Q(\bar{\xi}_m, \bar{\eta}_k))J(\bar{\xi}_m, \bar{\eta}_k)\bar{J}(\bar{\xi}_m, \bar{\eta}_k)W_m W_k \tag{35}$$

The maximal number of triangular subelements N_s depends on the type of the element (two for linear elements and three for quadratic elements). For quadratic elements the number of triangular subelements can either be two or three depending at which node n the source point P_i is situated on. If P_i is one of the corner nodes two subelements are required, if it is one of the mid-side-nodes three

subelements are necessary. $\bar{J}(\bar{\xi},\bar{\eta})$ is the Jacobian of the transformation from the local $\bar{\xi},\bar{\eta}$ coordinates of the triangular subregion to the intrinsic ξ,η coordinates of the element [3].

Lachat-Watson-Transformation may also be applied to the traction kernel $\Delta\mathbf{T}^e_{ni}$ if the source point P_i is one of the elements nodes but not node n. Similar to the equation above following equation will arise.

$$\Delta\mathbf{T}^e_{ni} \approx \sum_{s=1}^{N_s}\sum_{m=1}^{M}\sum_{k=1}^{K} N_n(\bar{\xi}_m,\bar{\eta}_k)\mathbf{T}(P_i,Q(\bar{\xi}_m,\bar{\eta}_k))J(\bar{\xi}_m,\bar{\eta}_k)\bar{J}(\bar{\xi}_m,\bar{\eta}_k)W_mW_k \tag{36}$$

More detailed informations about applying Lachat-Watson-Transformation can be found in Reference [3].

3.3.3 Regular integration

The regular integration scheme is applied if the source point P_i is not one of the element nodes of the element. The kernels for the regular case can be approximated by using Gauss Quadrature in ξ and η direction of the element.

$$\begin{aligned}\Delta\mathbf{U}^e_{ni} &\approx \sum_{m=1}^{M}\sum_{k=1}^{K} N_n(\xi_m,\eta_k)\mathbf{U}(P_i,Q(\xi_m,\eta_k))J(\xi_m,\eta_k)W_mW_k\\ \Delta\mathbf{T}^e_{ni} &\approx \sum_{m=1}^{M}\sum_{k=1}^{K} N_n(\xi_m,\eta_k)\mathbf{T}(P_i,Q(\xi_m,\eta_k))J(\xi_m,\eta_k)W_mW_k\end{aligned} \tag{37}$$

where M and K are the number of Gauss points in ξ and η direction, respectively. W_m and W_k are the corresponding weights. The number of Gauss points depends on the actual element dimensions in ξ and η direction (L_ξ, L_η), the minimal distance R between the collocation point P_i and the present element, the order of the kernel's singularities and the required accuracy for numerical integration. To keep it simple, the smaller the distance R and the greater either L_ξ or L_η the more Gauss points will be needed in both ξ and η direction. Detailed explanations about evaluating the number of Gauss points can be found in Reference [3].

In some cases the ratios R/L_ξ or R/L_η can be very inappropriate, resulting in an increasing number of Gauss points. It occurs for meshes consisting of elements with extremely varying dimensions or if boundary surfaces are located quite close to each other. In order to get along with a reduced set of Gauss points, the element is subdivided into subelements (subregions) and Gauss Quadrature is applied to each subelement [3]. Therefore, the equations in (37) are rewritten as follows:

$$\begin{aligned}\Delta\mathbf{U}^e_{ni} &\approx \sum_{l=1}^{N_\xi}\sum_{j=1}^{N_\eta}\sum_{m=1}^{M(l)}\sum_{k=1}^{K(j)} N_n(\bar{\xi}_m,\bar{\eta}_k)\mathbf{U}(P_i,Q(\bar{\xi}_m,\bar{\eta}_k))J(\xi_m,\eta_k)\bar{J}(N_\xi,N_\eta)W_mW_k\\ \Delta\mathbf{T}^e_{ni} &\approx \sum_{l=1}^{N_\xi}\sum_{j=1}^{N_\eta}\sum_{m=1}^{M(l)}\sum_{k=1}^{K(j)} N_n(\bar{\xi}_m,\bar{\eta}_k)\mathbf{T}(P_i,Q(\bar{\xi}_m,\bar{\eta}_k))J(\xi_m,\eta_k)\bar{J}(N_\xi,N_\eta)W_mW_k\end{aligned} \tag{38}$$

where N_ξ and N_η are the number of subelements in ξ and η direction which depends on the facts

stated above for the number of Gauss points. $M(l)$ and $K(j)$ are the number of Gauss points of the subregion defined by l and j. $\bar{\xi}$, $\bar{\eta}$ are the transformed local coordinates of each subregion and

$$\bar{J} = \frac{1}{N_\xi N_\eta} \tag{39}$$

Regular integration may also be applied to the remaining integration cases of the kernel $\Delta\mathbf{U}^e_{ni}$ which have not been discussed yet. It occurs if the source point P_i is one of the element nodes but not node n. In this case the shape function at P_i is zero and thus it eliminates the weak singularity of the kernel. As a consequence these integrals can be evaluated using the integration scheme introduced above as well.
For additional informations about the subdivision technique please refer to Reference [3].

In the following a small example will be shown which indicates different influences on the number of subelements. Therefore a flat three-dimensional rectangular element which is twice as long as heigh is defined as shown in Figure 4. It is located in the y,z-plane, thus the ξ,η-axes coincide with the y,z-axes. To compute the number of subelements the same parameters as in Reference [3] were used, meaning the number of Gauss points ($M(l)$, $K(j)$) were chosen to be four resulting in a total number of Gauss points of 16 for each subregion. Also the limiting values for the distance R were chosen to be the same as in Reference [3], that is, a maximal integration error of 10^{-3} occurs. Results for a point p approaching the element along the x-axis are depicted in Figures 5 and 6 which include the number of subdivisions for hyper singularities too as they arise in the SSI.

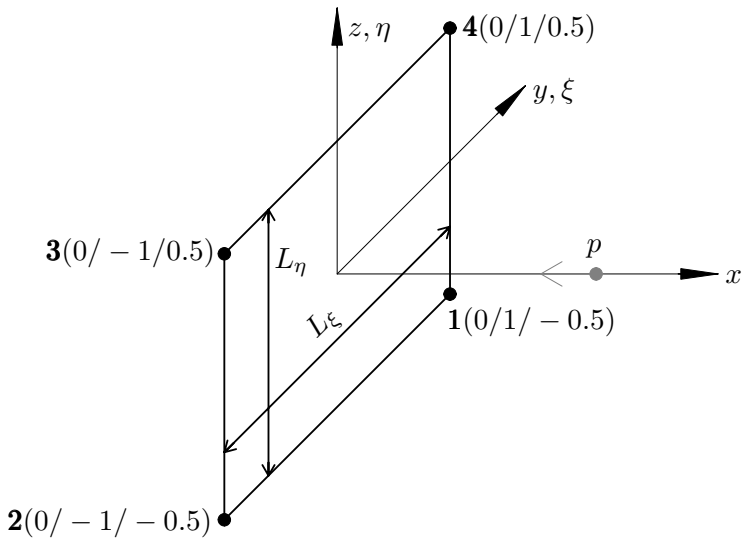

Fig. 4: sketch of rectangular element in y, z-plane

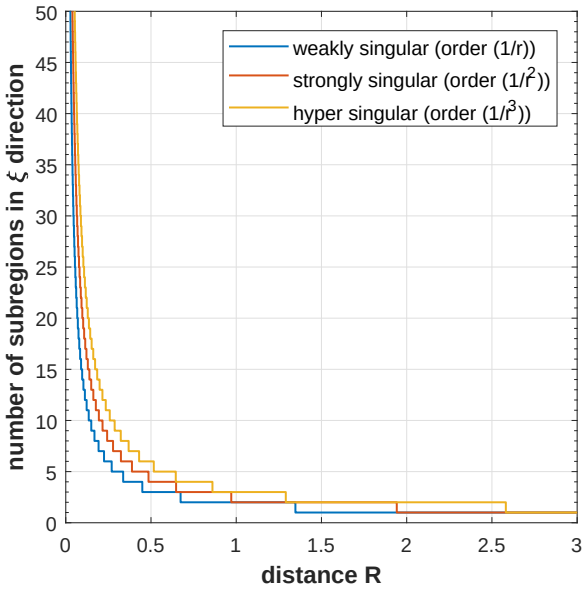

Fig. 5: number of subdivisions in ξ-direction

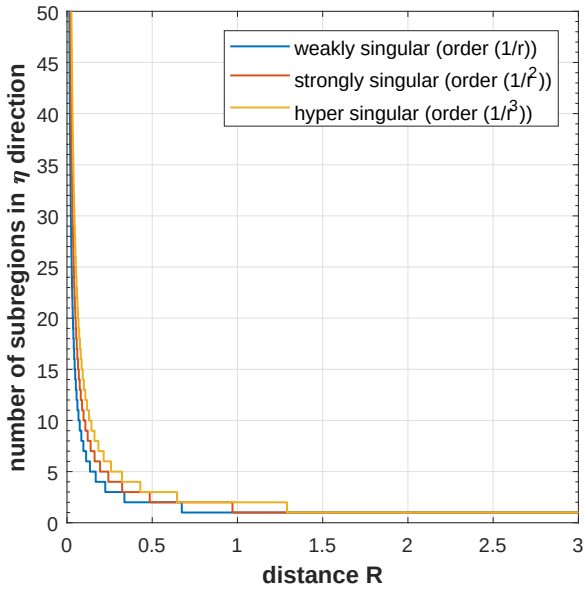

Fig. 6: number of subdivisions in η-direction

As can be seen in Figures 5 and 6 the number of subregions generally depends on the proximity of p to the element. This means the closer p the more subregions will be necessary to obtain results with same accuracy. The figures also show the influence of the singularity orders as for higher orders more subregions are required to achieve the same accuracy as for lower orders when keeping the distance R constant. Furthermore, the dimensions of the element influence the number of subelements too as can be recognized by comparing the results in Figure 5 with those in Figure 6. For identical distances R more subregions are required on the long side (L_ξ in this case) than on the other side which is shorter (L_η in this case). Finally, it is to say that the number of subelements tends to very large numbers beyond a certain proximity of point p resulting in an increasing computation time. Especially for computing interior results using the non-regularized forms of the Somigliana Identities this may be an issue as interior points sometimes are located very close to the boundary. Thus, the number of subelements may be limited for saving in computation time. This leads to inaccurate results for points p approaching the element beyond a corresponding distance R which depends on the chosen limiting number of subregions.

3.4 Discretization and numerical integration of the Somigliana Identities for interior results

In what follows the discretization and numerical evaluation of the Somigliana Identities for interior results at points p in a 3-D domain will be discussed. The boundary displacements $\mathbf{u}_n^e$ and boundary tractions $\mathbf{t}_n^e$ are assumed to be known from evaluating the BIE and from solving the system of equations (See Sections 3.1 and 3.2).

3.4.1 Discretized forms of the Somigliana Identities for interior results

The discretized form of the SDI in Equation (4), which is needed for the numerical evaluation of displacements $\mathbf{u}(p)$ at interior points p, can be written as:

$$\mathbf{u}(p) = \sum_{e=1}^{E} \sum_{n=1}^{N} \Delta\mathbf{U}_n^e \mathbf{t}_n^e - \sum_{e=1}^{E} \sum_{n=1}^{N} \Delta\mathbf{T}_n^e \mathbf{u}_n^e \tag{40}$$

where

$$\begin{aligned} \Delta\mathbf{U}_n^e &= \int_{\Gamma_e} N_n(\xi,\eta)\mathbf{U}(p, Q(\xi,\eta))d\Gamma(\xi,\eta) \\ \Delta\mathbf{T}_n^e &= \int_{\Gamma_e} N_n(\xi,\eta)\mathbf{T}(p, Q(\xi,\eta))d\Gamma(\xi,\eta) \end{aligned} \tag{41}$$

The discretized form of the SSI in Equation (5) allows the numerical stress evaluation at interior points p:

$$\boldsymbol{\sigma}(p) = \sum_{e=1}^{E} \sum_{n=1}^{N} \Delta\mathbf{S}_n^e \mathbf{t}_n^e - \sum_{e=1}^{E} \sum_{n=1}^{N} \Delta\mathbf{R}_n^e \mathbf{u}_n^e \tag{42}$$

where

$$\begin{aligned} \Delta\mathbf{S}_n^e &= \int_{\Gamma_e} N_n(\xi,\eta)\mathbf{S}(p, Q(\xi,\eta))d\Gamma(\xi,\eta) \\ \Delta\mathbf{R}_n^e &= \int_{\Gamma_e} N_n(\xi,\eta)\mathbf{R}(p, Q(\xi,\eta))d\Gamma(\xi,\eta) \end{aligned} \tag{43}$$

$\boldsymbol{\sigma}(p)$ in Equation 42 is a pseudo-stress vector.

3.4.2 Numerical integration of the Somigliana Identities

The integrals $\Delta\mathbf{U}_n^e$, $\Delta\mathbf{T}_n^e$ (Equation (41)) and $\Delta\mathbf{S}_n^e$, $\Delta\mathbf{R}_n^e$ (Equation (43)) can be computed numerically using Gauss Quadrature.

$$\begin{aligned} \Delta\mathbf{U}_n^e &\approx \sum_{m=1}^{M} \sum_{k=1}^{K} N_n(\xi_m,\eta_k)\mathbf{U}(p, Q(\xi_m,\eta_k))J(\xi_m,\eta_k)W_m W_k \\ \Delta\mathbf{T}_n^e &\approx \sum_{m=1}^{M} \sum_{k=1}^{K} N_n(\xi_m,\eta_k)\mathbf{T}(p, Q(\xi_m,\eta_k))J(\xi_m,\eta_k)W_m W_k \end{aligned} \tag{44}$$

and

$$\begin{aligned} \Delta\mathbf{S}_n^e &\approx \sum_{m=1}^{M} \sum_{k=1}^{K} N_n(\xi_m,\eta_k)\mathbf{S}(p, Q(\xi_m,\eta_k))J(\xi_m,\eta_k)W_m W_k \\ \Delta\mathbf{R}_n^e &\approx \sum_{m=1}^{M} \sum_{k=1}^{K} N_n(\xi_m,\eta_k)\mathbf{R}(p, Q(\xi_m,\eta_k))J(\xi_m,\eta_k)W_m W_k \end{aligned} \tag{45}$$

Furthermore, as the interior point p approaches the boundary Γ, subdivision will be necessary at a certain proximity and thus:

$$\begin{aligned}\Delta\mathbf{U}_n^e &\approx \sum_{l=1}^{N_\xi}\sum_{j=1}^{N_\eta}\sum_{m=1}^{M(l)}\sum_{k=1}^{K(j)} N_n(\bar{\xi}_m,\bar{\eta}_k)\mathbf{U}(p,Q(\bar{\xi}_m,\bar{\eta}_k))J(\xi_m,\eta_k)\bar{J}(N_\xi,N_\eta)W_mW_k \\ \Delta\mathbf{T}_n^e &\approx \sum_{l=1}^{N_\xi}\sum_{j=1}^{N_\eta}\sum_{m=1}^{M(l)}\sum_{k=1}^{K(j)} N_n(\bar{\xi}_m,\bar{\eta}_k)\mathbf{T}(p,Q(\bar{\xi}_m,\bar{\eta}_k))J(\xi_m,\eta_k)\bar{J}(N_\xi,N_\eta)W_mW_k\end{aligned} \tag{46}$$

and

$$\begin{aligned}\Delta\mathbf{S}_n^e &\approx \sum_{l=1}^{N_\xi}\sum_{j=1}^{N_\eta}\sum_{m=1}^{M(l)}\sum_{k=1}^{K(j)} N_n(\bar{\xi}_m,\bar{\eta}_k)\mathbf{S}(p,Q(\bar{\xi}_m,\bar{\eta}_k))J(\xi_m,\eta_k)\bar{J}(N_\xi,N_\eta)W_mW_k \\ \Delta\mathbf{R}_n^e &\approx \sum_{l=1}^{N_\xi}\sum_{j=1}^{N_\eta}\sum_{m=1}^{M(l)}\sum_{k=1}^{K(j)} N_n(\bar{\xi}_m,\bar{\eta}_k)\mathbf{R}(p,Q(\bar{\xi}_m,\bar{\eta}_k))J(\xi_m,\eta_k)\bar{J}(N_\xi,N_\eta)W_mW_k\end{aligned} \tag{47}$$

Both Gauss Quadrature and the subdivision scheme are applied in the same manner as outlined in Section 3.3.3.

3.5 Discretization and numerical integration of the regularized Somigliana Identities

The aim of this section is to describe the discretized forms as well as the numerical evaluation of the regularized Somigliana Identities for interior results. Since most of it is already explained, this section will concentrate on what is new in discretizing and numerically integrating the regularized forms of the SDI and SSI. Again the boundary displacements and tractions are considered to be already known from solving the BIE.

3.5.1 Discretized forms of the regularized Somigliana Identities for interior results

The discretized form of the regularized SDI from Equation (11) may be written as.

$$\mathbf{u}(p) = \mathbf{u}(P) + \sum_{e=1}^{E}\sum_{n=1}^{N}\Delta\mathbf{U}_n^e\mathbf{t}_n^e - \sum_{e=1}^{E}\sum_{n=1}^{N}\Delta\mathbf{T}_n^e\mathbf{u}_n^e + \mathbf{u}(P)\sum_{e=1}^{E}\Delta\mathbf{T}^e + \mathbf{u}(P)\int_{\Gamma_\infty}\mathbf{T}(p,Q)d\Gamma_\infty \tag{48}$$

where $\Delta\mathbf{U}_n^e$ and $\Delta\mathbf{T}_n^e$ are the same integrals as in Equation (44) and the integral over boundary Γ_∞ at infinity does not occur for finite domains. Thus, it has to be evaluated for infinite domains only and its solution is shown in Equation (12). Finally, the regularized integral term $\Delta\mathbf{T}^e$ can be written as follows.

$$\Delta\mathbf{T}^e = \int_\Gamma \mathbf{T}(p,Q(\xi,\eta))d\Gamma(\xi,\eta) \tag{49}$$

Discretizing the regular form of the SSI (Equation (19)) yields:

$$\begin{aligned}\boldsymbol{\sigma}(p) = \boldsymbol{\sigma}(P) + \sum_{e=1}^{E}\sum_{n=1}^{N}\Delta\mathbf{S}_n^e\mathbf{t}_n^e - \sum_{e=1}^{E}\Delta\mathbf{S}^e - \sum_{e=1}^{E}\sum_{n=1}^{N}\Delta\mathbf{R}_n^e\mathbf{u}_n^e + \sum_{e=1}^{E}\Delta\mathbf{R}^e - \\ \int_{\Gamma_\infty}\mathbf{S}(p,Q)\mathbf{t}^*(Q)d\Gamma_\infty + \int_{\Gamma_\infty}\mathbf{R}(p,Q)\mathbf{u}^*(Q)d\Gamma_\infty\end{aligned} \tag{50}$$

$\Delta\mathbf{S}_n^e$ and $\Delta\mathbf{R}_n^e$ can be evaluated as shown in Equation (43). Again the integrals over the boundary Γ_∞ at infinity have to be evaluated for infinite domains only by using the analytical solutions of Equations (22) and (23). The regularized integral terms $\Delta\mathbf{S}^e$ and $\Delta\mathbf{R}^e$ can be evaluated as follows:

$$\begin{aligned}\Delta\mathbf{S}^e &= \int_\Gamma \mathbf{S}(p, Q(\xi,\eta))\mathbf{t}^*(Q(\xi,\eta))d\Gamma \\ \Delta\mathbf{R}^e &= \int_\Gamma \mathbf{R}(p, Q(\xi,\eta))\mathbf{u}^*(Q(\xi,\eta))d\Gamma\end{aligned} \tag{51}$$

where $\mathbf{t}^*(Q(\xi,\eta))$ and $\mathbf{u}^*(Q(\xi,\eta))$ additionally are rewritten:

$$\begin{aligned}\mathbf{t}^*(Q(\xi,\eta)) &= \boldsymbol{\sigma}_c^*(P)\mathbf{n}(Q(\xi,\eta)) \\ \mathbf{u}^*(Q(\xi,\eta)) &= \mathbf{u}(P) + \frac{\partial\mathbf{u}(P)}{\partial\mathbf{x}}\Delta\mathbf{x}(P, Q(\xi,\eta))\end{aligned} \tag{52}$$

3.5.2 Numerical Integration of the regularized Somigliana Identities

This section is about the numerical evaluation of the integrals $\Delta\mathbf{U}_n^e$, $\Delta\mathbf{T}_n^e$ and $\Delta\mathbf{T}^e$ for the regularized SDI and $\Delta\mathbf{S}_n^e$, $\Delta\mathbf{S}^e$, $\Delta\mathbf{R}_n^e$ and $\Delta\mathbf{R}^e$ for the regularized SSI. These integrals again can be computed using Gauss Quadrature as already introduced in Section 3.3.3.

The numerical integration of $\Delta\mathbf{U}_n^e$, $\Delta\mathbf{T}_n^e$, $\Delta\mathbf{S}_n^e$ and $\Delta\mathbf{R}_n^e$ is analogous to Equations (44) and (45).

Applying Gauss Quadrature to the regularizing integral term $\Delta\mathbf{T}^e$ in the discretized regular formulation of the SDI results in:

$$\Delta\mathbf{T}^e = \sum_{m=1}^{M}\sum_{k=1}^{K}\mathbf{T}(p, Q(\xi_m,\eta_k))J(\xi_m,\eta_k)W_mW_k \tag{53}$$

The regularizing integral terms $\Delta\mathbf{S}^e$ and $\Delta\mathbf{R}^e$ of the discretized regular formulation of the SSI can be integrated numerically as shown below.

$$\begin{aligned}\Delta\mathbf{S}^e &= \sum_{m=1}^{M}\sum_{k=1}^{K}\mathbf{S}(p, Q(\xi_m,\eta_k))\mathbf{t}^*(Q(\xi_m,\eta_k))J(\xi_m,\eta_k)W_mW_k \\ \Delta\mathbf{R}^e &= \sum_{m=1}^{M}\sum_{k=1}^{K}\mathbf{R}(p, Q(\xi_m,\eta_k))\mathbf{u}^*(Q(\xi_m,\eta_k))J(\xi_m,\eta_k)W_mW_k\end{aligned} \tag{54}$$

where

$$\begin{aligned}&\mathbf{t}^*(Q(\xi_m,\eta_k)) = \boldsymbol{\sigma}_c^*(P)\mathbf{n}(Q(\xi_m,\eta_k)) \\ &\mathbf{u}^*(Q(\xi_m,\eta_k)) = \mathbf{u}(P) + \frac{\partial\mathbf{u}(P)}{\partial\mathbf{x}}\Delta\mathbf{x}(P, Q(\xi_m,\eta_k)) \quad = \mathbf{u}(P) + \frac{\partial\mathbf{u}(P)}{\partial\mathbf{x}}[\mathbf{x}(Q(\xi_m,\eta_k)) - \mathbf{x}(P)]\end{aligned} \tag{55}$$

Note, $\Delta\mathbf{x}(P, Q(\xi_m,\eta_k))$ is replaced by $[\mathbf{x}(Q(\xi_m,\eta_k)) - \mathbf{x}(P)]$, where $\mathbf{x}(Q(\xi_m,\eta_k))$ and $\mathbf{x}(P)$ denote the coordinates of the present Gauss point (field point Q) and the coordinates of the regularizing point P, respectively. Thus, it can be interpreted as the distance vector between the Gauss point and the regularization point P.

3.6 Displacements, stresses and displacement gradient at a point inside an element

This section will explain how to compute the displacement $\mathbf{u}(P)$, the stresses $\boldsymbol{\sigma}(P)$ and $\boldsymbol{\sigma}_c^*(P)$, the pseudo-strain vector $\boldsymbol{\epsilon}(P)$ and the displacement gradient $\frac{\partial \mathbf{u}(P)}{\partial \mathbf{x}}$ at any point P on the discretized boundary. The evaluation of $\mathbf{u}(P)$ is simple and it is essential to put more effort in computing stresses and displacement derivatives. For this purpose a local coordinate system $(\bar{x}, \bar{y}, \bar{z})$ at point P inside the element e will be introduced. Then, local stress values and displacement derivatives will be evaluated and gathered in a local pseudo-stress vector $\bar{\boldsymbol{\sigma}}(P)$ and a local displacement gradient $\frac{\partial \mathbf{u}(P)}{\partial \bar{\mathbf{x}}}$. Finally local stresses and displacement derivatives will be transformed into global stresses and displacement derivatives by applying proper transformation schemes. The method of evaluating global stresses may also be applied to compute the remaining nodal stress values element-wise after solving the system of equations as part of post-processing. Moreover, it is assumed that the boundary displacements $\mathbf{u}_n^e$ and boundary tractions $\mathbf{t}_n^e$ at each node n of the elements e, where the point P is located on, are already known. Another prerequisite is the information of the intrinsic coordinates ξ_P, η_P of point P. For a regularizing point they may be evaluated using Newton iteration and for evaluating nodal boundary stresses the intrinsic coordinates ξ_P, η_P are simply taken to be those of the corresponding element node as can be found in Figure 3.

For stresses and displacement derivatives the just outlined method can also be found in Reference [2] which uses index notation and the evaluation of nodal global stresses is also explained in Reference [3].

3.6.1 Evaluation of displacements inside an element

At no additional expense the displacement $\mathbf{u}(P)$ at a point P inside an element can be evaluated using the interpolation formula of Equation (30).

$$\mathbf{u}(P) = \sum_{n=1}^{N} N_n(\xi_P, \eta_P)\mathbf{u}_n^e \tag{56}$$

3.6.2 Local orthogonal coordinate system

In order to compute the stress values gathered in $\boldsymbol{\sigma}(P)$ and $\boldsymbol{\sigma}_c^*(P)$ and the displacement derivatives gathered in $\boldsymbol{\epsilon}(P)$ and $\frac{\partial \mathbf{u}(P)}{\partial \mathbf{x}}$ at a point P inside an element a local orthogonal coordinate system $(\bar{x}, \bar{y}, \bar{z})$ has to be introduced as can be seen in Figure 7 for an arbitrary quadrilateral serendipity element with quadratic ansatz order.

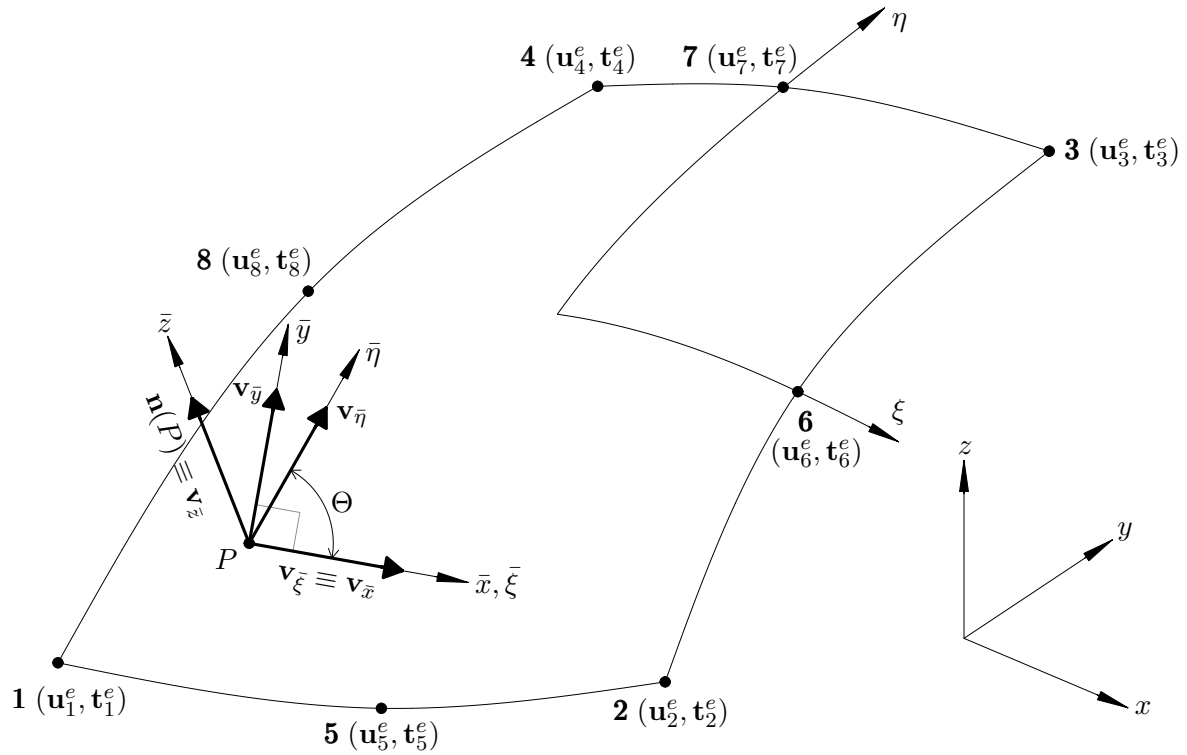

Fig. 7: local coordinate system $\bar{x}, \bar{y}, \bar{z}$ for a quadrilateral serendipity element with quadratic ansatz order

For defining the local orthogonal coordinate system ($\bar{x}$, $\bar{y}$, $\bar{z}$) the tangent plane in point P has to be determined. It is described by the tangent vectors $\mathbf{V}_{\bar{\xi}}$ and $\mathbf{V}_{\bar{\eta}}$ which can be evaluated by applying the interpolation formula from Equation (30) and replacing the shape functions by its derivatives with respect to either ξ or η.

$$\begin{aligned} \mathbf{V}_{\bar{\xi}} &= \sum_{n=1}^{N} \frac{\partial N_n}{\partial \xi}(\xi_P, \eta_P)\mathbf{x}_n^e \\ \mathbf{V}_{\bar{\eta}} &= \sum_{n=1}^{N} \frac{\partial N_n}{\partial \eta}(\xi_P, \eta_P)\mathbf{x}_n^e \end{aligned} \tag{57}$$

where $\mathbf{x}_n^e$ denotes a vector containing the global coordinates (x, y, z) of local node n.

The unit vectors $\mathbf{v}_{\bar{\xi}}$ and $\mathbf{v}_{\bar{\eta}}$ of the tangent plane are calculated using vector normalization. These vectors specify the direction of the local intrinsic coordinate system ($\bar{\xi}$, $\bar{\eta}$) and may not be orthogonal to each other (angle Θ) as shown in Figure 7,

$$\begin{aligned} \mathbf{v}_{\bar{\xi}} &= \frac{\mathbf{V}_{\bar{\xi}}}{|\mathbf{V}_{\bar{\xi}}|} \equiv \frac{\mathbf{V}_{\bar{\xi}}}{J_{\bar{\xi}}} \\ \mathbf{v}_{\bar{\eta}} &= \frac{\mathbf{V}_{\bar{\eta}}}{|\mathbf{V}_{\bar{\eta}}|} \equiv \frac{\mathbf{V}_{\bar{\eta}}}{J_{\bar{\eta}}} \end{aligned} \tag{58}$$

where

$$\begin{aligned} J_{\bar{\xi}} \equiv |\mathbf{V}_{\bar{\xi}}| &= \sqrt{V_{\bar{\xi},1}^2 + V_{\bar{\xi},2}^2 + V_{\bar{\xi},3}^2} \\ J_{\bar{\eta}} \equiv |\mathbf{V}_{\bar{\eta}}| &= \sqrt{V_{\bar{\eta},1}^2 + V_{\bar{\eta},2}^2 + V_{\bar{\eta},3}^2} \end{aligned} \tag{59}$$

$J_{\bar{\xi}}$ and $J_{\bar{\eta}}$ can be interpreted as scaling factors.

Now, the unit vector $\mathbf{v}_{\bar{z}}$ can be evaluated. It defines the direction of the local $\bar{z}$-axis and is also called the outward normal at point P ($\mathbf{n}(P)$).

$$\mathbf{v}_{\bar{z}} \equiv \mathbf{n}(P) = \frac{\mathbf{v}_{\bar{\xi}} \times \mathbf{v}_{\bar{\eta}}}{|\mathbf{v}_{\bar{\xi}} \times \mathbf{v}_{\bar{\eta}}|} \tag{60}$$

Next, the unit vectors $\mathbf{v}_{\bar{x}}$ and $\mathbf{v}_{\bar{y}}$ which specify the directions of the $\bar{x}$-$\bar{y}$ plane of the orthogonal local coordinate system $(\bar{x}, \bar{y}, \bar{z})$ may be determined as follows.

$$\begin{aligned} \mathbf{v}_{\bar{x}} &\equiv \mathbf{v}_{\bar{\xi}} \\ \mathbf{v}_{\bar{y}} &= \frac{\mathbf{v}_{\bar{z}} \times \mathbf{v}_{\bar{x}}}{|\mathbf{v}_{\bar{z}} \times \mathbf{v}_{\bar{x}}|} \end{aligned} \tag{61}$$

Additionally $cos(\Theta)$ and $sin(\Theta)$ can be evaluated.

$$\begin{aligned} cos(\Theta) &= \mathbf{v}_{\bar{\xi}} \bullet \mathbf{v}_{\bar{\eta}} \\ sin(\Theta) &= |\mathbf{v}_{\bar{\xi}} \times \mathbf{v}_{\bar{\eta}}| \end{aligned} \tag{62}$$

Now, the relationships between the local coordinates $\bar{x}, \bar{y}$ and the local intrinsic coordinates $\bar{\xi}$, $\bar{\eta}$ can be derived.

$$\begin{aligned} \bar{x} &= J_{\bar{\xi}} \cdot \bar{\xi} + J_{\bar{\eta}} \cdot \bar{\eta} \cdot cos(\Theta) \\ \bar{y} &= J_{\bar{\eta}} \cdot \bar{\eta} \cdot sin(\Theta) \end{aligned} \tag{63}$$

Solving these equations for $\bar{\xi}$ and $\bar{\eta}$ yields:

$$\begin{aligned} \bar{\xi} &= \frac{1}{J_{\bar{\xi}}}(\bar{x} - \frac{cos(\Theta)}{sin(\Theta)}\bar{y}) \\ \bar{\eta} &= \frac{\bar{y}}{J_{\bar{\eta}} \cdot sin(\Theta)} \end{aligned} \tag{64}$$

Finally taking the derivatives with respect to $\bar{x}$ and $\bar{y}$ will result in:

$$\begin{aligned} \frac{\partial \bar{\xi}}{\partial \bar{x}} &= \frac{1}{J_{\bar{\xi}}} \quad , \quad \frac{\partial \bar{\xi}}{\partial \bar{y}} = -\frac{cos(\Theta)}{J_{\bar{\xi}} \cdot sin(\Theta)} \\ \frac{\partial \bar{\eta}}{\partial \bar{x}} &= 0 \quad , \quad \frac{\partial \bar{\eta}}{\partial \bar{y}} = \frac{1}{J_{\bar{\eta}} \cdot sin(\Theta)} \end{aligned} \tag{65}$$

3.6.3 Computing local stresses and local displacement derivatives

For determining the local stress values the traction $\mathbf{t}(P)$ at point P has to be computed using the interpolation formula from Equation (30).

$$\mathbf{t}(P) = \sum_{n=1}^{N} N_n(\xi_P, \eta_P)\mathbf{t}_n^e \tag{66}$$

Furthermore, the displacement derivatives with respect to $\bar{\xi}$ and $\bar{\eta}$ have to be computed by applying the interpolation formula and replacing the shape functions by its derivatives with respect to either ξ or η.

$$\begin{aligned} \frac{\partial \mathbf{u}(P)}{\partial \bar{\xi}} &= \sum_{n=1}^{N} \frac{\partial N_n}{\partial \xi}(\xi_P, \eta_P)\mathbf{u}_n^e \\ \frac{\partial \mathbf{u}(P)}{\partial \bar{\eta}} &= \sum_{n=1}^{N} \frac{\partial N_n}{\partial \eta}(\xi_P, \eta_P)\mathbf{u}_n^e \end{aligned} \tag{67}$$

Figure 8 shows the stress components in the local orthogonal coordinate system ($\bar{x}$, $\bar{y}$, $\bar{z}$). These components have to be determined now.

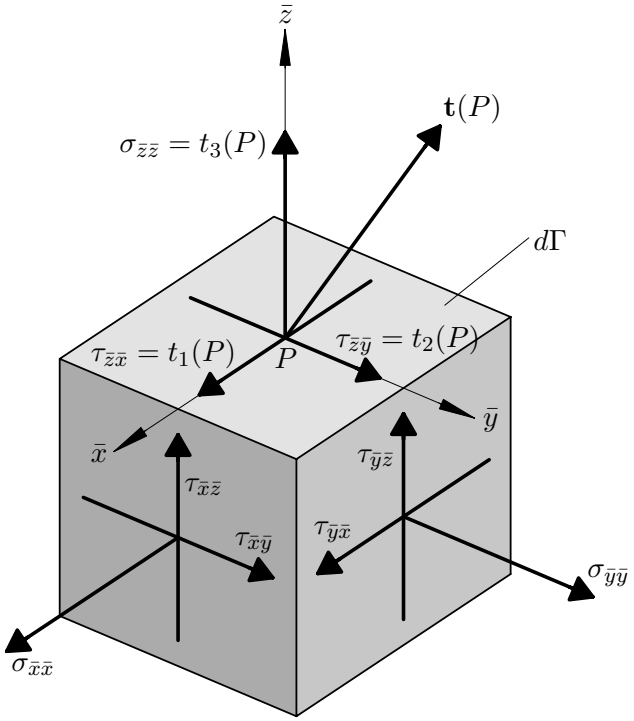

Fig. 8: Stress components at point P in the local orthogonal coordinate system ($\bar{x}$, $\bar{y}$, $\bar{z}$)

As can be seen from Figure 8 some local stress components are already calculated as they are components of the traction vector $\mathbf{t}(P)$. The remaining local stress values can be obtained by applying

Hook's law for isotropic materials in 3-D and equilibrium conditions.

$$\begin{aligned}
\sigma_{\bar{x}\bar{x}} &= \frac{E}{1-\nu^2}(\epsilon_{\bar{x}\bar{x}} + \nu \cdot \epsilon_{\bar{y}\bar{y}}) + \frac{\nu}{\nu-1} \cdot t_{\bar{z}} \\
\sigma_{\bar{y}\bar{y}} &= \frac{E}{1-\nu^2}(\epsilon_{\bar{y}\bar{y}} + \nu \cdot \epsilon_{\bar{x}\bar{x}}) + \frac{\nu}{\nu-1} \cdot t_{\bar{z}} \\
\sigma_{\bar{z}\bar{z}} &= t_3(P) \\
\tau_{\bar{x}\bar{y}} &\equiv \tau_{\bar{y}\bar{x}} = G \cdot \gamma_{\bar{x}\bar{y}} \\
\tau_{\bar{y}\bar{z}} &\equiv \tau_{\bar{z}\bar{y}} = t_2(P) \\
\tau_{\bar{x}\bar{z}} &\equiv \tau_{\bar{z}\bar{x}} = t_1(P)
\end{aligned} \tag{68}$$

From Equation 68 it can be seen that the stress components which still have to be calculated ($\sigma_{\bar{x}\bar{x}}$, $\sigma_{\bar{y}\bar{y}}$ and $\tau_{\bar{x}\bar{y}}$) are related to strains. These strains are composed of some local displacement derivatives in $\frac{\partial \mathbf{u}(P)}{\partial \bar{\mathbf{x}}}$. The local displacement derivatives can be interpreted as the projection of the derivatives of the displacement vector $\mathbf{u}(P)$ onto the unit vectors $\mathbf{v}_{\bar{x}}$, $\mathbf{v}_{\bar{y}}$ and $\mathbf{v}_{\bar{z}}$ and then taking the derivatives with respect to $\bar{x}, \bar{y}$ or $\bar{z}$. By using the results of Equations (60), (61), (65) and (67) they can be evaluated as follows. Note, not all of them are necessary to compute the remaining stress values. With regard to the local displacement gradient $\frac{\partial \mathbf{u}(P)}{\partial \bar{\mathbf{x}}}$ all required local displacement derivatives for both computing the remaining local stress values and the local displacement derivatives are listed below.

$$\begin{aligned}
\frac{\partial u_{\bar{x}}}{\partial \bar{x}} &= \left(\frac{\partial \mathbf{u}(P)}{\partial \bar{\xi}} \bullet \mathbf{v}_{\bar{x}}\right)\frac{\partial \bar{\xi}}{\partial \bar{x}} + \left(\frac{\partial \mathbf{u}(P)}{\partial \bar{\eta}} \bullet \mathbf{v}_{\bar{x}}\right)\frac{\partial \bar{\eta}}{\partial \bar{x}} \\
\frac{\partial u_{\bar{y}}}{\partial \bar{y}} &= \left(\frac{\partial \mathbf{u}(P)}{\partial \bar{\xi}} \bullet \mathbf{v}_{\bar{y}}\right)\frac{\partial \bar{\xi}}{\partial \bar{y}} + \left(\frac{\partial \mathbf{u}(P)}{\partial \bar{\eta}} \bullet \mathbf{v}_{\bar{y}}\right)\frac{\partial \bar{\eta}}{\partial \bar{y}} \\
\frac{\partial u_{\bar{x}}}{\partial \bar{y}} &= \left(\frac{\partial \mathbf{u}(P)}{\partial \bar{\xi}} \bullet \mathbf{v}_{\bar{x}}\right)\frac{\partial \bar{\xi}}{\partial \bar{y}} + \left(\frac{\partial \mathbf{u}(P)}{\partial \bar{\eta}} \bullet \mathbf{v}_{\bar{x}}\right)\frac{\partial \bar{\eta}}{\partial \bar{y}} \\
\frac{\partial u_{\bar{y}}}{\partial \bar{x}} &= \left(\frac{\partial \mathbf{u}(P)}{\partial \bar{\xi}} \bullet \mathbf{v}_{\bar{y}}\right)\frac{\partial \bar{\xi}}{\partial \bar{x}} + \left(\frac{\partial \mathbf{u}(P)}{\partial \bar{\eta}} \bullet \mathbf{v}_{\bar{y}}\right)\frac{\partial \bar{\eta}}{\partial \bar{x}} \\
\frac{\partial u_{\bar{z}}}{\partial \bar{x}} &= \left(\frac{\partial \mathbf{u}(P)}{\partial \bar{\xi}} \bullet \mathbf{v}_{\bar{z}}\right)\frac{\partial \bar{\xi}}{\partial \bar{x}} + \left(\frac{\partial \mathbf{u}(P)}{\partial \bar{\eta}} \bullet \mathbf{v}_{\bar{z}}\right)\frac{\partial \bar{\eta}}{\partial \bar{x}} \\
\frac{\partial u_{\bar{z}}}{\partial \bar{y}} &= \left(\frac{\partial \mathbf{u}(P)}{\partial \bar{\xi}} \bullet \mathbf{v}_{\bar{z}}\right)\frac{\partial \bar{\xi}}{\partial \bar{y}} + \left(\frac{\partial \mathbf{u}(P)}{\partial \bar{\eta}} \bullet \mathbf{v}_{\bar{z}}\right)\frac{\partial \bar{\eta}}{\partial \bar{y}}
\end{aligned} \tag{69}$$

For computing the remaining stress components the following relations between strains and local displacement derivatives are required. These relations are known from continuum mechanics.

$$\begin{aligned}
\epsilon_{\bar{x}\bar{x}} &= \frac{\partial u_{\bar{x}}}{\partial \bar{x}} \\
\epsilon_{\bar{y}\bar{y}} &= \frac{\partial u_{\bar{y}}}{\partial \bar{y}} \\
\gamma_{\bar{x}\bar{y}} &\equiv \gamma_{\bar{y}\bar{x}} = \frac{\partial u_{\bar{x}}}{\partial \bar{y}} + \frac{\partial u_{\bar{y}}}{\partial \bar{x}}
\end{aligned} \tag{70}$$

The remaining stress values $\sigma_{\bar{x}\bar{x}}$, $\sigma_{\bar{y}\bar{y}}$ and $\tau_{\bar{x}\bar{y}}$ can be evaluated by inserting the relations from Equation (70) in the corresponding formulas of Equation (68).

For the local displacement gradient $\frac{\partial \mathbf{u}(P)}{\partial \bar{\mathbf{x}}}$ it is required to compute three additional local displacement derivatives. Therefore following relations between strains and local displacement derivatives will be

necessary.

$$\begin{aligned}\epsilon_{\bar{z}\bar{z}} &= \frac{\partial u_{\bar{z}}}{\partial \bar{z}} \\ \gamma_{\bar{x}\bar{z}} &= \frac{\partial u_{\bar{x}}}{\partial \bar{z}} + \frac{\partial u_{\bar{z}}}{\partial \bar{x}} \\ \gamma_{\bar{y}\bar{z}} &= \frac{\partial u_{\bar{y}}}{\partial \bar{z}} + \frac{\partial u_{\bar{z}}}{\partial \bar{y}}\end{aligned} \tag{71}$$

Furthermore, applying Hook's law yields:

$$\begin{aligned}\epsilon_{\bar{z}\bar{z}} &= \frac{1}{E}[\sigma_{\bar{z}\bar{z}} - \nu(\sigma_{\bar{x}\bar{x}} + \sigma_{\bar{y}\bar{y}})] \\ \tau_{\bar{x}\bar{z}} &= G \cdot \gamma_{\bar{x}\bar{z}} \\ \tau_{\bar{y}\bar{z}} &= G \cdot \gamma_{\bar{y}\bar{z}}\end{aligned} \tag{72}$$

Then, inserting the formulas of Equation (71) into the corresponding ones of Equation (72), rearranging and using the stress values, which have already been computed, results in:

$$\begin{aligned}\frac{\partial u_{\bar{z}}}{\partial \bar{z}} &= \frac{1}{E}[\sigma_{\bar{z}\bar{z}} - \nu(\sigma_{\bar{x}\bar{x}} + \sigma_{\bar{y}\bar{y}})] \\ \frac{\partial u_{\bar{x}}}{\partial \bar{z}} &= \frac{\tau_{\bar{x}\bar{z}}}{G} - \frac{\partial u_{\bar{z}}}{\partial \bar{x}} \\ \frac{\partial u_{\bar{y}}}{\partial \bar{z}} &= \frac{\tau_{\bar{y}\bar{z}}}{G} - \frac{\partial u_{\bar{z}}}{\partial \bar{y}}\end{aligned} \tag{73}$$

Now, all local stress values and displacement derivatives have been evaluated and analogous to Section 2.3.5 they can be gathered in the corresponding local pseudo-stress vector $\bar{\boldsymbol{\sigma}}(P)$ and the local displacement gradient $\frac{\partial \mathbf{u}(P)}{\partial \bar{\mathbf{x}}}$ for transformation into the global system which will be introduced next.

3.6.4 Transformation from local to global stress vectors and displacement gradients

The transformation from local stresses $\bar{\boldsymbol{\sigma}}(P)$ to global stresses $\boldsymbol{\sigma}(P)$ can be written as follows.

$$\boldsymbol{\sigma}(P) = \mathbf{T}_\sigma \bar{\boldsymbol{\sigma}}(P) \tag{74}$$

where $\mathbf{T}_\sigma$ denotes the transformation matrix. Its entries are composed of the vector entries of $\mathbf{v}_{\bar{x}}$, $\mathbf{v}_{\bar{y}}$ and $\mathbf{v}_{\bar{z}}$ which describe the direction of the local orthogonal coordinate system ($\bar{x}$, $\bar{y}$, $\bar{z}$).

$$\mathbf{T}_\sigma = \begin{bmatrix} v_{\bar{x},1}^2 & v_{\bar{x},2}^2 & v_{\bar{x},3}^2 & 2v_{\bar{x},1}v_{\bar{x},2} & 2v_{\bar{x},2}v_{\bar{x},3} & 2v_{\bar{x},1}v_{\bar{x},3} \\ v_{\bar{y},1}^2 & v_{\bar{y},2}^2 & v_{\bar{y},3}^2 & 2v_{\bar{y},1}v_{\bar{y},2} & 2v_{\bar{y},2}v_{\bar{y},3} & 2v_{\bar{y},1}v_{\bar{y},3} \\ v_{\bar{z},1}^2 & v_{\bar{z},2}^2 & v_{\bar{z},3}^2 & 2v_{\bar{z},1}v_{\bar{z},2} & 2v_{\bar{z},2}v_{\bar{z},3} & 2v_{\bar{z},1}v_{\bar{z},3} \\ v_{\bar{x},1}v_{\bar{y},1} & v_{\bar{x},2}v_{\bar{y},2} & v_{\bar{x},3}v_{\bar{y},3} & v_{\bar{x},1}v_{\bar{y},2} + v_{\bar{x},2}v_{\bar{y},1} & v_{\bar{x},2}v_{\bar{y},3} + v_{\bar{x},3}v_{\bar{y},2} & v_{\bar{x},1}v_{\bar{y},3} + v_{\bar{x},3}v_{\bar{y},1} \\ v_{\bar{y},1}v_{\bar{z},1} & v_{\bar{y},2}v_{\bar{z},2} & v_{\bar{y},3}v_{\bar{z},3} & v_{\bar{y},1}v_{\bar{z},2} + v_{\bar{y},2}v_{\bar{z},1} & v_{\bar{y},2}v_{\bar{z},3} + v_{\bar{y},3}v_{\bar{z},2} & v_{\bar{y},1}v_{\bar{z},3} + v_{\bar{y},3}v_{\bar{z},1} \\ v_{\bar{x},1}v_{\bar{z},1} & v_{\bar{x},2}v_{\bar{z},2} & v_{\bar{x},3}v_{\bar{z},3} & v_{\bar{x},1}v_{\bar{z},2} + v_{\bar{x},2}v_{\bar{z},1} & v_{\bar{x},2}v_{\bar{z},3} + v_{\bar{x},3}v_{\bar{z},2} & v_{\bar{x},1}v_{\bar{z},3} + v_{\bar{x},3}v_{\bar{z},1} \end{bmatrix} \tag{75}$$

Global pseudo-stress vectors $\boldsymbol{\sigma}(P)$ may be rearranged into global Cauchy-stress tensors $\boldsymbol{\sigma}_c^*(P)$ in the same manner as explained in Section 2.3.5. A detailed explanation of stress transformation can be found in Reference [3].

Finally, the transformation from local displacement gradients $\frac{\partial \mathbf{u}(P)}{\partial \bar{\mathbf{x}}}$ into global displacement gradients $\frac{\partial \mathbf{u}(P)}{\partial \mathbf{x}}$ can be written as:

$$\frac{\partial \mathbf{u}(P)}{\partial \mathbf{x}} = \mathbf{L}^T \frac{\partial \mathbf{u}(P)}{\partial \bar{\mathbf{x}}} \mathbf{L} \tag{76}$$

where $\mathbf{L}$ refers to a rotational matrix comprised of the unit vectors $\mathbf{v}_{\bar{x}}$, $\mathbf{v}_{\bar{y}}$ and $\mathbf{v}_{\bar{z}}$ and $\mathbf{L}^T$ is the transposed matrix of $\mathbf{L}$. The rotational matrix $\mathbf{L}$ is:

$$\mathbf{L} = \begin{bmatrix} v_{\bar{x},1} & v_{\bar{x},2} & v_{\bar{x},3} \\ v_{\bar{y},1} & v_{\bar{y},2} & v_{\bar{y},3} \\ v_{\bar{z},1} & v_{\bar{z},2} & v_{\bar{z},3} \end{bmatrix} \tag{77}$$

Also global displacement gradients may be rearranged into global pseudo-strain vectors $\boldsymbol{\epsilon}(P)$ analogous as explained in Section 2.3.5. The transformation from local into global displacement gradients is also outlined in Reference [2].

4 Test examples

In order to test the implemented BEM-application four test examples were created to compare the numerical results (BEM-results) with either a reference solution or an analytical solution. By choosing the test examples attention was paid to use both quadrilateral elements with linear ansatz order and quadrilateral serendipity elements with quadratic ansatz order, flat and curved elements and finite and infinite domains to cover all possible error sources and to guarantee that the application is running smoothly. Thus, the following four test examples were chosen to be investigated closer:

- Compression test in 3D
- Cantiliver beam in 3D
- Thick walled pressurized cylinder in 3D
- Tunnel in 3D

In what follows the results of these test examples will be analysed and discussed.

4.1 Compression test in 3D

4.1.1 Introduction

The simplest test which can be carried out in 3D is a compression test. Figure 9 shows the cuboid which is used in this example. It is 0.5m in length (L_x), 0.8m in width (L_y) and 1.5m in height (L_z) and it is subjected to a pressure $p_z = 1kPa$. The cuboid's base is restraint in such a way that the cuboid can expand or contract freely due to a load applied on the top. The Young's modulus E is 5[kPa] and the Poisson's ratio ν is 0.25. For obtaining numerical BEM-results the surface is decomposed into quadrilateral elements with linear ansatz order. The initial mesh consists of one element per face. Then, mesh refinements are done by halving each element side of the previous mesh resulting in four times more elements per refinement. In this example three meshes are used: "mesh 1", "mesh 2" and "mesh 3" which consist of six, 24 and 96 elements, respectively. Finally, the orange dashed line m in Figure 9 which runs from the centre of left face to the centre of the right face is the line along which interior results are calculated.

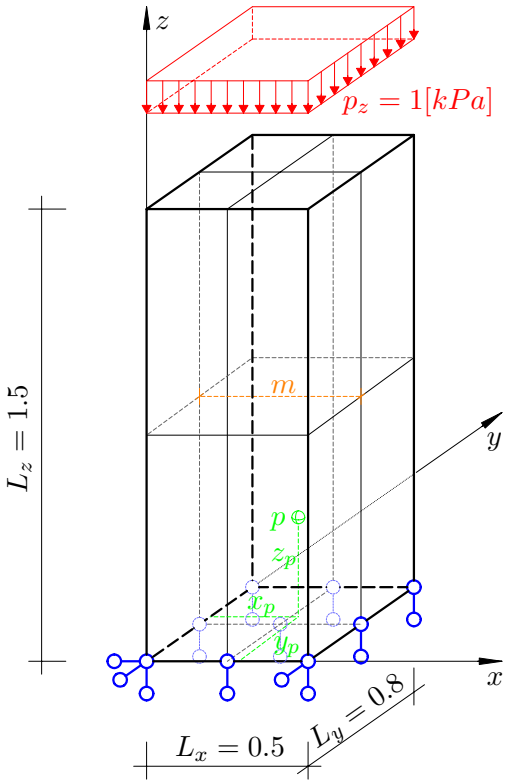

Fig. 9: Compression test in 3D (dimensions in [m])

4.1.2 Analytical Solution

In this example the analytical solution is known. It can be obtained from Hook's law. Since no shear stresses are acting on the cuboid only normal stresses have to be considered. The normal strains ϵ_{xx}, ϵ_{yy} and ϵ_{zz} for any point p of the cuboid can be calculated as follows (shear strains $\gamma_{xy} = \gamma_{xz} = \gamma_{yz} = 0$).

$$\begin{aligned} \epsilon_{xx} &= \frac{1}{E}[\sigma_{xx} - \nu(\sigma_{yy} + \sigma_{zz})] \\ \epsilon_{yy} &= \frac{1}{E}[\sigma_{yy} - \nu(\sigma_{xx} + \sigma_{zz})] \\ \epsilon_{zz} &= \frac{1}{E}[\sigma_{zz} - \nu(\sigma_{xx} + \sigma_{yy})] \end{aligned} \tag{78}$$

As there are no normal loads acting in x and y direction the corresponding normal stresses are zero ($p_x = \sigma_{xx} = 0$ and $p_y = \sigma_{yy} = 0$). Thus, Hook's law can be simplified and the deformations u_{x_p}, u_{y_p} and u_{z_p} in each direction for a point p within the cuboid can be calculated as follows:

$$\begin{aligned} \epsilon_{xx} &= -\frac{\nu}{E}\sigma_{zz} \quad , \quad u_{x_p} = \epsilon_{xx} \cdot x_p \\ \epsilon_{yy} &= -\frac{\nu}{E}\sigma_{zz} \quad , \quad u_{y_p} = \epsilon_{yy} \cdot y_p \\ \epsilon_{zz} &= \frac{1}{E}\sigma_{zz} \quad , \quad u_{z_p} = \epsilon_{zz} \cdot z_p \end{aligned} \tag{79}$$

where x_p, y_p and z_p are the cartesian coordinates of a point p as shown in green in Figure 9 for an arbitrary point.

The stresses at every point in the cuboid are constant. Only compressive stresses $\sigma_{zz} = p_z = 1kPa$ arise.

The maximal displacements $u_{x,max}$, $u_{y,max}$ and $u_{z,max}$ in each direction of the cuboid can be obtained by inserting the corresponding dimensions L_x, L_y and L_z for x_p, y_p and z_p in the formulas of Equation (79). From that the total lengths $L_{x,tot}$, $L_{y,tot}$ and $L_{z,tot}$ can be derived. Moreover, considering that the load p_z acting against the positive z-direction (pressure load), which means that the stress $\sigma_{zz} = p_z$ has a negative algebraic sign, yields:

Direction i	Original length L_i [m]	Strain ϵ_{ii} [%]	deformation $u_{i,max}$ [m]	Total length $L_{i,tot} = L_i + u_{i,max}$ [m]
x	0.5	5	0.025	0.525
y	0.8	5	0.040	0.840
z	1.5	-20	-0.300	1.200

Tab. 1: analytical solution for strains and displacements of the compression test

Figure 10 shows the original shape of the cuboid and the deformed shape after the load p_z is applied on the cuboid's top face. The original shape is coloured grey and the deformed shape is coloured black.

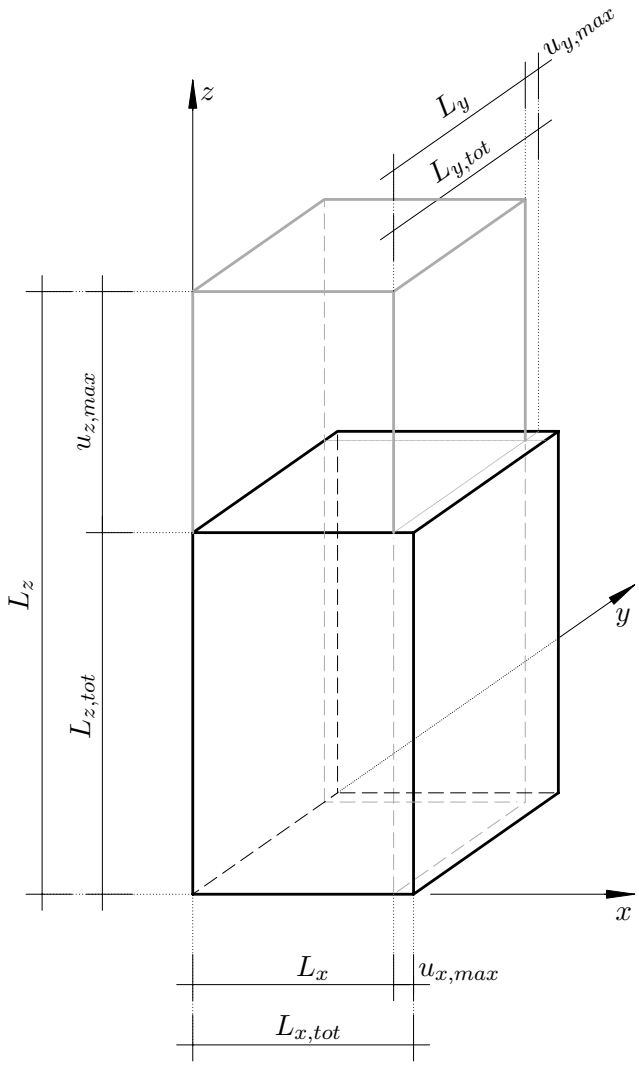

Fig. 10: original shape (grey) and deformed shape (black) of the cuboid

4.1.3 Boundary results

Figures 11 to 14 display boundary results obtained with the BEM-application using the coarsest mesh ("mesh 1"). The figures show deformations in each direction (u_x, u_y, u_z) and the normal stress in z-direction σ_{zz}.

As can be seen from the figures the deformations increasing or decreasing linearly as expected from the analytical solution in Equation (79). Also the maximal and minimal values coincide with those of the analytical solution in Table 1. Moreover the stress σ_{zz} is constant throughout the boundary and the value again coincides with that of the analytical solution. Thus, in this example the exact solution at the boundary can already be obtained with the BEM by using the coarsest mesh. This is because it is a linear problem.

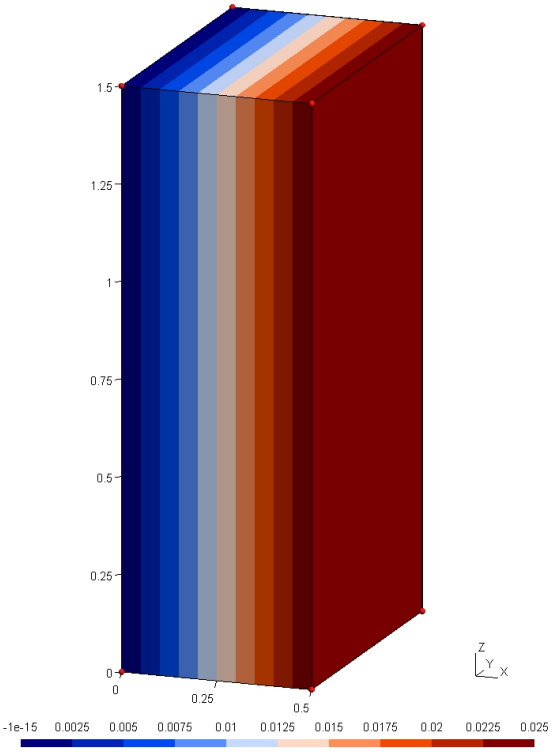

Fig. 11: deformation u_x [m]

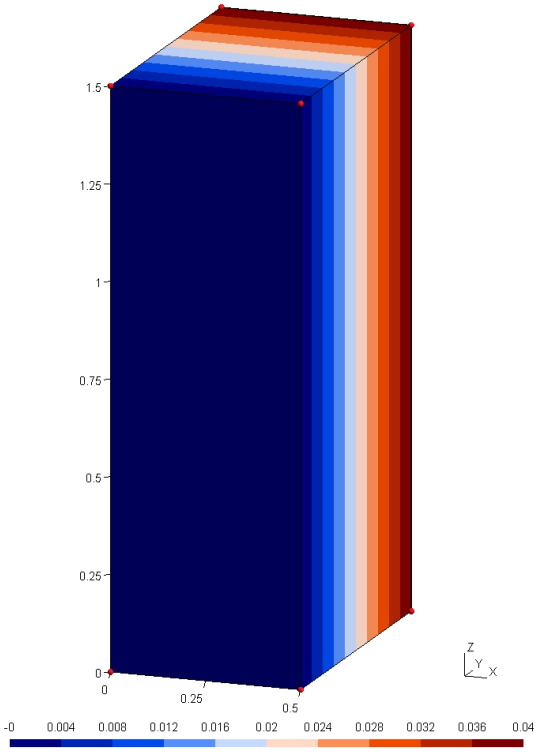

Fig. 12: deformation u_y [m]

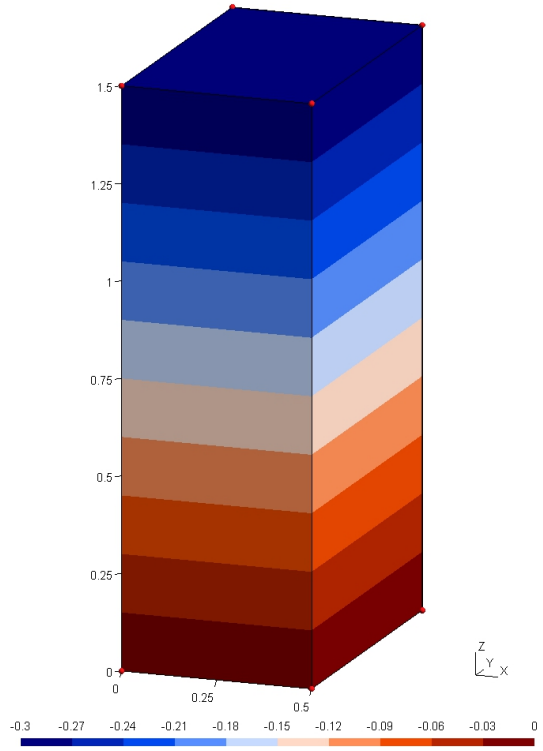

Fig. 13: deformation u_z [m]

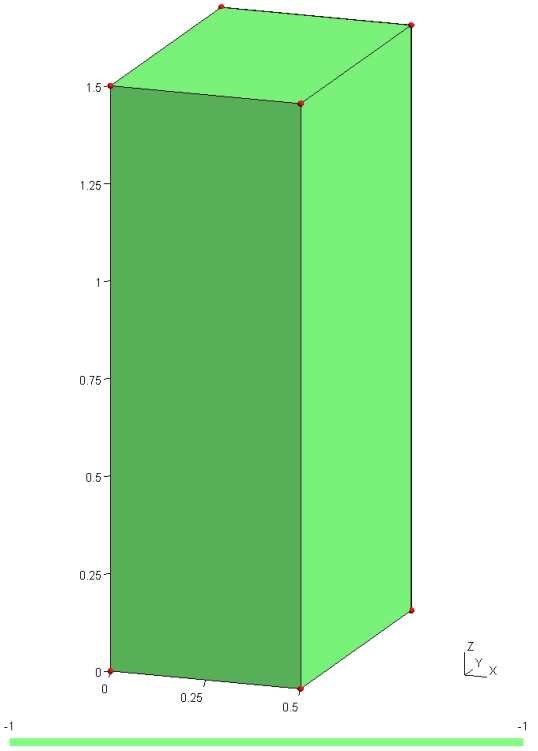

Fig. 14: normal stress σ_{zz} [kPa]

4.1.4 Influence of limited subregions on non-regularized interior results

The accuracy of non-regularized interior results near the boundary is highly dependent on the number of subregions in ξ- and η- direction. On the basis of what is discussed in Sections 3.3.3 and 3.4 this now is applied to a concrete example and discussed in what follows. Therefore, displacements u_z and stresses σ_{zz} along line m (orange dashed line in Figure 9) were numerically computed for all meshes and with certain limiting numbers of subelements. The results are depicted in Figures 15 to 17 which also include the analytical solutions for comparison. Since the effect is prominent near the boundary, only results of the first $0.05m$ of line m starting from the left boundary are shown in the figures.

Approaching the boundary and comparing the numerical results with the analytical solution, it can be figured out from the graphs that at a certain proximity to the boundary inaccuracies of numerical results become unacceptable. The distance between the point where inaccuracies of numerical results become unacceptable and the boundary is decreasing the higher the limiting numbers of subregions in ξ and η direction are. This is because of the reduction of the integration error due to a denser distribution of Gauss points which can capture the influence of the singularities of the fundamental solutions better. The accuracy of interior results is not only dependent on the number of subregions but also on the order of the singularities of the fundamental solutions. In contrary to stress results a point p can be brought closer towards the boundary without displacement results becoming inaccurate since the singularity order of the fundamental solutions in the SDI ($\mathbf{U}(p,Q)$, $\mathbf{T}(p,Q)$) is one degree lower as the singularity order of their counterparts in the SSI ($\mathbf{S}(p,Q)$, $\mathbf{R}(p,Q)$). This, for example, can be seen in Figure 16 when comparing the distributions of u_z and σ_{zz} obtained with ten subregions in maximum (red lines in the graphs). Displacements u_z already coincides with the analytical solution from a distance of about $0.02m$ from the boundary whereas stresses σ_{zz} only coincides with the analytical solution from a distance of about $0.03m$ from the boundary. Thus, more subelements would be required to obtain the same accuracy for stresses. Furthermore, assuming the same limiting number of subelements and results are accepted for the same error margin, the finer a mesh the closer a point p can be moved towards the boundary. This can be explained by the fact that the maximal number of subelements is valid for each element which generally results in more subregions available the more elements are used for the discretization of domains. Additionally, boundary results would become more accurate when taking finer meshes which consequently leads to better interior results too. Moreover, discretization errors would be minimized. However, these facts are obsolete in this example as already numerical results obtained with the coarsest mesh ("mesh 1") agree with the analytical solution and no discretization errors arise for the cuboid.

Summing up it can be said that interior results near the boundary obtained from the standard, non-regularized Somigliana Identities hardly will become accurate within a certain proximity to the boundary whether by increasing the number of subelements nor by taking finer meshes or applying both. Additionally, such measures would lead to vast increases in computation times. Thus, regularization of the Somigliana Displacement and Stress Identities is inevitable to achieve accurate interior results near boundary within an tolerable computation time.

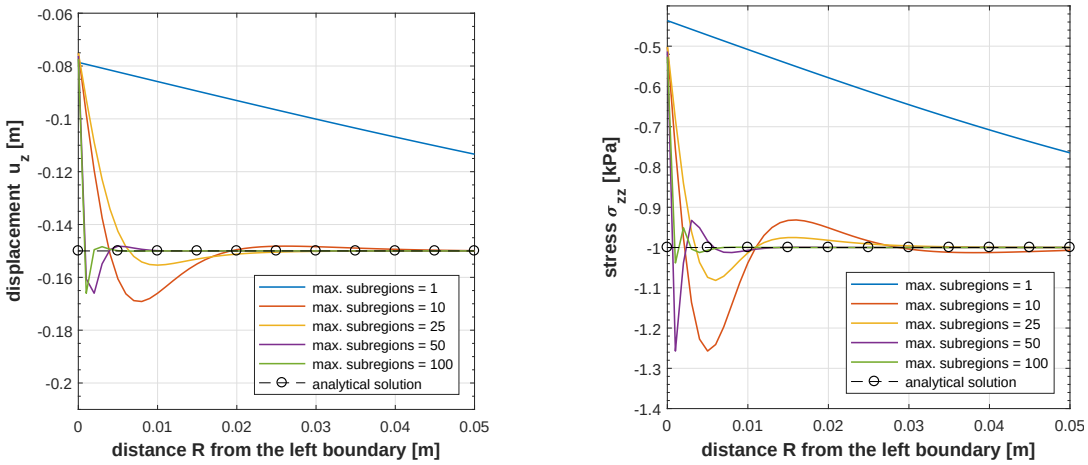

Fig. 15: mesh 1 (six elements): deformation u_z and stress σ_{zz}

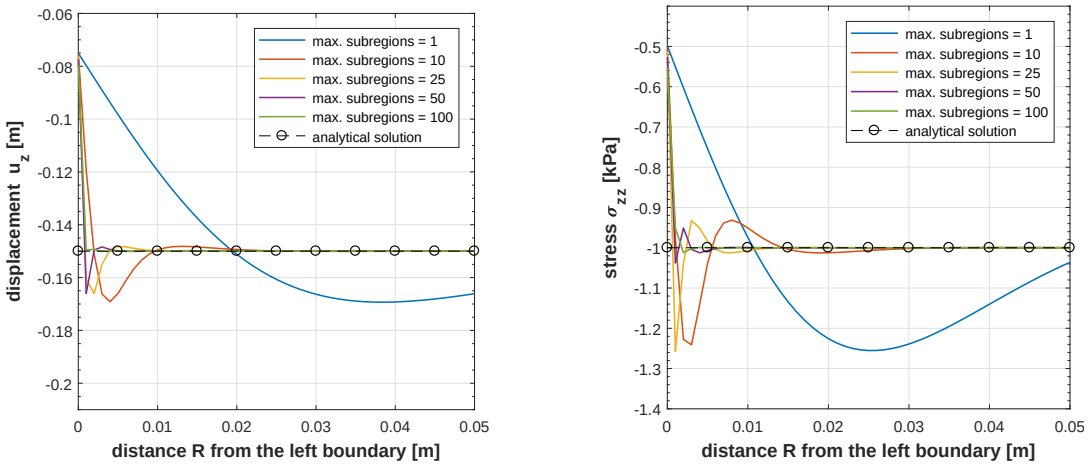

Fig. 16: mesh 2 (24 elements): deformation u_z and stress σ_{zz}

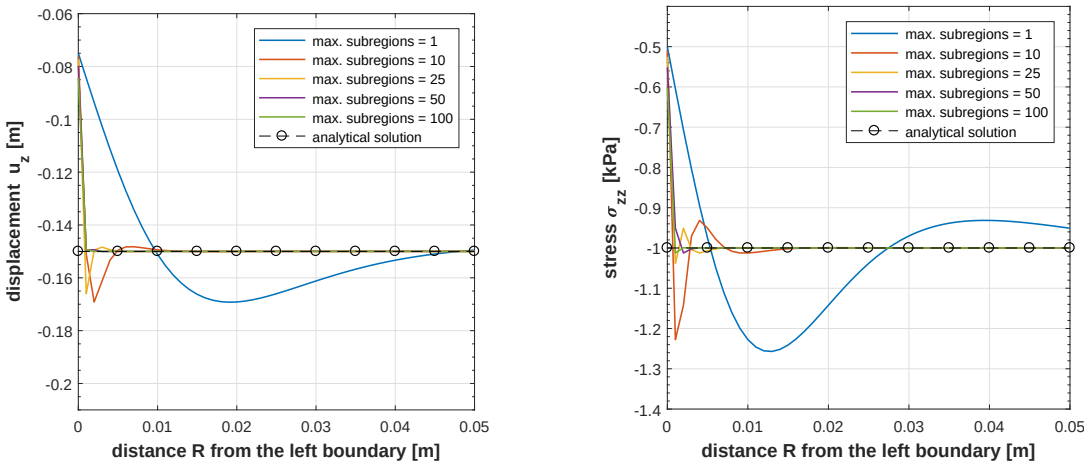

Fig. 17: mesh 3 (96 elements): deformation u_z and stress σ_{zz}

4.1.5 Regularized interior results

Now the regularized interior results will be discussed briefly. The following figure (Figure 18) sketches two graphs showing numerical results for the displacement u_z and the stress σ_{zz} again along the line m, which connects the centres of the left and right face of the cuboid as highlighted in orange in Figure 9. Both the non-regularized (standard) and the regularized formulations of the Somigliana Displacement and Stress Identities were used to compute numerical results. To see in detail what happen to numerically determined displacements u_z and stresses σ_{zz} only results for the first $0.02m$ of line m starting from the left face of the cuboid are depicted. For comparison, the graphs also include the analytical solutions. Numerical results were obtained for the coarsest mesh which consists of six elements ("mesh 1"). Moreover, the limit of subelements in both ξ- and η- direction for the non-regularized BEM-results was set to 50.

What stands out immediately in the graphs is that both displacements u_z and stresses σ_{zz} which were obtained from the regularized formulations of the Somigliana Identities coincide with the analytical solutions although the coarsest mesh ("mesh 1") was used to compute those results. This confirms the general character of the regularized Somigliana Identities as they mitigate the adverse effects of the singularities on results close to the boundary. Another reason for the excellent coincidence of regularized results with the analytical solutions is also the accuracy of the boundary results which agree exactly with the analytical solutions. Thus, the regularizing displacement $\mathbf{u}(P)$ and stress $\boldsymbol{\sigma}(P)$, which significantly can influence accuracy of regularized results very close to the boundary, can be evaluated exactly too in this example. Furthermore, these graphs again emphasize the problem of the non-regularized results near the boundary as the deviation from the analytical solution is unacceptable within a certain distance from the boundary.

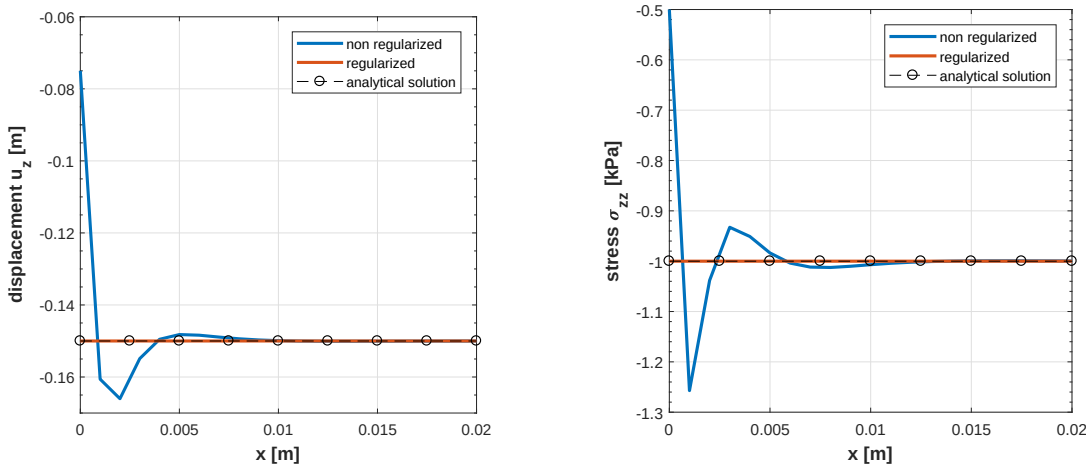

Fig. 18: interior results of mesh 1 (6 elements): deformation u_z and stress σ_{zz}

4.2 Cantilever beam in 3D

4.2.1 Introduction

The second example deals with a cantilever beam in 3D as depicted in Figure 19. It has a fully restraint support and it is subjected to a constantly distributed traction load $t_z = 10kPa$ acting in z-direction at the free end. The beam is $5m$ in length and $1m$ in height and width. The material properties are chosen to be $E = 100000kPa$ as the Young's modulus, $\nu = 0.0$ as the Poisson's ratio and $G = 50000kPa$ as the shear modulus, which can be derived by using the relationship between E, ν and G for homogeneous isotropic materials. In order to compute numerical BEM-results the geometry is decomposed into equally sized quadrilateral serendipity elements with quadratic ansatz order. Starting with an element side length of $0.5m$ the cantilever beam is decomposed into ten elements on the length and two elements on the width and height resulting in a mesh with 88 elements ("mesh 1"). Then two mesh refinements were carried out by gradually halving each element side as also applied in the compression test example. This causes the number of elements on the length, width and height to double for each refinement, and thus, "mesh 2" consists of 352 elements and "mesh 3" of 1408. The Euler-Bernoulli beam theory is considered to be the reference solution in this example. It is founded on two basic assumptions, namely plane cross-sections remain plane and perpendicular to the neutral axis after bending. Since this may be best satisfied in the middle of the cantilever beam the line along which interior stress results are computed is defined at $x = x_m = 2.5m$ (orange dashed line in Figure 19). Moreover, interior displacement results were computed along the neutral axis of the cantilever beam which coincides with the x-axis.

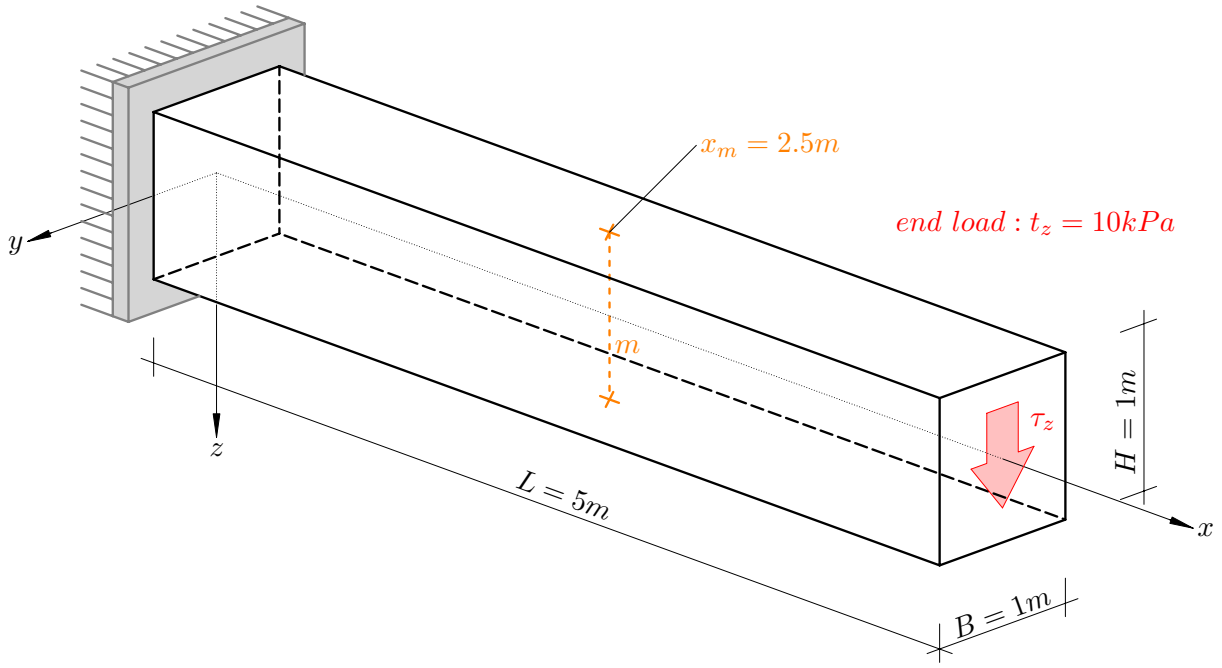

Fig. 19: Cantilever beam in 3D

4.2.2 Reference solution

In this example it is obvious to compare numerical results with the solutions of the Euler-Bernoulli beam theory. Due to simplifications of solid mechanics, such as the assumptions mentioned previously, it only can be considered as reference solution. Figure 20 shows the model of the cantilever beam used for the reference solution. Note, the traction load $t_z = 10kPa$ is transformed into an equivalent force $F_z = 10kN$.

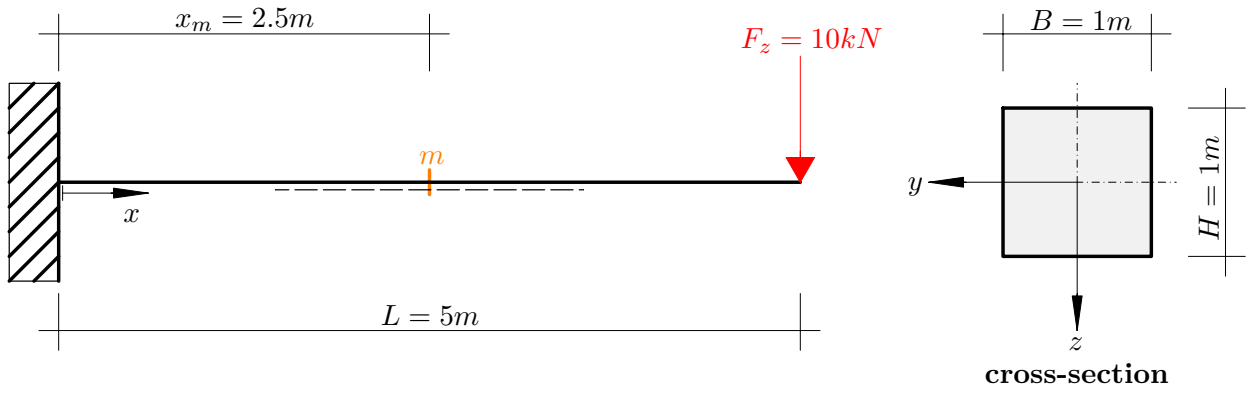

Fig. 20: model of the cantilever beam

The deflection curve $w(x)$ of a cantilever beam with constant cross-sections which is subjected to a force F_z at the free end may be computed as follows. Note, the shear deflection (second term in the equation) is considered as well.

$$w(x) = \frac{F_z x^2}{6EI_y}(3L - x) + \frac{F_z x}{\kappa GA} = \tag{80}$$

where I_y denotes the area moment of inertia about the y-axis, A the area of the cross-section and κ is the shear deflection constant also known as Timoshenko shear coefficient, which is dependent on the cross-section's geometry. $\kappa = 5/6$ for rectangular and $\kappa = 10/11$ for circular cross-sections.

Assuming a rectangular cross-section in Equation (80) yields:

$$w(x) = \frac{2F_z x^2}{EBH^3}(3L - x) + \frac{6F_z x}{5GBH} \tag{81}$$

In order to compute normal stresses $\sigma_{xx}(z)$ and shear stresses $\tau_{xz}(z)$ at any cross-section, the distribution of the bending moment $M_y(x)$ and the shear force $Q_z(x)$ has to be evaluated first. For the given cantilever beam they may written as follows.

$$\begin{aligned} M_y(x) &= F_z(x - L) \\ Q_z(x) &= F_z = const. \end{aligned} \tag{82}$$

Now the normal stress $\sigma_{xx}(z)$ and shear stresses $\tau_{xz}(z)$ can be calculated.

$$\begin{aligned} \sigma_{xx}(z) &= \frac{M_y(x)}{I_y} z \\ \tau_{xz}(z) &= -\frac{Q_z(x) S_y(z)}{I_y B} \end{aligned} \tag{83}$$

where $S_y(z)$ denotes the statical moment of area about the y-axis.

Equation (83) can be evaluated for a rectangular cross-section. This yields:

$$\begin{aligned} \sigma_{xx}(z) &= \frac{12M_y(x)}{BH^3}z \\ \tau_{xz}(z) &= -\frac{3Q_z(x)}{2BH}\left(1-4\frac{z^2}{H^2}\right) \end{aligned} \tag{84}$$

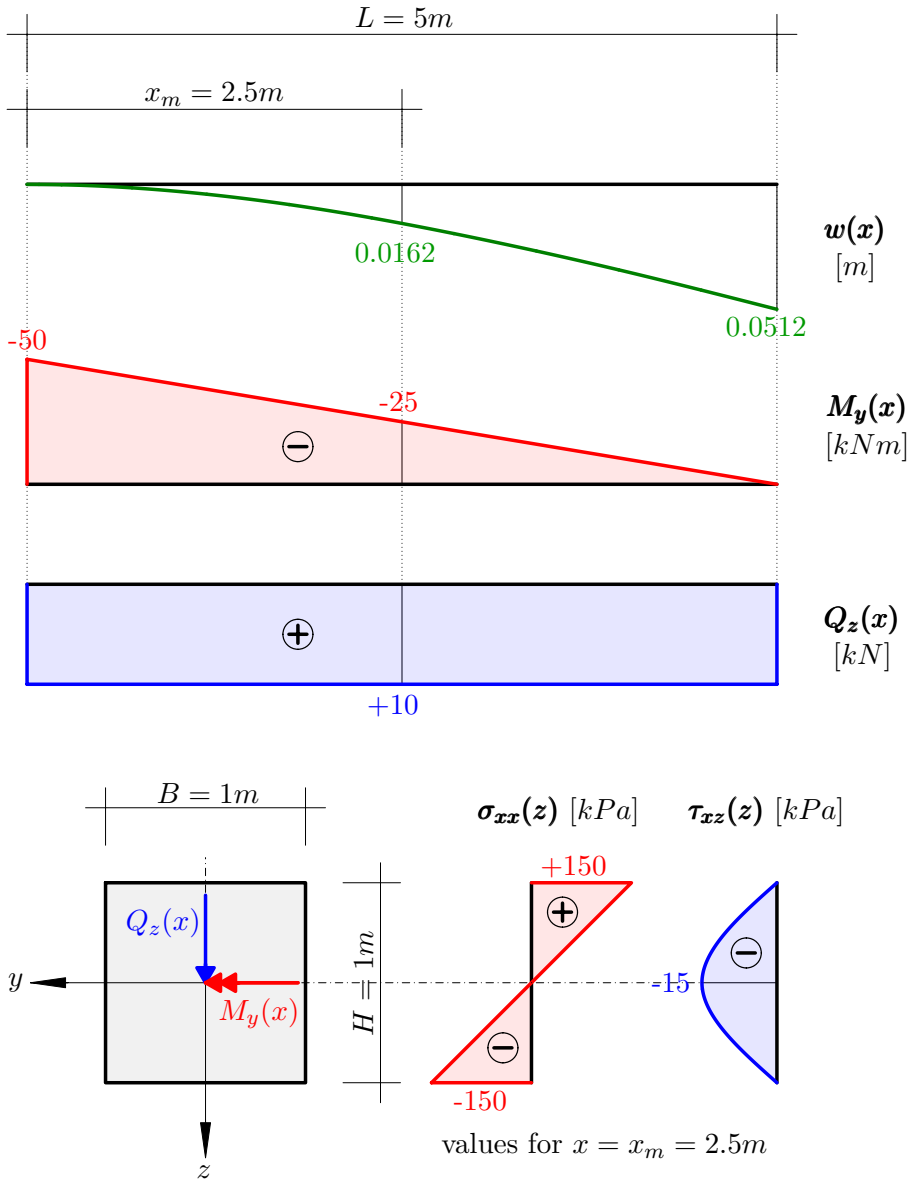

Fig. 21: reference solution of the cantilever beam

Figure 21 depicts the deflection curve $w(x)$ and the distribution of the bending moment $M_y(x)$ and shear force $Q_z(x)$ for the given cantilever beam. Moreover, the distribution of normal stresses $\sigma_{xx}(z)$ and shear stresses $\tau_{xz}(z)$ over a cross-section are shown where the values are evaluated for the cross-section at $x = x_m = 2.5m$.

4.2.3 Boundary results

Boundary results for the finest mesh ("mesh 3") are depicted in following figures. Figure 22 shows the total displacement u_{tot} and the corresponding deformed shape and Figure 23 the deformation w in z-direction. Figures 24 and 25 depict normal stresses σ_{xx} and shear stresses τ_{xz}, respectively. The total displacement $u_{p,tot}$ at any point p is defined as follows.

$$u_{p,tot} = \sqrt{u_p^2 + v_p^2 + w_p^2} \tag{85}$$

where u_p, v_p and w_p are deformations of point p in x-, y- and z- direction, respectively. Moreover, $v_p = 0$ throughout the domain and the deformed shape in Figure 22 is depicted with an enlargement factor of 10.

By comparing the total displacement u_{tot} and the deformation w in z-direction it can be seen that the maximal total deformation u_{tot} at the free end is slightly higher than the maximal deformation w in z-direction at the same location. That is, the total deformation also considers the deformation u in x-direction due to the curvature of the cross-section (see Equation (85)). Thus, the total deformation u_{tot} would be slightly higher than the corresponding deformation w in z-direction not only at the free end but also at each cross-section. Furthermore, there is hardly any difference between the maximal deformation w obtained with the BEM and that of the reference solution which is $0.0513m$ and $0.0512m$, respectively. In contrary to that, the difference between minimal and maximal normal stresses σ_{xx} computed with the BEM and that of the reference solution is quite big. The minimal and maximal normal stress σ_{xx} according to the reference solution, which can be obtained for the cross-section at $x = 0m$ (fixed end), is $\pm 300kPa$. The minimal and maximal normal stress σ_{xx} computed numerically at the same location is $\pm 323kPa$ as can be seen from Figure 24. Reasons for this differences may be that the Euler-Bernoulli beam theory is not valid at the fixed and free ends and the singular stress behaviour at fixed ends in general. Differences can also be detected for shear stresses τ_{xz}. According to the reference solution shear stresses should not exceed $0kPa$ at the top and the bottom of any cross-section and they should be quadratic distributed over the cross-sections with a minimum of $-15kPa$ in the middle ($z = 0m$; compare Figure 21). Without showing in detail, the minimal and maximal shear stresses τ_{xz} obtained with the BEM ($-16.3kPa$ and $2.61kPa$) only arise near the loaded free end and may be a result of the discontinuous load transmission in this example. The differences might be minimized if the traction load t_z is applied according to the expected shear stress distribution $\tau_{xz}(z)$ of the reference solution. Moreover, numerically computed shear stresses near the fixed end are not distributed according to the reference solution too as can be seen from Figure 25. Thus, numerically computed shear stresses vary widely from the reference solution in the affected regions (fixed and free ends) of the cantilever.

As a resume it can be said that the above described differences in normal and shear stresses near the fixed and free ends underpin that the line along which interior stress results are obtained is chosen to be in the middle of the cantilever to achieve results which are comparable with the reference solution.

This is roughly outlined in the introduction of this example too (see Section 4.2.1).

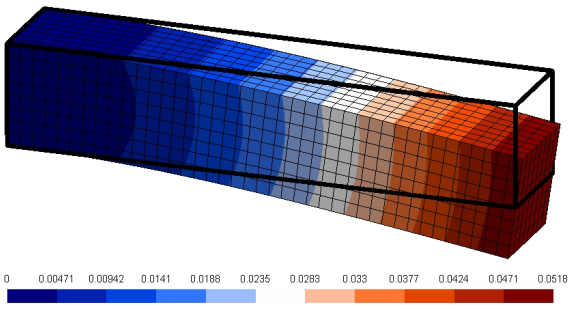

Fig. 22: deformed shape & tot. displ. u_{tot} [m]

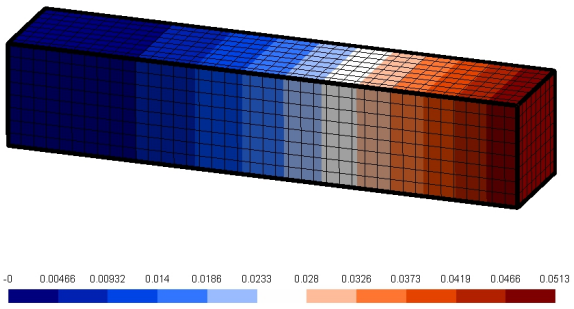

Fig. 23: deformation w [m]

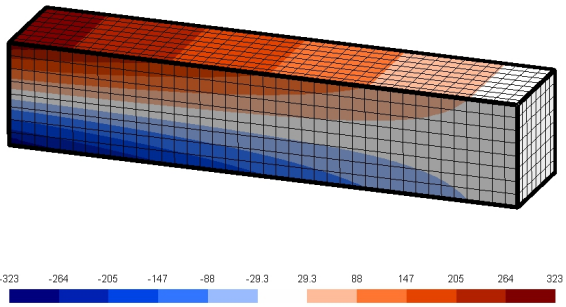

Fig. 24: normal stress σ_{xx} [kPa]

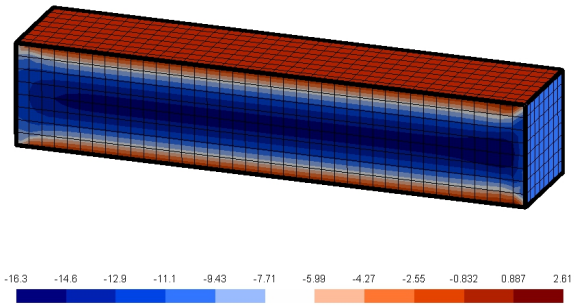

Fig. 25: shear stress τ_{xz} [kPa]

4.2.4 Interior results

Figure 26 shows the deflection curve $w(x)$ along the neutral axis (x- axis) obtained from the regularized and standard (non-regularized) formulation of the SDI for the coarsest mesh ("mesh 1"). It also includes the deflection curve $w(x)$ of the reference solution. By comparing numerical results with the reference solution it can be seen from the figure that the numerical results already are accurate using the coarsest mesh. Obviously, there is no difference between the deflection computed numerically and the reference solution. Only numerical results obtained from the standard formulation of the SDI become inaccurate near the loaded free end due to reasons discussed in Sections 4.1.4 and 3.3.3. On the other hand numerical results obtained from the regularized formulation of the SDI are accurate along the whole neutral axis due to elimination of the adverse influences of the singularities of the fundamental solutions near the boundary. Unlike expected non-regularized numerical results are not inaccurate near the fixed end. This is due to the prescribed displacement values (Dirichlet boundary conditions) to generate the fully restraint face for solving the BIE. Very tiny differences between numerical results and the reference solution can be obtained by having a closer look on the values. For example the deflection at $x = x_m = 2.5m$ obtained from the BEM-application for the coarsest mesh is $w(x_m)_{BEM} = 0.016227m$ for both the non-regularized and the regularized method whereas the evaluation of the reference solution at the same point yields $w(x_m)_{ref} = 0.016225m$. By comparing these values a difference only arise at the fifth significant digit, which may be interpreted as negligibly small.

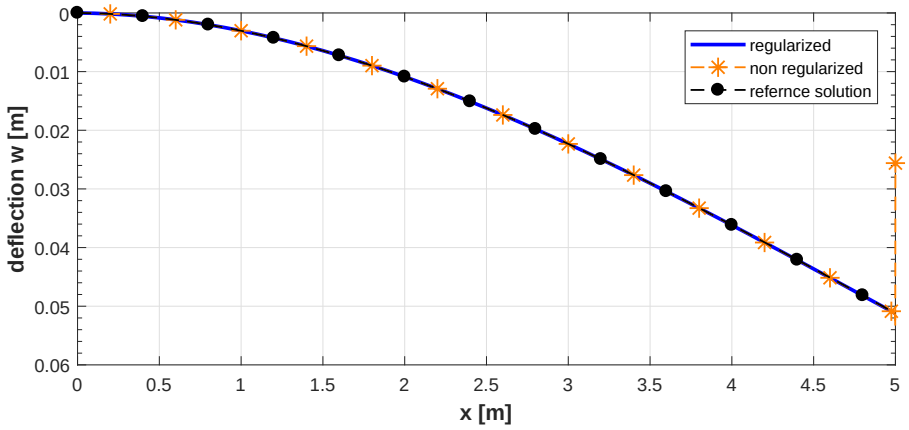

Fig. 26: deflection curve $w(x)$ along the neutral axis for "mesh 1"

Following two figures (Figure 27 and 28) show the distribution of the normal stress σ_{xx} and the shear stress τ_{xz} along the z-axis at $x = x_m = 2.5m$ (orange dashed line in Figure 19). The numerical results depicted in these figures are computed using the coarsest mesh ("mesh 1", 88 elements). Obviously, no difference can be recognized between the numerical results and the reference solution for normal stresses σ_{xx} and hardly any for shear stresses τ_{xz}. As expected, the results near the boundary obtained from the standard formulation of the SSI (non-regularized SSI) are unreliable.

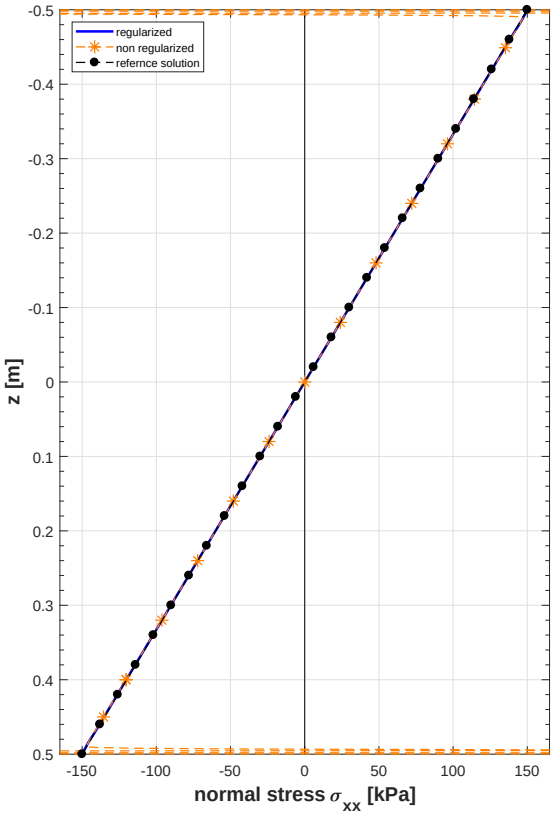

Fig. 27: normal stress σ_{xx} at $x = x_m = 2.5m$

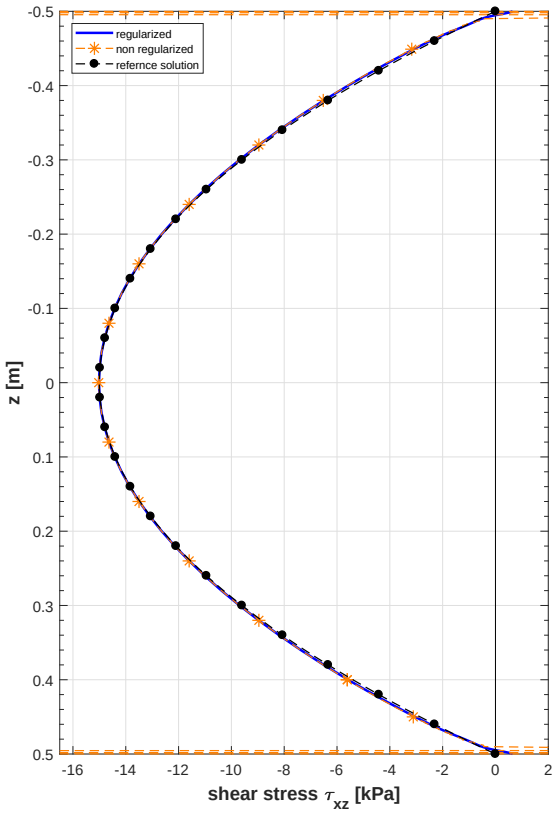

Fig. 28: shear stress τ_{xz} at $x = x_m = 2.5m$

Differences may be detected by taking a closer look at the interior results as provided in Figures 29 to 31. These figures show the distribution of normal stresses σ_{xx} and shear stresses τ_{xz} along the first $0.1m$ of the cross-sectional z-axis starting from the top ($z = -0.4$ to $-0.5m$) for "mesh 1", "mesh 2" and "mesh 3", respectively.

It can be detected from these figures that the deviation between normal stresses σ_{xx} obtained from the regularized formulation of the SSI and those obtained from the reference solution is already very small for the coarsest mesh ("mesh 1"). However, differences between the shear stresses τ_{xz} of the reference solution and those computed from the regularized SSI are larger for the same mesh as can be seen in Figure 29. This differences gradually decreasing the finer the mesh will be until hardly any or no differences arise for the finest mesh which results are displayed in Figure 31. Note also, the anomaly of regularized shear stresses τ_{xz} close to the boundary for "mesh 1" and "mesh 2", which may result due to inappropriate boundary results for shear stresses. Analogous to the improvement of normal stresses also this anomaly gradually disappears the finer the mesh will be, and thus, it do not occur for the finest mesh as can be seen in Figure 31. Moreover, the results of the non-regularized method are quite unreliable, above all very near the boundary. Note, the jagged curves of this results, which do not become quite better for finer meshes and the big inaccuracies of the results very near the boundary which are stronger than that obtained in the previous example (compression test). The higher complexity of this example may be the reason for that. Another reason may be that more subelements would be necessary to smooth the curve in the moderate jagged sections and to mitigate the adverse impacts of the singularities of the fundamental solutions. Such behaviours do not occur for regularized results which curves are smooth, also near the boundary. Note, non-regularized results were obtained with a limit of 50 subelements per element in this example.

In the end it can be said that for coarse meshes normal stresses obtained from the regularized formulations of the SSI tend to agree better with the reference than shear stresses, but if the discretization of the cantilever is sufficiently fine also shear stresses agree very well with the reference solution. Furthermore, hardly any or no differences between numerical results of both methods, regularization and standard formulation of the SSI, can be detected in an adequate distance from the boundary which considers sections of unreliable non-regularized results (jagged sections and sections very close to the boundary); e.g. no or hardly any differences between regularized and non-regularized normal stress results σ_{xx} can be detected for $z \geq -0.44$ in Figure 31.

An example of a cantilever beam in 3D and similar investigations of interior stresses computed from the regularized SSI also can be found in Reference [2]. However, regularized stress result obtained in this work are slightly better than in the reference. This may have different reasons whereas the main reason may be that in the reference quadrilateral elements with linear ansatz order were used for mesh generation. Another reason may be the different interpretation of the regularizing point P since in the reference it was assumed to be the closest node of the boundary element in contrary to the closest point of the element as defined in the present work.

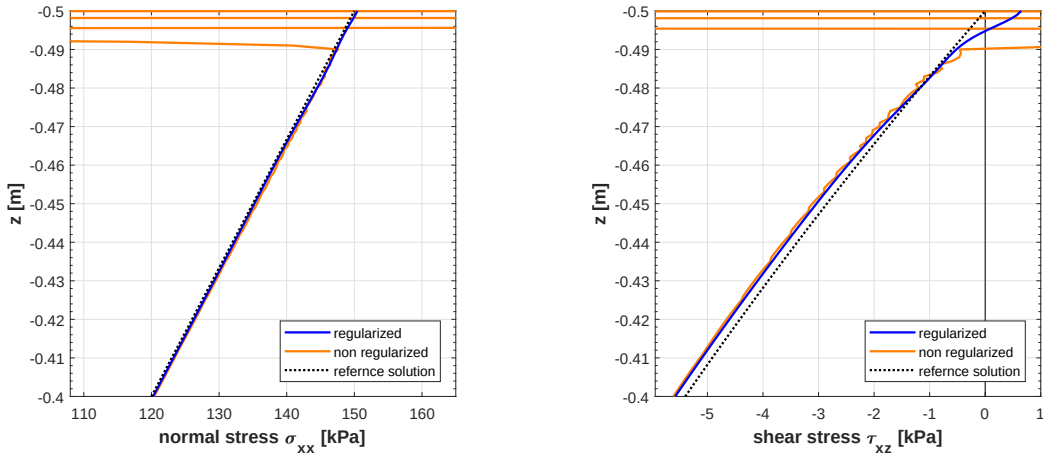

Fig. 29: "mesh 1": normal stress σ_{xx} and shear stress τ_{xz} at $x = x_m = 2.5m$

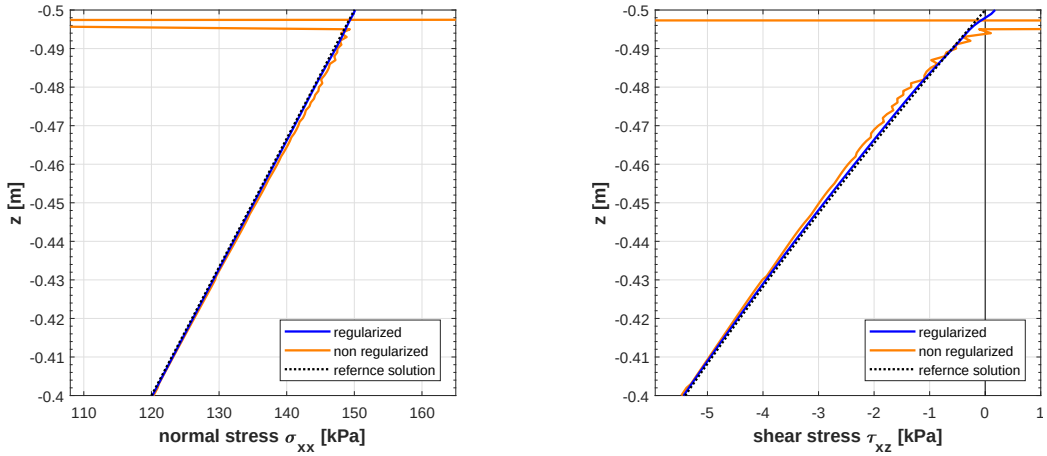

Fig. 30: "mesh 2": normal stress σ_{xx} and shear stress τ_{xz} at $x = x_m = 2.5m$

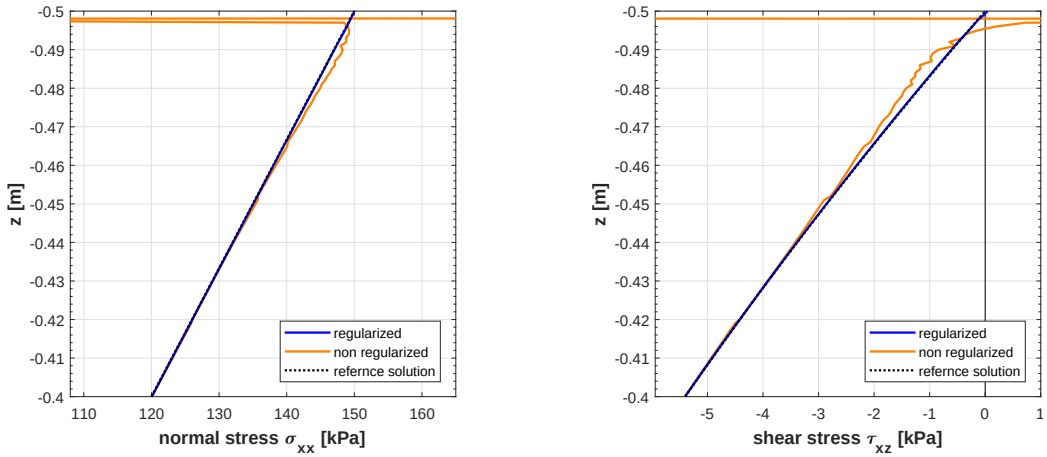

Fig. 31: "mesh 3": normal stress σ_{xx} and shear stress τ_{xz} at $x = x_m = 2.5m$

4.3 Thick walled pressurized cylinder in 3D

4.3.1 Introduction

The third example is a thick walled pressurized cylinder as shown in Figure 32. It is subjected to an uniform internal pressure $p_i = 1MPa$ and no external pressure ($p_e = 0$). The inner radius of the cylinder is taken to be $r_i = 1m$ and the outer (external) radius $r_e = 2m$. This yields a cylinder wall thickness $t = r_e - r_i = 1m$. The cylinder is made of steel with $E = 200000MPa$ as the Young's modulus and $\nu = 0.3$ as the Poisson's ratio. Due to double symmetry a quarter cylinder of length $L = 1m$ was cut out to compute numerical results. This can be seen in the right sketch of Figure 32. Plane strain conditions are assumed. As a consequence, Dirichlet boundary conditions as highlighted in blue in Figure 32 were chosen in such a way that the quarter cylinder can deform freely in radial direction while the deformations in y-direction are restraint. Quadrilateral serendipity elements with quadratic ansatz order were used to discretize the boundary of the domain, since the discretization error for this curved boundary is far smaller when using these elements rather than quadrilateral elements with linear ansatz order. Based on the mesh with ten elements as indicated in the right sketch of Figure 32, mesh refinements were carried out by dividing each element of the previous mesh into four elements whereby each previous element side is halved. This causes the number of elements to quadruple for each refinement. Thus, the meshes created in this example are consisting of 40 ("mesh 1"), 160 ("mesh 2") and 640 ("mesh 3") elements. The bold orange dashed line m in the right sketch of Figure 32, which is located at $y = y_m = 0.5m$ at an angle $\theta = 22.5°$, indicates the line along which interior results are calculated.

The same example in 2D also can be found in Reference [2].

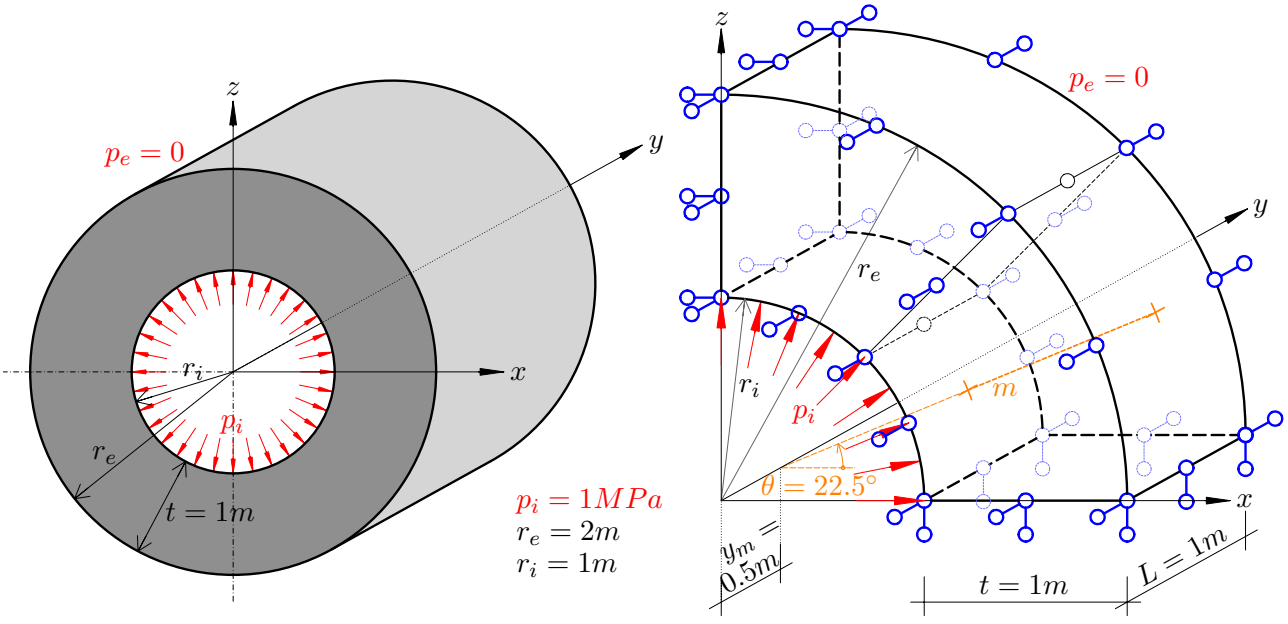

Fig. 32: Thick walled pressurized cylinder in 3D

4.3.2 Analytical solution

For thick walled cylinders such as long high pressure hydraulic pipes an analytical solution known as Lame's equations can be derived by assuming plane strain conditions. Moreover, an axis-symmetry about the y-axis is considered and the differential equations of stress equilibrium may be solved in polar coordinates. Hence, the radial deformation $u_r(r)$ for thick walled cylinders (inner radius r_i and outer radius r_e) subjected to an uniform internal and external pressure (p_i and p_e) may be written as a function of the variable radius r ($r_i \leq r \leq r_e$):

$$u_r(r) = \frac{1+\nu}{E}\left((1-2\nu)\frac{r_i^2 p_i - r_e^2 p_e}{r_e^2 - r_i^2} r + \frac{r_e^2 r_i^2 (p_i - p_e)}{r_e^2 - r_i^2}\frac{1}{r}\right) \tag{86}$$

where the pressures p_i and p_e have to be considered with positive sign. A negative sign for loadings would mean that the thick walled cylinder is subjected to tensile loadings as would arise at the inside when putting a cylindrical thick walled pipe under vacuum. Because of symmetry, no tangential deformations u_θ arise and the axial deformation $u_a \equiv u_y = 0$ due to the assumption of plane strain conditions. The principal radial stress $\sigma_{rr}(r)$ and the principal tangential stress $\sigma_{\theta\theta}(r)$, also known as circumferential or hoop stress, are also found to be functions of the variable radius r, whereas the axial stress $\sigma_{aa} \equiv \sigma_{yy}$ is constant:

$$\begin{aligned}
\sigma_{rr}(r) &= \frac{p_i r_i^2}{r_e^2 - r_i^2}\left(1 - \frac{r_e^2}{r^2}\right) - \frac{p_e r_e^2}{r_e^2 - r_i^2}\left(1 - \frac{r_i^2}{r^2}\right) \\
\sigma_{\theta\theta}(r) &= \frac{p_i r_i^2}{r_e^2 - r_i^2}\left(1 + \frac{r_e^2}{r^2}\right) - \frac{p_e r_e^2}{r_e^2 - r_i^2}\left(1 + \frac{r_i^2}{r^2}\right) \\
\sigma_{aa} &= \nu(\sigma_{rr} + \sigma_{\theta\theta}) = 2\nu\frac{p_i r_i^2 - p_e r_e^2}{r_e^2 - r_i^2} = const.
\end{aligned} \tag{87}$$

Note, radial stresses $\sigma_{rr}(r)$ always are compressive for pressurized thick walled cylinders while tangential stresses $\sigma_{\theta\theta}(r)$ may be tensile or compressive dependent on the load situation of the internal and external pressures p_i and p_e.

Instead of plane strain conditions plane stress conditions may be assumed as it would be the case for thick walled cylindrical pressure vessels. This does not change anything for radial and tangential stresses σ_{rr} and $\sigma_{\theta\theta}$. That is, the corresponding formulas in Equation (87) are valid for plane stress conditions, too. But, the radial deformation $u_r(r)$ is different from that based on plane strain conditions and an axial deformation $u_a(y)$ as a function of the y-coordinate arises instead of the axial stress σ_{aa} ($\sigma_{aa} = 0$):

$$\begin{aligned}
u_r(r) &= \frac{1-\nu}{E}\left(\frac{r_i^2 p_i - r_e^2 p_e}{r_e^2 - r_i^2}\right) r + \frac{1+\nu}{E}\left(\frac{r_e^2 r_i^2 (p_i - p_e)}{r_e^2 - r_i^2}\right)\frac{1}{r} \\
u_a(y) &= -\frac{2\nu}{E}\left(\frac{r_i^2 p_i - r_e^2 p_e}{r_e^2 - r_i^2}\right) y
\end{aligned} \tag{88}$$

In this example plane strain conditions are assumed as can be seen from the choice of the Dirichlet boundary conditions in Figure 32 which do not allow the cylinder to deform in axial direction (y-direction). Thus, Equations (86) and (87) are chosen to be the appropriate analytical solution for this problem. These equations further can be simplified for thick walled cylinders which are subjected

to internal pressure p_i only ($p_e = 0$). Simplification of the radial deformation $u_r(r)$ (Equation (86)) yields:

$$u_r(r) = \frac{1+\nu}{E}\left((1-2\nu)\frac{r_i^2 p_i}{r_e^2 - r_i^2}r + \frac{r_e^2 r_i^2 p_i}{r_e^2 - r_i^2}\frac{1}{r}\right) \tag{89}$$

The radial, tangential and axial stresses, $\sigma_{rr}(r)$, $\sigma_{\theta\theta}(r)$ and σ_{aa}, in Equation (87) can be simplified as follows:

$$\begin{aligned}
\sigma_{rr}(r) &= \frac{p_i r_i^2}{r_e^2 - r_i^2}\left(1 - \frac{r_e^2}{r^2}\right) \\
\sigma_{\theta\theta}(r) &= \frac{p_i r_i^2}{r_e^2 - r_i^2}\left(1 + \frac{r_e^2}{r^2}\right) \\
\sigma_{aa} &= 2\nu\frac{p_i r_i^2}{r_e^2 - r_i^2} = const.
\end{aligned} \tag{90}$$

where the tangential stress $\sigma_{\theta\theta}$ always is tensile in case thick walled cylinders subjected to internal pressure p_i only.

Figure 33 provides the distribution of radial, tangential and axial stresses, $\sigma_{rr}(r)$, $\sigma_{\theta\theta}(r)$ and σ_{aa}, and the distribution of radial deformations $u_r(r)$ within the wall of a thick walled cylinder subjected to internal pressure p_i only. For the given cylinder problem, values were computed at the inner and outer radius r_i and r_e as well as at the mean radius $r_m = (r_e + r_i)/2 = r_i + t/2 = 1.5m$.

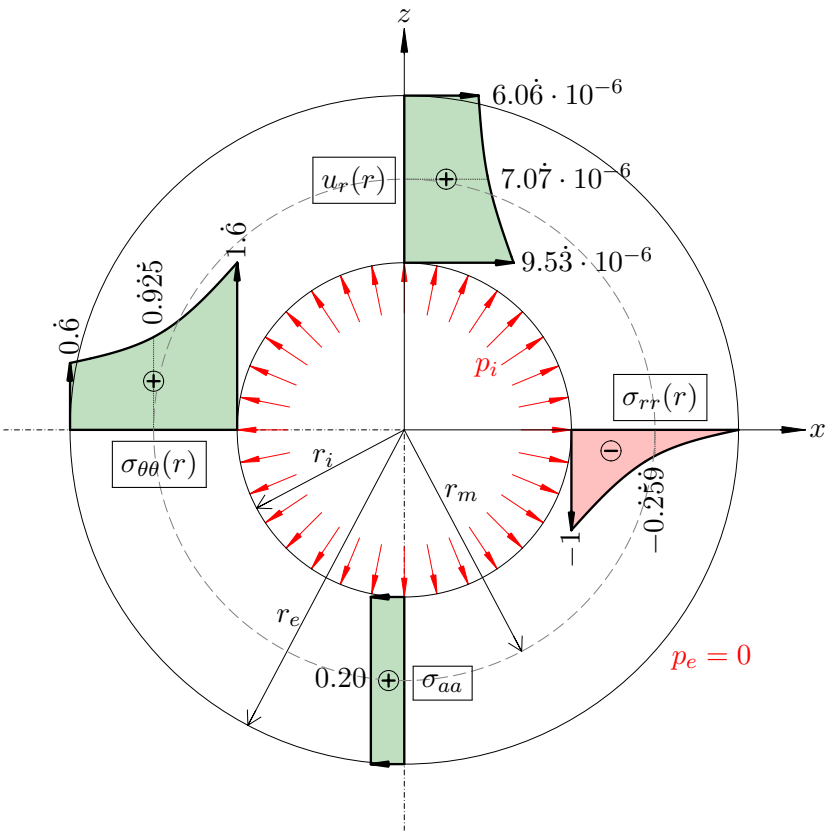

Fig. 33: distribution of $\sigma_{rr}(r)$, $\sigma_{\theta\theta}(r)$ and σ_{aa} (values in [MPa]) and $u_r(r)$ (values in [m])

4.3.3 Boundary results

Following figures provide numerical boundary results of the given thick walled cylinder. They are computed with the finest mesh ("mesh 3"). Figure 34 depicts the radial stress field σ_{rr}, Figure 35 the tangential stress field $\sigma_{\theta\theta}$, Figure 36 the axial stress field σ_{aa} and Figure 37 the radial deformation field u_r.

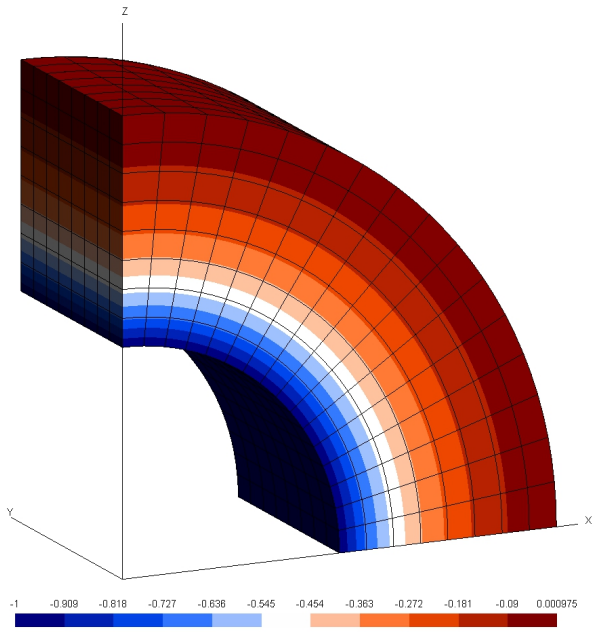

Fig. 34: radial stress σ_{rr} in [MPa]

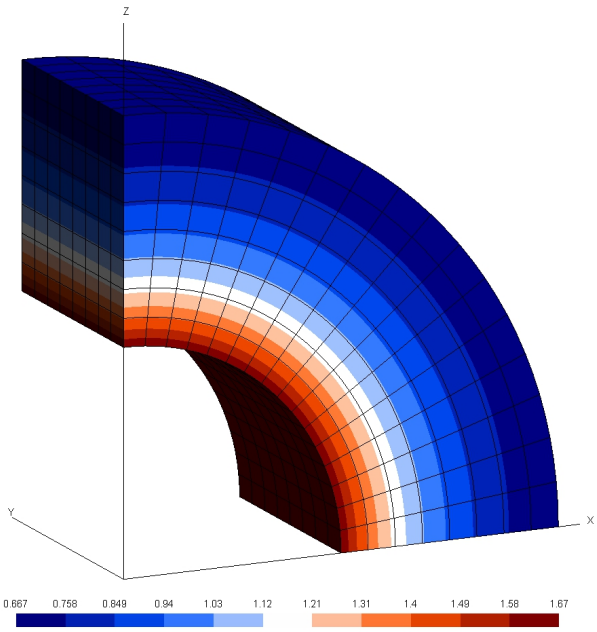

Fig. 35: tangential stress $\sigma_{\theta\theta}$ in [MPa]

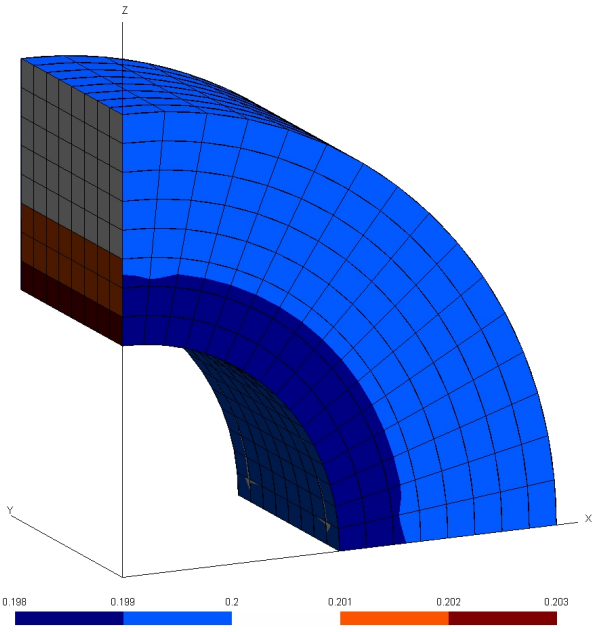

Fig. 36: axial stress σ_{aa} in [MPa]

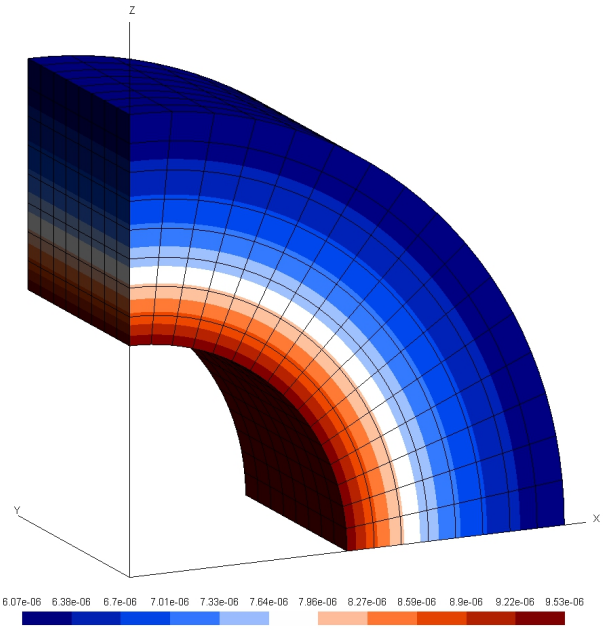

Fig. 37: radial deformation u_r in [m]

As can be seen from these figures, numerical results agree very well with the analytical solution. Only numerically computed axial stresses σ_{aa} in Figure 36 do not seem to agree quite well with the analytical solution at the first sight. But, the values of the colour scale indicate that the numerical results just slightly vary around the expected constant axial stress of the analytical solution which is $\sigma_{aa} = 0.2MPa$. By comparing the values of numerically computed radial stresses σ_{rr}, tangential stresses $\sigma_{\theta\theta}$ and radial deformations u_r at the inside and outside of the quarter cylinder with the corresponding ones in Figure 33 hardly any or no differences between numerical and analytical results may be detected. In general, also their distribution corresponds to those of the analytical solution since it is recognisable by the colour gradients that the results, as they do in the analytical solution too, increasing or decreasing faster near the inside than near the outside of the cylinder. (Compare Figure 33 with Figures 34, 35 and 37).

Boundary results for the same example calculated in 2D can be found in Reference [2] as well.

4.3.4 Interior results

The next figures provide an overview of interior results evaluated with the finest mesh ("mesh 3") along line m which is indicated by the bold orange dashed line in Figure 32. Figure 38 shows radial stresses σ_{rr}, Figure 39 tangential stresses $\sigma_{\theta\theta}$ and Figure 40 radial deformations u_r. Additionally, the corresponding distribution of the analytical solution is displayed in each graph for comparison.

As is evident from these figures, both numerical computed displacements and stresses agree very well with the equivalent analytical solution. Nevertheless, some small deviations may be detected by having a closer look at the results as outlined in the next section and, as usual, non-regularized results become inaccurate close to the boundary due to the singular behaviour of the fundamental solutions.

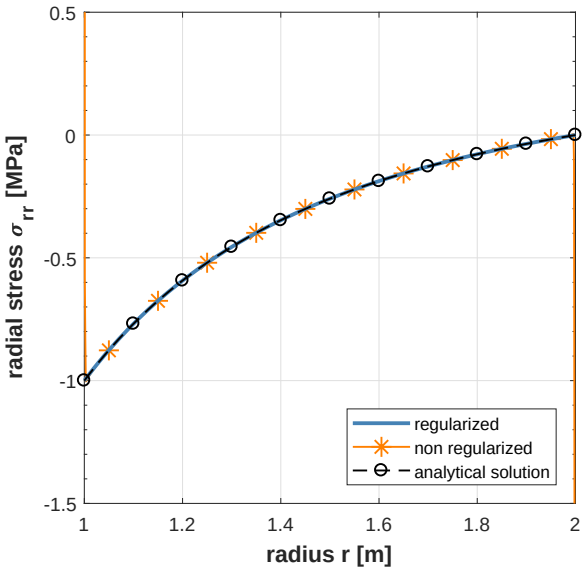

Fig. 38: radial stress σ_{rr} along line m

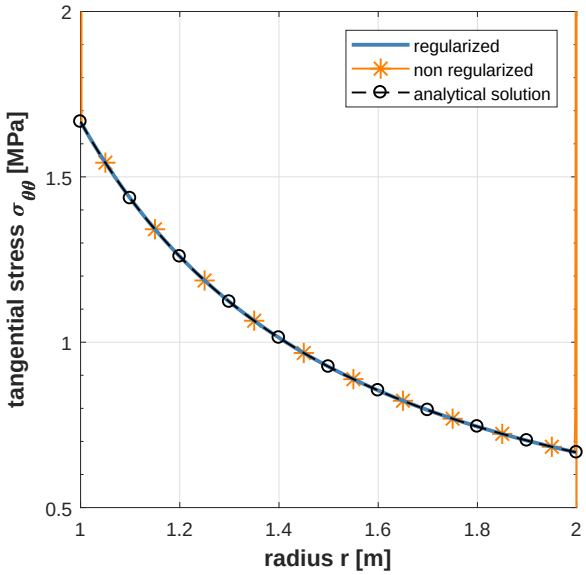

Fig. 39: tangential stress $\sigma_{\theta\theta}$ along line m

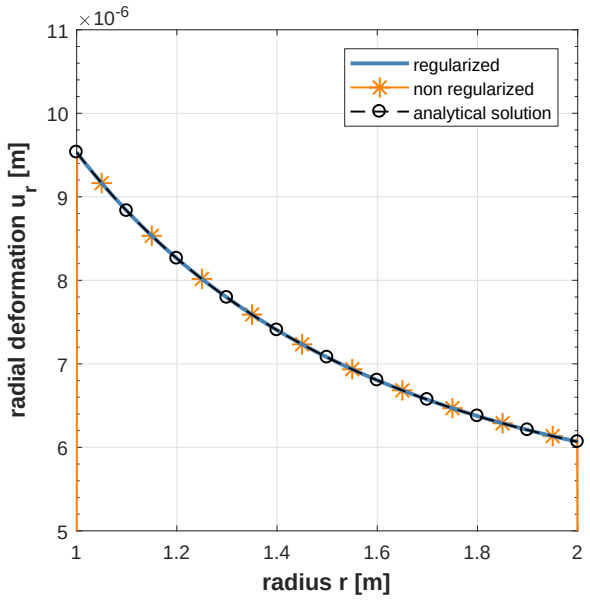

Fig. 40: radial deformation u_r along line m

4.3.5 Convergence study

In this section a convergence study will be shown and discussed. Therefore, numerical results in terms of absolute differences ϵ are displayed in following figures. Each figure contains graphs which illustrate the absolute difference in radial stresses σ_{rr}, tangential stresses $\sigma_{\theta\theta}$ and radial displacements u_r of one mesh. Thus, Figures 41, 42 and 43 show results computed using the coarsest mesh ("mesh 1"), "mesh 2" and the finest mesh ("mesh 3), respectively. Moreover, only results near the inside of the cylinder are plotted in these figures $(r_i \leq r \leq (r_i + 0.1m) : 1m \leq r \leq 1.1m)$. The absolute difference ϵ_p at any point p is defined as follows.

$$\epsilon_p = \left| \frac{f_{p,BEM} - f_{p,analytical}}{f_{p,analytical}} \right| \cdot 100 \quad ... \quad \text{in } [\%] \tag{91}$$

were $f_{p,BEM}$ represents the value, which is a stress or displacement value, at any point p evaluated numerically using the regularized or standard formulations of the Somigliana Identities and $f_{p,analytical}$ is the corresponding value of the analytical solution.

Generally it can be seen from the figures that the absolute differences ϵ approaching zero at a certain distance away from the boundary dependent on the mesh refinement. Furthermore, as already figured out in the previous example, displacements converging better towards the analytical solution than stresses. For numerically computed stresses finer meshes are required to achieve the same quality as for numerical displacement results; e.g. applying the regularized Somigliana Identities for numerical computation, "mesh 2" is required to obtain a quite equivalent error margin for radial stresses σ_{rr} as for displacements u_r computed with "mesh 1" (Compare the corresponding results in Figures 41 and 42). The reason may be that the order of singularities of the fundamental solutions in the SSI is one degree higher than the order of singularities of their counterparts in the SDI. For regularized stress results especially the determination of the regularizing stress $\boldsymbol{\sigma}(P)$ play a role, too. It is recovered from boundary tractions and displacements which are obtained from the displacement form of the

BIE as outlined in Section 3.6. This is accompanied by an increasing inaccuracy in the regularizing stress. A direct evaluation of boundary stresses based on the stress form of the BIE which can be derived from the SSI might mitigate that problem. Nevertheless, results obtained with the regularized formulations of the Somigliana Identities near the boundary are very accurate, though some very small differences above all in tangential stresses $\sigma_{\theta\theta}$ still arise for the finest mesh in Figure 43. In addition to what is already mentioned above such differences might arise due to the discretization error done for such a curved domain and even though the regularization mitigates the singular behaviour of the Somigliana Identities near the boundary very well, small influences of the singularities might not be excluded. However, these differences would decrease until they are extremely small when using finer meshes than those used in this convergence study. Moreover, also integration errors may impact the accuracy of numerical results. They may be reduced by increasing the number of Gauss points. But, in the end it can be said that with the regularized formulations of the Somigliana Identities very accurate results can be achieved with the finest mesh since the maximum absolute difference which is obtained for tangential stresses $\sigma_{\theta\theta}$ very near the boundary is lower than 0.2% and therefore very small. Differences in radial stresses σ_{rr} only may be detected when looking very carefully and no differences may be recognisable in radial deformations u_r computed with the finest mesh. The graphs also emphasize the inaccuracy of the standard, non-regularized Somigliana Identities near the boundary as the absolute differences are out of range within a certain distance from the boundary. Note, the maximal number of subelements in each intrinsic direction was set to 50 as usual.

Error graphs of interior results, similar as depicted in the figures below, can be found in Reference [2] for the same thick walled cylinder calculated in 2D. The results in the reference show the same behaviour as in the corresponding figures of this work.

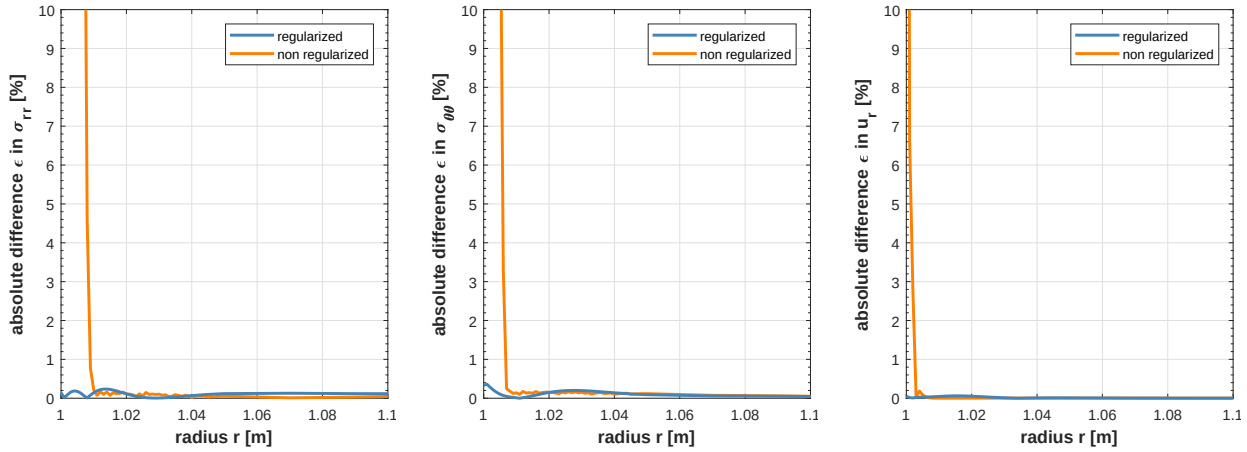

Fig. 41: "mesh 1" (coarsest mesh, 40 elements): absolute difference in σ_{rr}, $\sigma_{\theta\theta}$ and u_r

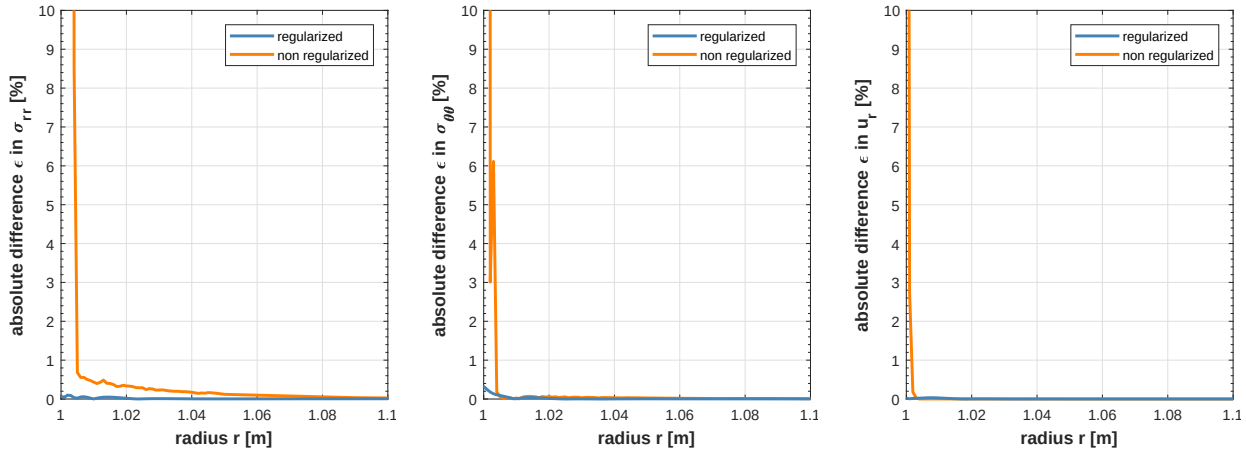

Fig. 42: "mesh 2" (160 elements): absolute difference in σ_{rr}, $\sigma_{\theta\theta}$ and u_r

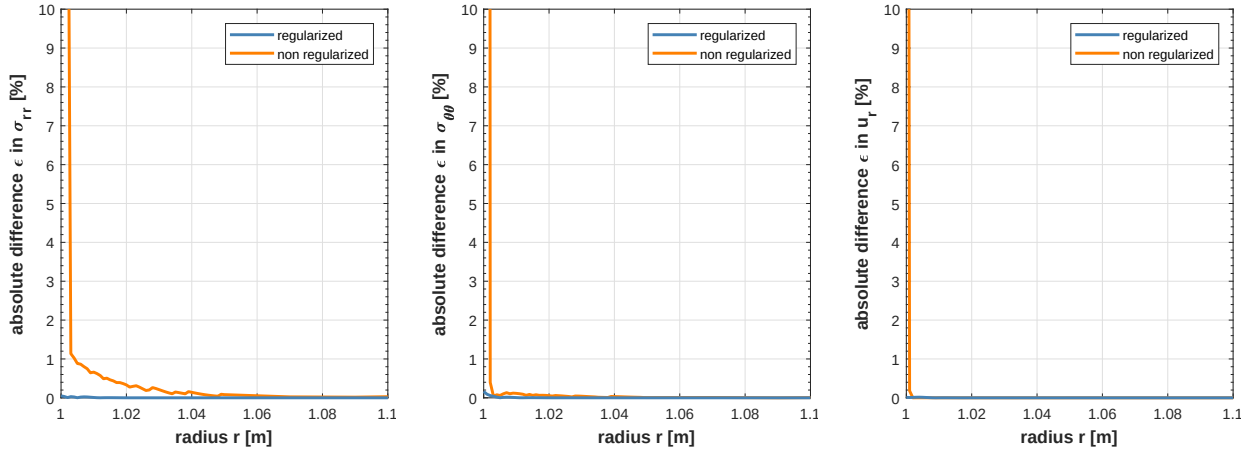

Fig. 43: "mesh 3" (finest mesh, 640 elements): absolute difference in σ_{rr}, $\sigma_{\theta\theta}$ and u_r

4.4 Tunnel in 3D

4.4.1 Introduction

As a last example a circular tunnel (Figure 44) with radius $R = 1m$ which will be driven at a depth $H = 1000m$ measured from the ground surface to the tunnel axis is analysed using the implemented BEM-application. Excavation induced displacements and stresses around the tunnel will be investigated. The tunnel will be driven in granite rock having a Young's modulus $E = 80000MPa$, a Poisson's ratio $\nu = 0.25$ and a specific weight $\gamma = 30kN/m^3$. The shear modulus $G = 32000MPa$ can be derived from E and ν. A constant virgin stress state as can be seen in Figure 44 is assumed. The major principal stress σ_y is taken to be the vertical compressive in situ stress $\sigma_v = \gamma \cdot H = 30MPa$ which is the weight of the overburden. Assuming a lateral earth pressure coefficient at rest $k = 0.5$ will give the horizontal compressive in situ stress $\sigma_h = k \cdot \sigma_v = 15MPa$ which is considered to be the minor principal stress $\sigma_x = \sigma_z$. For numerical calculation the tunnel surface is decomposed into quadrilateral serendipity elements with quadratic ansatz order. Since no infinite elements are used in the code the tunnel has closed ends and the length is taken to be $L = 20m$. Moreover, the boundary of the ground surface will not have any influence on the results, since the tunnel will be driven at great depth, and therefore, an infinite extended domain is assumed. Due to this assumption this example verifies the analytical solutions of the integrals over a boundary at infinity which arise in the regularized formulation of the Somigliana Identity for infinite domains. The meshes which are used in this example consists of 416 ("mesh 1"), 736 ("mesh 2") and 1472 ("mesh 3") elements and are shown in Figures 45, 46 and 47, respectively. Additionally, interior results are computed along a circle m^* with radius $r^* = 1.005m$ and along a line l^* as indicated by orange dashed lines in Figure 44. Both are located at $z = z^* = 10m$.

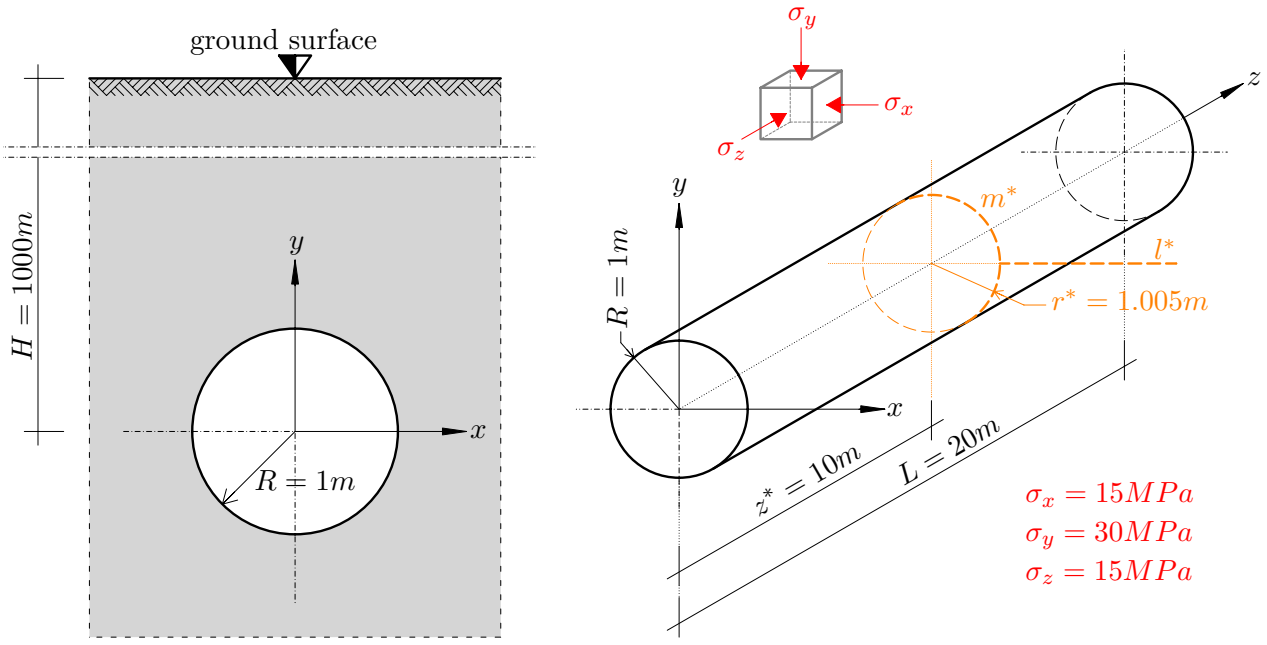

Fig. 44: Tunnel in 3D

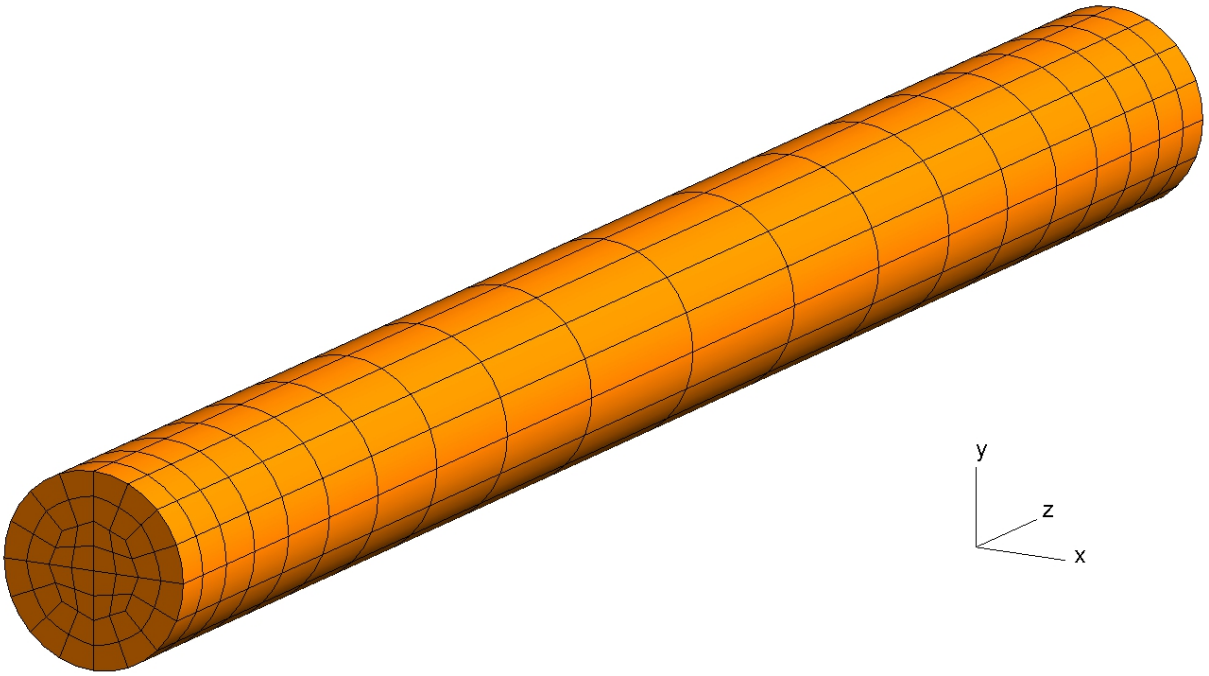

Fig. 45: "mesh 1" - 416 elements

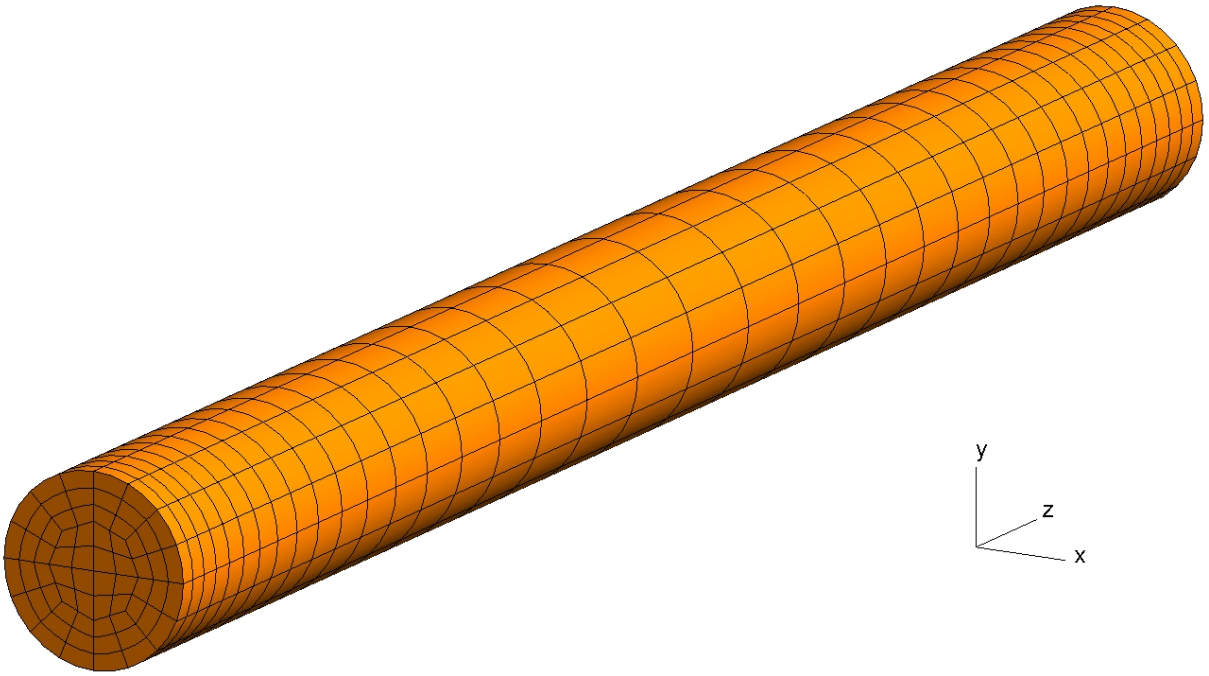

Fig. 46: "mesh 2" - 736 elements

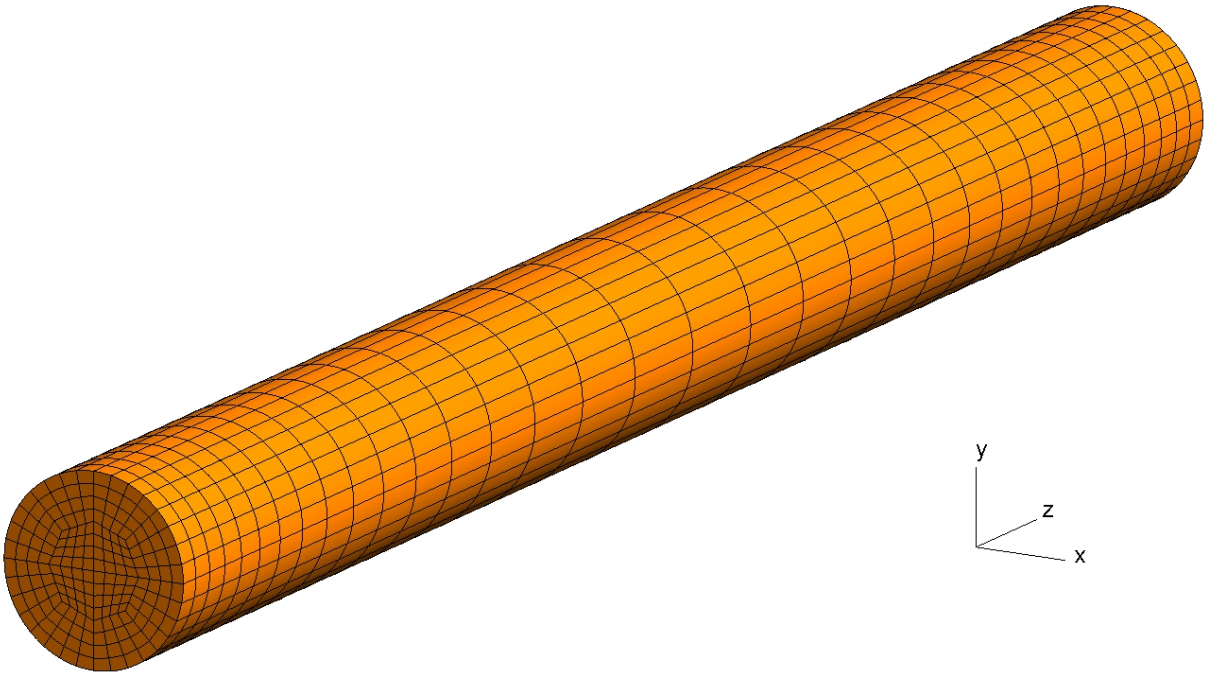

Fig. 47: "mesh 3" - 1472 elements

4.4.2 Reference solution

Excavation induced stresses and displacements around a circular tunnel may be analysed assuming plane strain conditions (infinite long tunnel) and using Kirsch's equations. These equations originally provide an analytical solution for the elastic stress and displacement distributions around a circular hole of radius R in a biaxial stressed infinite plate. The equations may be expressed in terms of polar coordinates $(r,\ \theta)$. The point of interest p is described by the radius $r \geq R$ and the angle θ as defined in Figure 48. Thus, the radial displacement $u_r(r,\theta)$ and the circumferential displacement $u_\theta(r,\theta)$ can be written as follows:

$$\begin{aligned} u_r(r,\theta) &= \frac{\sigma_v R^2}{4rG}\left[(1+k)-(1-k)\left(4(1-\nu)-\frac{R^2}{r^2}\right)cos(2\theta)\right] \\ u_\theta(r,\theta) &= \frac{\sigma_v R^2}{4rG}\left[(1-k)\left(2(1-2\nu)+\frac{R^2}{r^2}\right)sin(2\theta)\right] \end{aligned} \tag{92}$$

And the set of equations for stresses is:

$$\begin{aligned} \sigma_{rr}(r,\theta) &= \frac{\sigma_v}{2}\left[(1+k)\left(1-\frac{R^2}{r^2}\right)-(1-k)\left(1-4\frac{R^2}{r^2}+3\frac{R^4}{r^4}\right)cos(2\theta)\right] \\ \sigma_{\theta\theta}(r,\theta) &= \frac{\sigma_v}{2}\left[(1+k)\left(1+\frac{R^2}{r^2}\right)+(1-k)\left(1+3\frac{R^4}{r^4}\right)cos(2\theta)\right] \\ \tau_{r\theta}(r,\theta) &= \frac{\sigma_v}{2}\left[(1-k)\left(1+2\frac{R^2}{r^2}-3\frac{R^4}{r^4}\right)sin(2\theta)\right] \end{aligned} \tag{93}$$

where $\sigma_{rr}(r,\theta)$ refers to radial stresses, $\sigma_{\theta\theta}(r,\theta)$ to circumferential stresses (also known as tangential or hoop stresses) and $\tau_{r\theta}(r,\theta)$ to shear stresses. Furthermore, k in Equations (92) and (93) is defined as the ratio between horizontal and vertical stress, σ_h and σ_v. It is the assumed lateral earth pressure coefficient at rest $k = 0.5$.

$$k = \frac{\sigma_h}{\sigma_v} \tag{94}$$

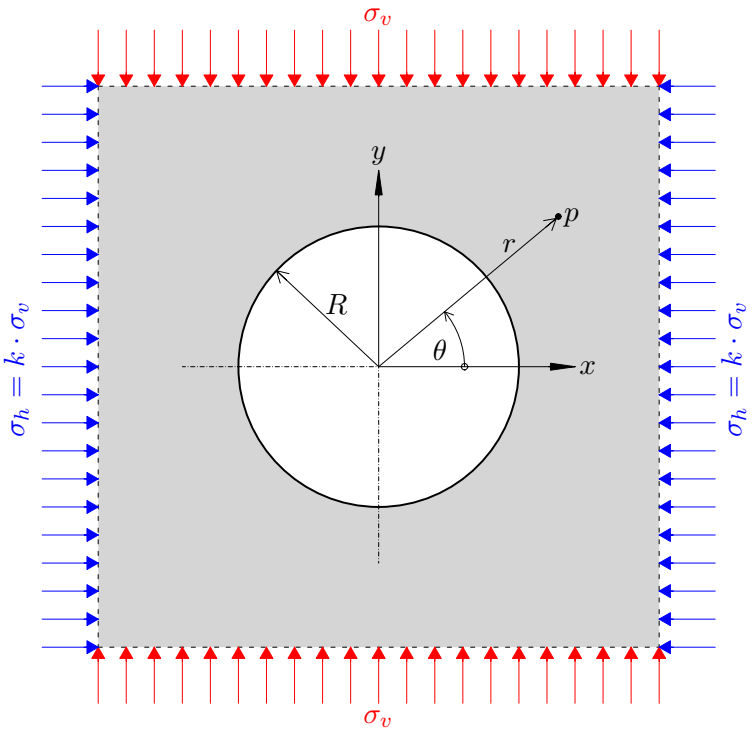

Fig. 48: biaxial stressed infinite plate or tunnel in 2D

The displacements and stresses in Equations (92) and (93) may be transformed into a cartesian system (x, y) by applying displacement and stress transformation which use a rotation matrix $\mathbf{Q}$. The transformation for displacements may be written as follows:

$$\mathbf{u}' = \mathbf{Q} \cdot \mathbf{u} \quad \rightarrow \quad \begin{Bmatrix} u_x \\ u_y \end{Bmatrix} = \begin{bmatrix} cos(\theta) & -sin(\theta) \\ sin(\theta) & cos(\theta) \end{bmatrix} \cdot \begin{Bmatrix} u_r \\ u_\theta \end{Bmatrix} \tag{95}$$

and the stress transformation from the polar system into the cartesian one is:

$$\boldsymbol{\sigma}' = \mathbf{Q} \cdot \boldsymbol{\sigma} \cdot \mathbf{Q}^T \quad \rightarrow \quad \begin{bmatrix} \sigma_{xx} & \tau_{xy} \\ \tau_{xy} & \sigma_{yy} \end{bmatrix} = \begin{bmatrix} cos(\theta) & -sin(\theta) \\ sin(\theta) & cos(\theta) \end{bmatrix} \cdot \begin{bmatrix} \sigma_{rr} & \tau_{r\theta} \\ \tau_{r\theta} & \sigma_{\theta\theta} \end{bmatrix} \cdot \begin{bmatrix} cos(\theta) & sin(\theta) \\ -sin(\theta) & cos(\theta) \end{bmatrix} \tag{96}$$

Now, by evaluating Equation 95 the displacements u_x and u_y in x- and y- direction are:

$$\begin{aligned} u_x &= u_r \cdot cos(\theta) - u_\theta \cdot sin(\theta) \\ u_y &= u_r \cdot sin(\theta) + u_\theta \cdot cos(\theta) \end{aligned} \tag{97}$$

The normal stresses σ_{xx} and σ_{yy} and the shear stress τ_{xy} can be obtained by applying the stress transformation of Equation (96) and appropriate trigonometric identities. Consequently, they may be written as follows:

$$\begin{aligned}\sigma_{xx} &= \frac{\sigma_{rr}+\sigma_{\theta\theta}}{2} + \frac{\sigma_{rr}-\sigma_{\theta\theta}}{2} cos(2\theta) - \tau_{r\theta} \cdot sin(2\theta) \\ \sigma_{yy} &= \frac{\sigma_{rr}+\sigma_{\theta\theta}}{2} - \frac{\sigma_{rr}-\sigma_{\theta\theta}}{2} cos(2\theta) + \tau_{r\theta} \cdot sin(2\theta) \\ \tau_{xy} &= \frac{\sigma_{rr}-\sigma_{\theta\theta}}{2} sin(2\theta) + \tau_{r\theta} \cdot cos(2\theta)\end{aligned} \tag{98}$$

In this example the closed ends of the tunnel might slightly influence the region in the middle of the tunnel ($z = L/2$) where numerical interior results will be computed. Thus, plane strain conditions might not be completely satisfied in that region and therefore, Kirsch's equations are considered to be the reference solution for this example (and not the analytical one!).

Table 2 provides displacement and stress values at the boundary ($r = R = 1m$) evaluated with the formulas of the reference solution in Equations (97) and (98) for angles θ of 0°, 45°and 90°, respectively.

θ	u_x [m]	u_y [m]	σ_{xx} [MPa]	σ_{yy} [MPa]	τ_{xy} [MPa]
0°	$-1.17 \cdot 10^{-4}$	0	0	-75.0	0
45°	$-0.83 \cdot 10^{-4}$	$-4.14 \cdot 10^{-4}$	-22.5	-22.5	22.5
90°	0	$-5.86 \cdot 10^{-4}$	-15.0	0	0

Tab. 2: evaluated reference solution at the boundary ($r = R = 1m$) for different anlges θ

4.4.3 Boundary results

Figures 49 to 53 provide boundary results calculated with the finest mesh ("mesh 3"). The displacement fields u_x and u_y can be found in Figures 49 and 50, respectively. Figure 51 shows the normal stress distribution σ_{xx} over the boundary, Figure 52 that of the normal stresses σ_{yy} and Figure 53 displays the shear stress field τ_{xy}.

These figures clearly show the influence of the closed tunnel ends as the displacements u_x and u_y are tending towards zero at the ends due to supporting effects of the rock mass behind while the compressive normal stresses σ_{xx} and σ_{yy} are increasing at the closed tunnel ends because of singular stress behaviour at corners. On the other hand, the contour lines (isolines) of both displacements and stresses are running quite parallel to the z-axis from a sufficient distance from the tunnel ends which indicates that plane strain conditions are fairly well satisfied in the region where interior results are computed. Moreover, value ranges and its location on the boundary in terms of the angle θ can be obtained from the results depicted in Figures 49 to 53. This more or less allows to compare numerically determined boundary results with the results of the reference solution provided in Table 2. It shows that numerically computed boundary results agree quite well with the reference solution, that is, the relevant value ranges include the corresponding values expected from the reference solution at the same location; e.g. Table 2 indicates a deformation $u_x = -1.17 \cdot 10^{-4}$ at an angle $\theta = 0°$ which lies within the corresponding value range of -0.00012 to $-9.7 * 10 \cdot 10^{-5}$ obtained from Figure 49 at the same location (red area); or, as a second example, the same table gives $u_x = 0$ at the crown ($\theta = 90°$), and obviously there is a contour line in Figure 49 at the corresponding location indicating

an infinitesimal small value of $-1.2 \cdot 10^{-13}$ which may be interpreted to be $u_x = 0$ and thus agreeing with the reference solution.

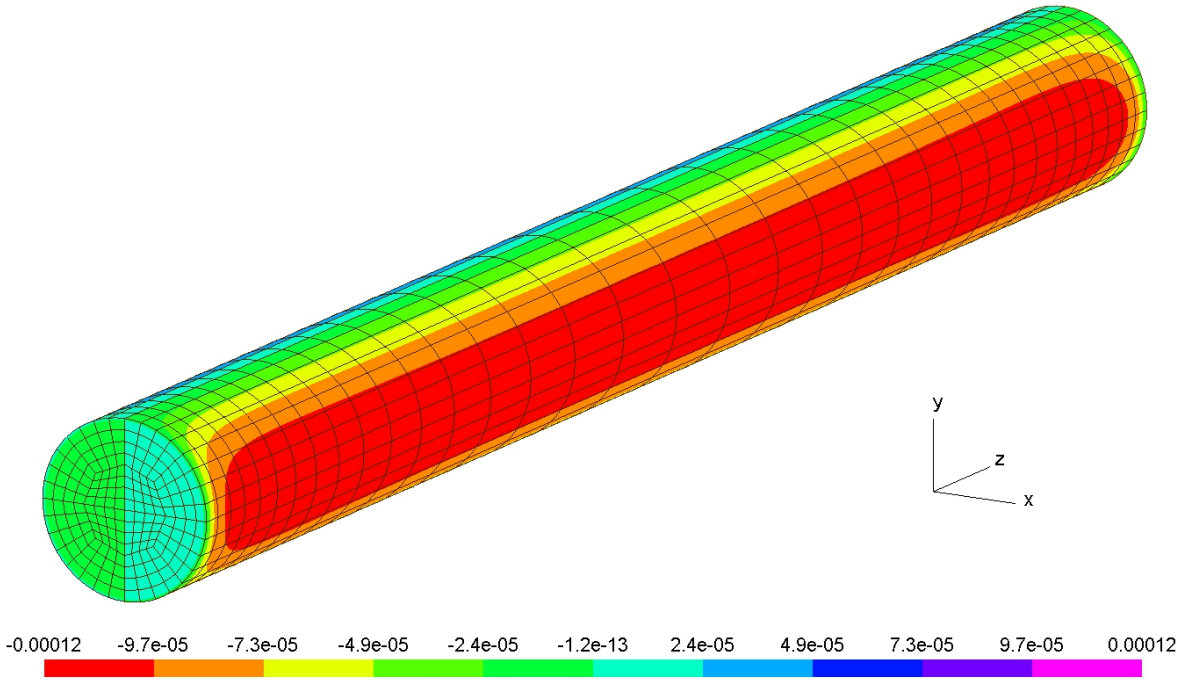

Fig. 49: displacement field u_x [m]

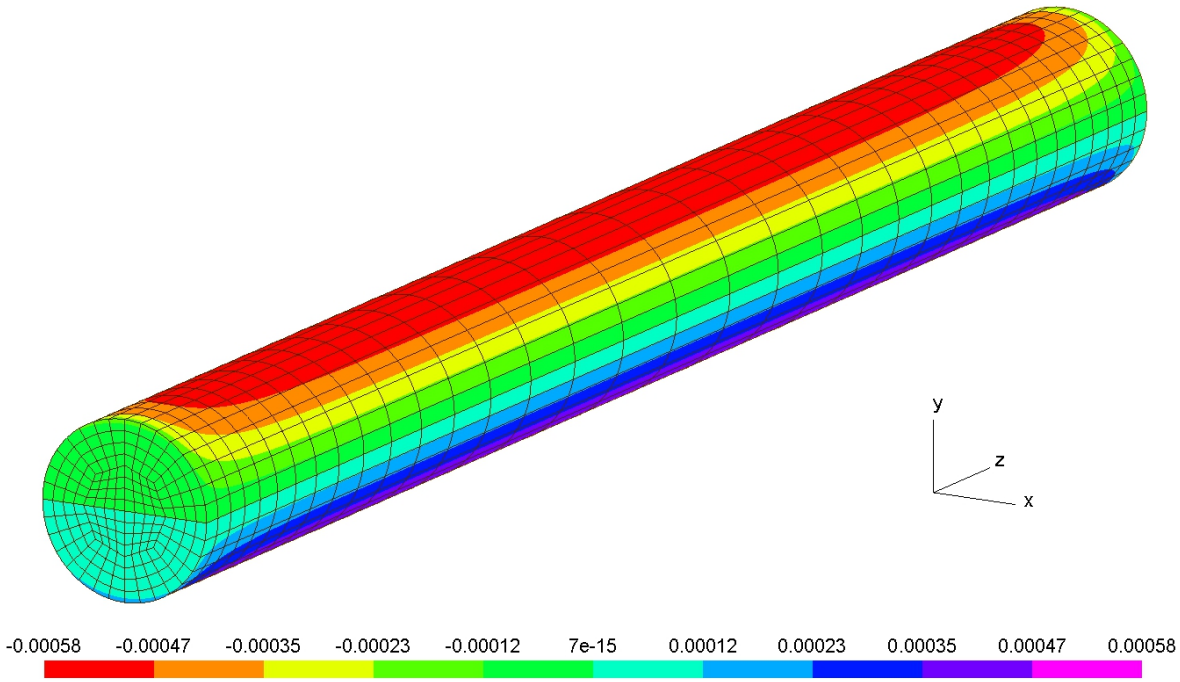

Fig. 50: displacement field u_y [m]

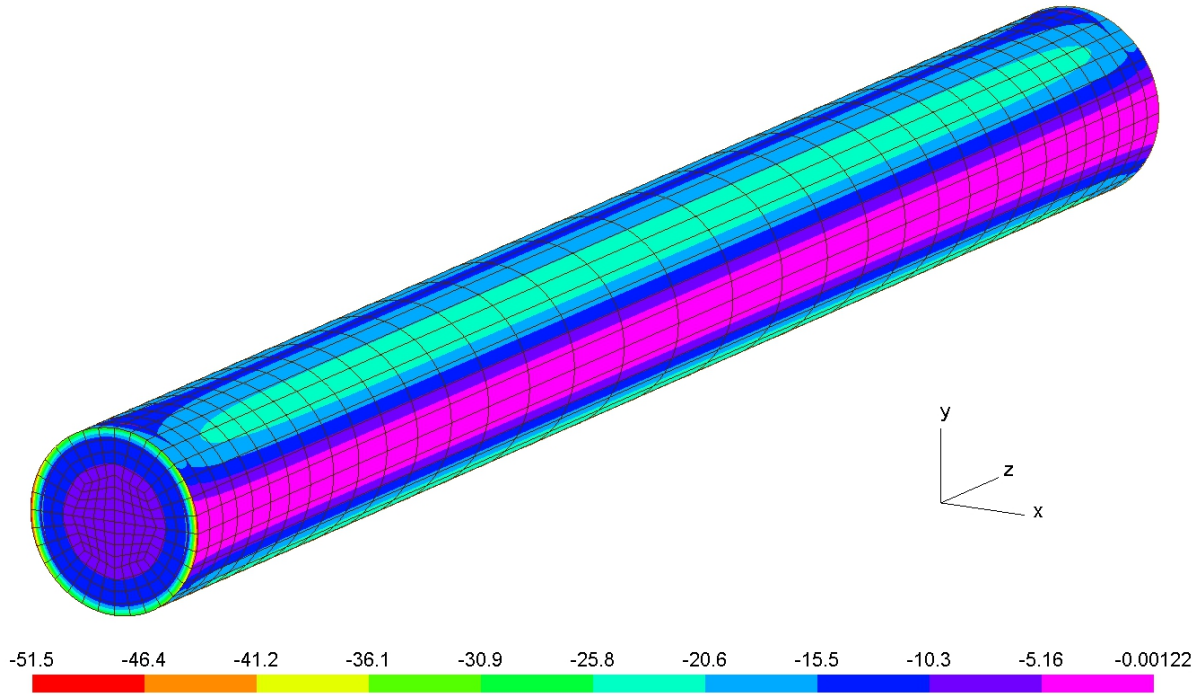

Fig. 51: normal stress field σ_{xx} [MPa]

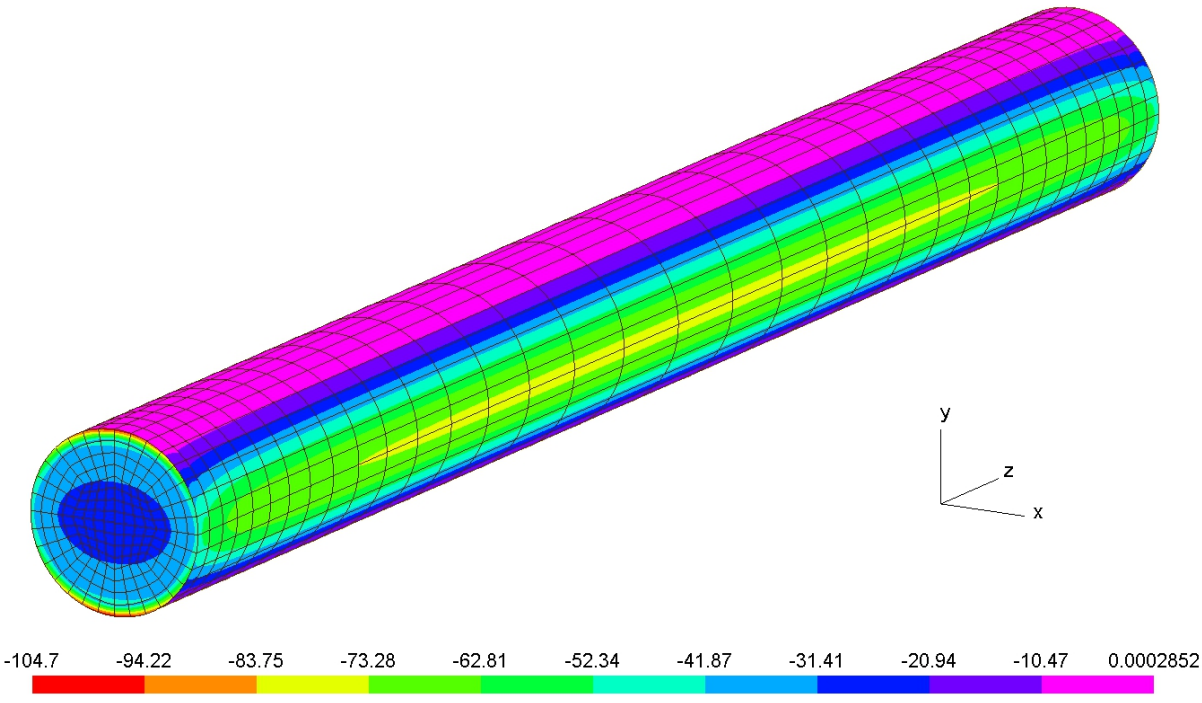

Fig. 52: normal stress field σ_{yy} [MPa]

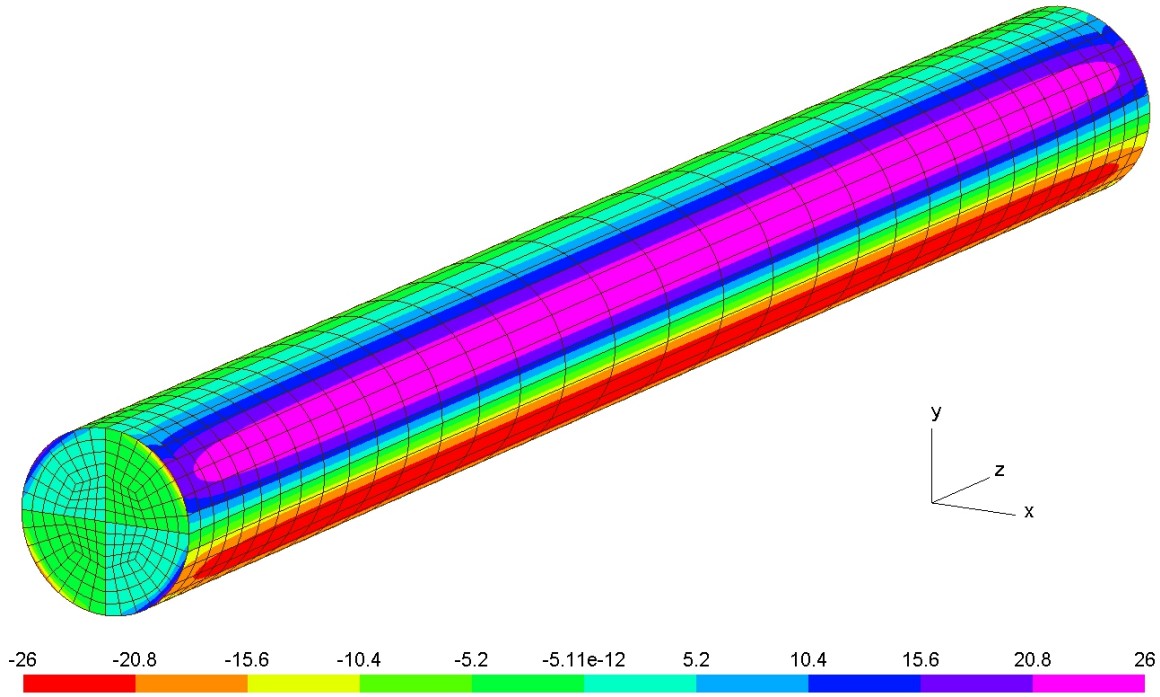

Fig. 53: shear stress field τ_{xy} [MPa]

4.4.4 Interior results along a horizontal line

Figures 54 to 56 provide graphs displaying the distributions of numerically determined interior results as well as the distributions of the corresponding Kirsch's solutions along line l^* which is defined in Figure 44. The normal stresses σ_{xx} and σ_{yy} are presented in Figures 54 and 55, respectively, and the displacements u_x are shown in Figure 56. Stresses along this line are principal stresses and therefore, shear stresses $\tau_{xy} = 0$. Furthermore, displacements u_y are zero due to symmetry.

The stress distributions in Figures 54 and 55 clearly illustrates the general stress behaviour in the material (rock) around the tunnel as the stresses σ_{xx} and σ_{yy} approaching the corresponding far-field stresses (primary stresses) $\sigma_x = -15MPa$ and $\sigma_y = -30MPa$ with increasing distance from the tunnel surface. The same behaviour can be seen for displacements u_x in Figure 56 as they have to converge towards $u_x = 0$ at infinity. Moreover, apart from the inaccuracies of numerical results obtained from the non-regularized standard formulations of the Somigliana Identities near the boundary, numerical results agree quite well with the reference solution. However, significant differences between the reference solution and numerical results arise for displacements u_x from a distance of about $0.5m$ from the boundary ($x > 1.5m$). This might be because plane strain conditions are not completely satisfied. On the other hand, this has little or no influence on stresses since hardly any differences arise between numerically computed stresses and stresses obtained from Kirsch's equations in Figures 54 and 55.

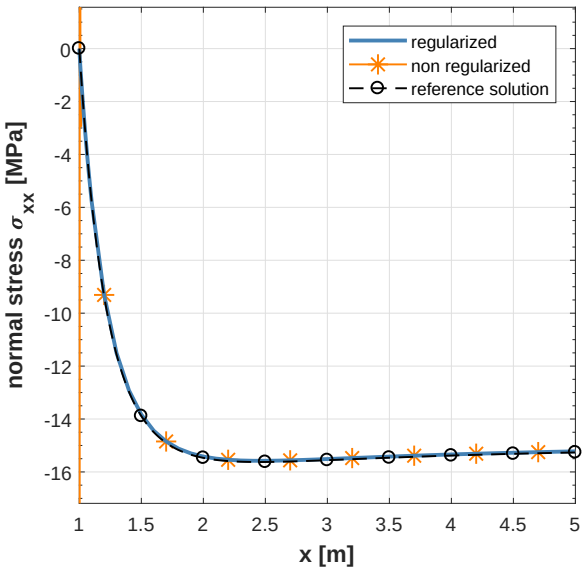

Fig. 54: normal stress σ_{xx} along line l^*

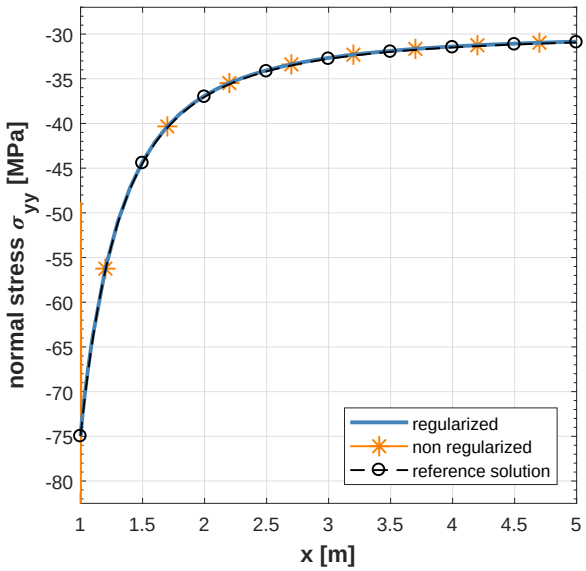

Fig. 55: normal stress σ_{yy} along line l^*

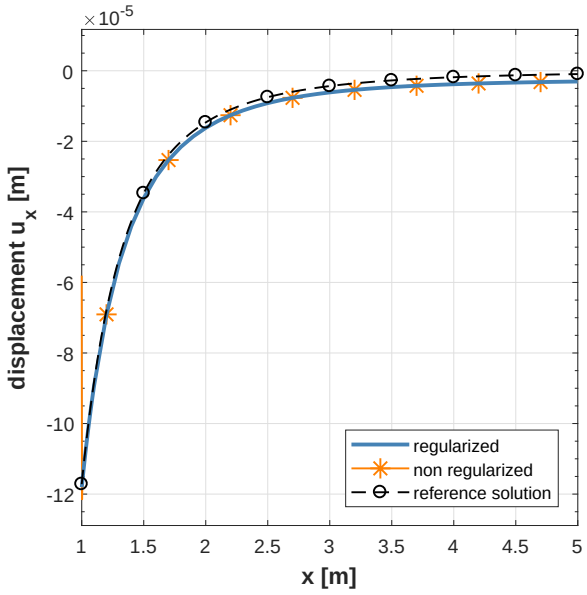

Fig. 56: displacement u_x along line $l*$

In the next figures the distributions of normal stresses σ_{xx} and σ_{yy} and displacements u_x are depicted for all meshes and for the first $0.1m$ along line l^* measured from the boundary ($1m \leq x \leq 1.1m$). Figure 57 shows numerical results obtained with the coarsest mesh ("mesh 1"), Figure 58 those obtained using "mesh 2" and Figure 59 depicts the same distributions for the finest mesh ("mesh 3"). For comparison, graphs of Kirsch's solutions are included as well.

Apart from the usual inaccuracies of non-regularized results, it can be seen that numerically computed normal stresses σ_{yy} and displacements u_x for each mesh slightly, but consequently, differ with the same order of magnitude from the reference solution while for all meshes numerically computed normal

stresses σ_{xx} agree very well with the reference solution. Nevertheless, the differences in σ_{yy} and u_x are very small and still acceptable. This also indicates that the highest level of accuracy already is achieved for the coarsest mesh and, obviously, integration and discretization errors play a minor role for the considered meshes since the quality of numerical results do not tend to improve for finer meshes. Furthermore, as already mentioned previously, this may prove that conditions at the corresponding region are not completely the ones of plain strain. This may be responsible for the small deviations between numerical and reference results. Only a longer tunnel with closed ends or the possibility of using infinite elements will cause that plane strain conditions are satisfied and the differences between numerical and reference results may decrease.

In the end it can be said that the quality of numerical results is very good and that the implemented code works for infinite domains, too. This means in particular, that the analytical solutions of the integrals over the boundary at infinity in Equations (12), (22) and (23) (Sections 2.3.2 and 2.3.4), which arise in the regularized SDI and SSI for infinite domains, are correct.

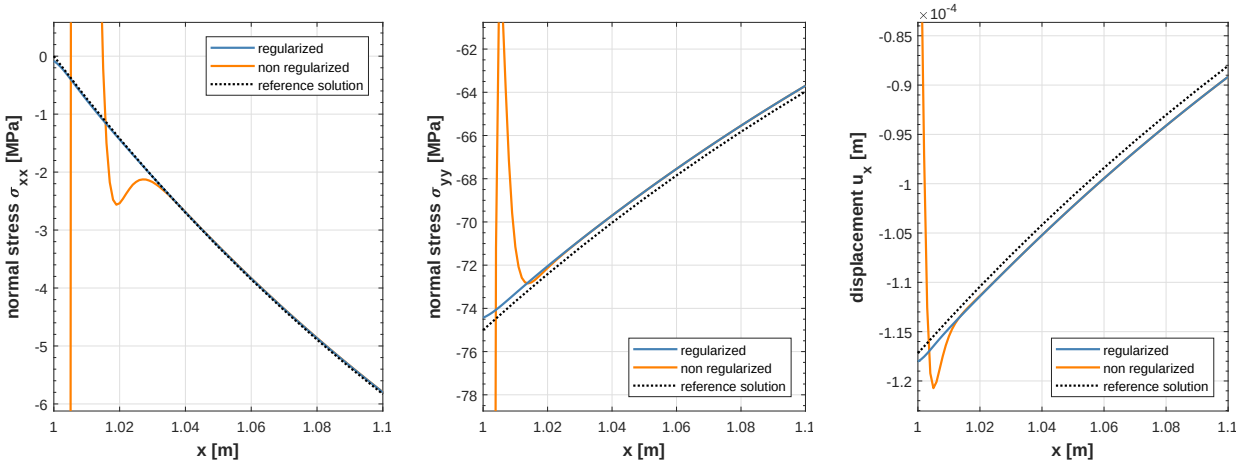

Fig. 57: "mesh 1" (coarsest mesh, 416 elements): normal stresses σ_{xx} and σ_{yy} and displacement u_x

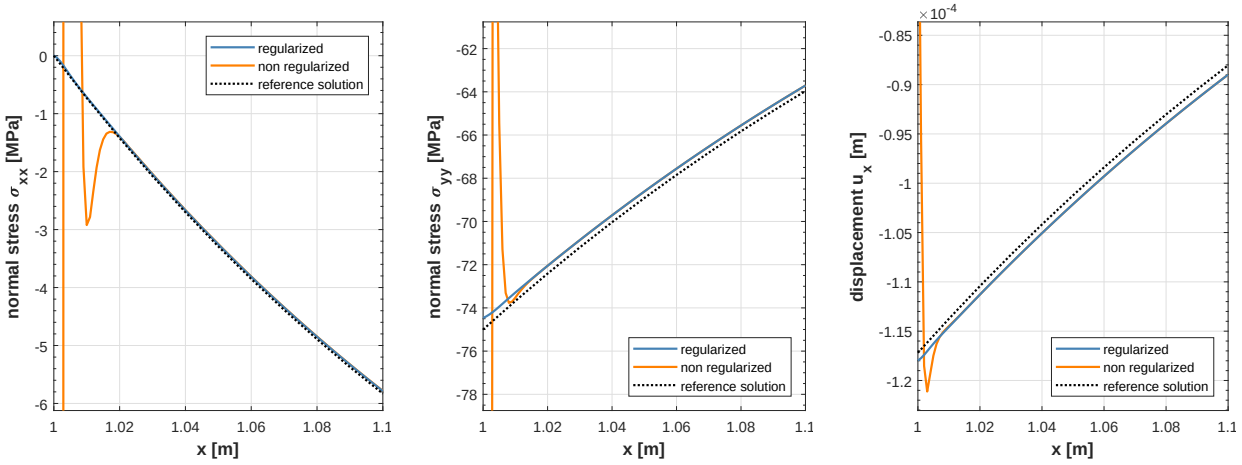

Fig. 58: "mesh 2" (736 elements): : normal stresses σ_{xx} and σ_{yy} and displacement u_x

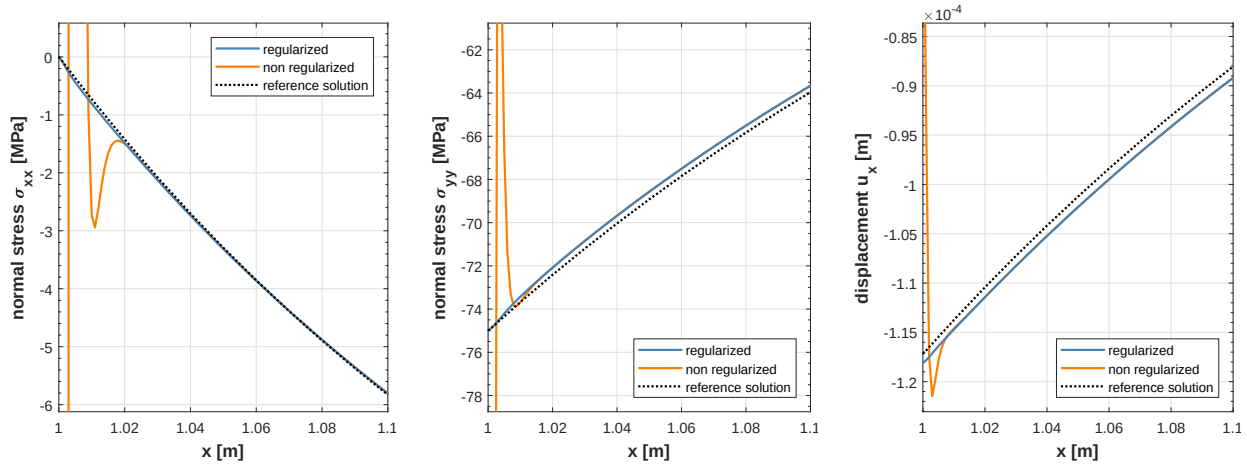

Fig. 59: "mesh 3" (finest mesh, 1472 elements): : normal stresses σ_{xx} and σ_{yy} and displacement u_x

4.4.5 Interior results along a circle very close around the tunnel

Following figures depicts numerical interior results obtained with the finest mesh ("mesh 3") and its corresponding reference solutions along the circle m^* with radius $r = 1.005m$ located at $z = z^* = 10m$ (orange dashed circle in Figure 44). Every interior point p on the circle m^* has the same constant and small distance from the tunnel surface. This thoroughly tests the implemented code whether it is working properly for interior points p located very close to the boundary. The distributions of normal and shear stresses σ_{xx}, σ_{yy} and τ_{xy} in terms of the angle θ are depicted in Figures 60, 61 and 62, respectively. Figures 63 and 64 show the displacement distributions u_x and u_y along the circle m^*.

First of all these figures clearly illustrates the influence of the different orders of singularities of the fundamental solutions on interior results obtained from the standard formulations of the SDI and SSI. The corresponding numerically computed interior displacement results agree very well with the reference solution whereas the stress results are no longer usable. This is because the singularity order of the fundamental solutions in the SSI ($\mathbf{S}$, $\mathbf{R}$) is one degree higher than that of their counterparts in the SDI ($\mathbf{U}$, $\mathbf{T}$). Therefore, for stresses more subelements than for displacements are required to achieve the same accuracy (see also Section 3.3.3). Note, the number of subelements in ξ- and η- direction was limited to 50 as for all previous examples. In this case the chosen element subdivision is still accurate for displacement results but provides inaccurate stress results. Whether the corresponding numerical displacement and stress results along the circle m^* are accurate or not could already be expected when comparing the corresponding results along the horizontal line l^* in Figure 59. The graphs in this figure clearly show that displacements u_x obtained from the standard formulation of the SDI at $x = r = 1.005m$ are still accurate and so they are along the circle m^*, while the normal stresses σ_{xx} and σ_{yy} obtained from the standard formulation of the SSI are already inaccurate at $x = r = 1.005m$ which also occur for those stresses along the circle m^*. On the contrary, results computed with the regularized forms of the Somigliana Identities are accurate for stresses and displacements and they agree very well with the reference solution. Thus, in this case it is inevitable to apply the regularized formulation of the Somigliana Identities in order to achieve accurate numerically computed stress results and also displacements if the radius r is chosen to be even smaller.

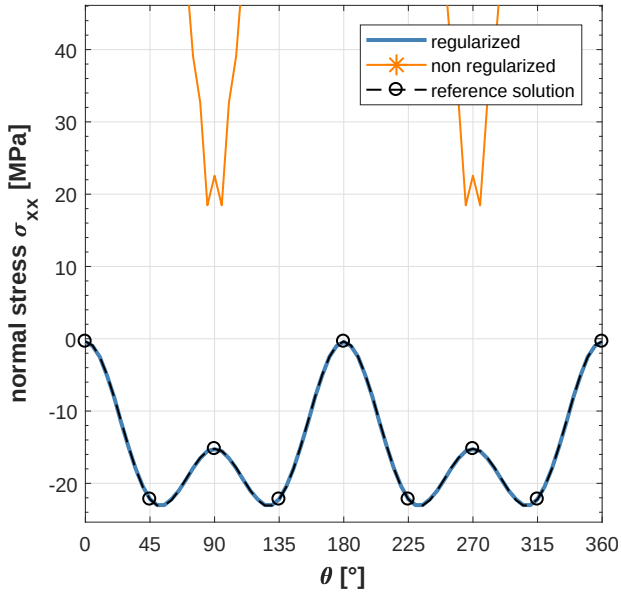

Fig. 60: normal stress σ_{xx} along circle m^*

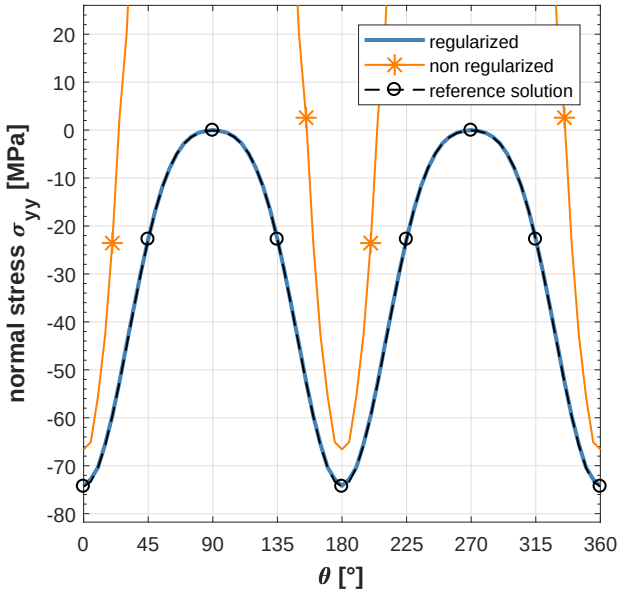

Fig. 61: normal stress σ_{yy} along circle m^*

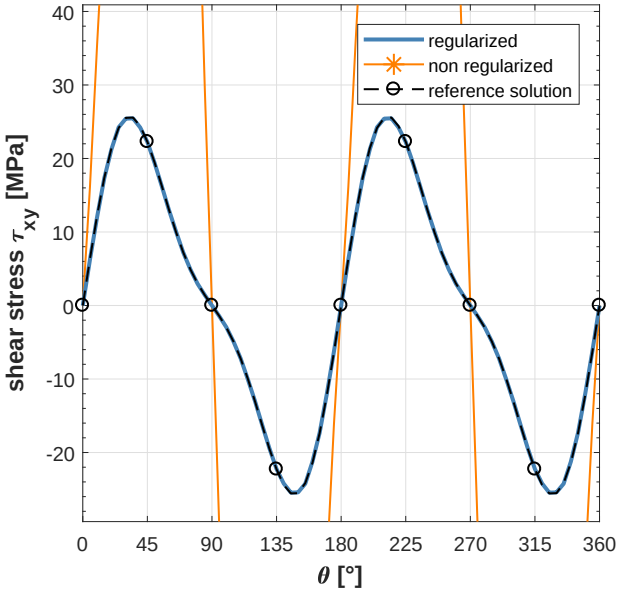

Fig. 62: shear stress τ_{xy} along circle m^*

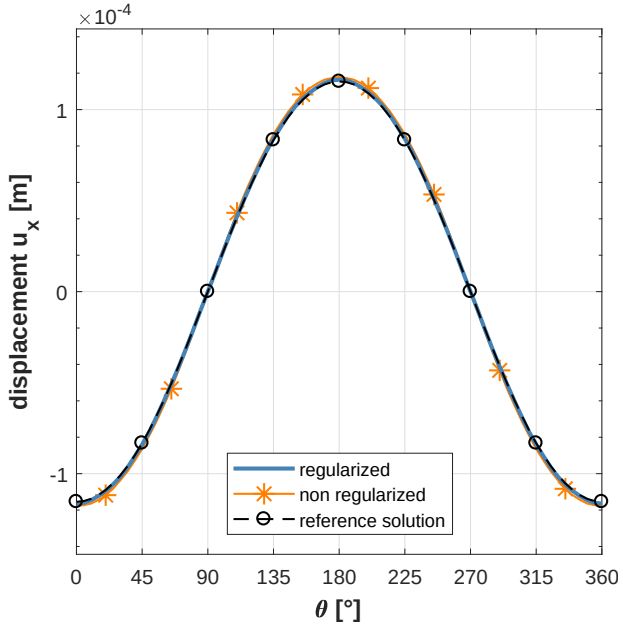

Fig. 63: displacement u_x along circle $m*$

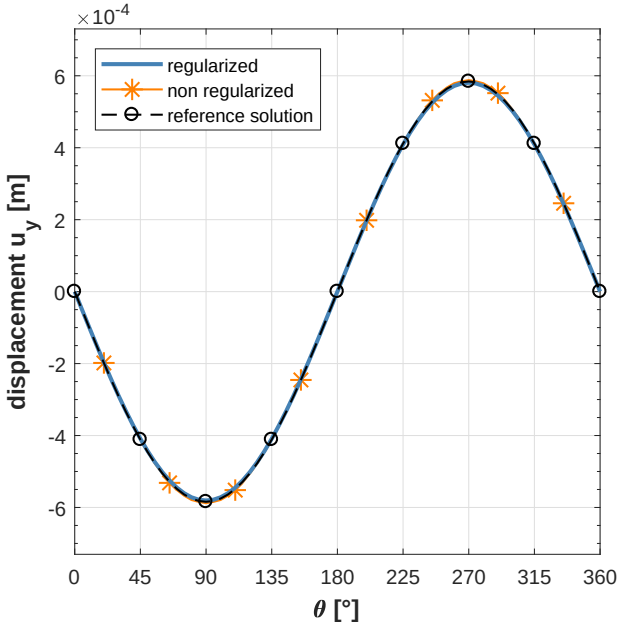

Fig. 64: displacement u_y along circle $m*$

4.4.6 Complementary results

In addition to results having already discussed in this example displacement and stress fields in the surrounding rock mass and at the boundary of the tunnel are illustrated in the next figures. They convey a better understanding of how excavation induced displacements and stresses behave around the tunnel. Therefore, a cross-section at $z = 10m$ and a longitudinal section along the tunnel axis (z-axis) for computing interior results with the regularized formulations of the Somigliana Identities are defined. Moreover, only half the length ($z \geq 10m$) and half the cross-section ($90° \leq \theta \leq 270°$) of the tunnel is displayed due to symmetry. Numerical results were calculated using the finest mesh ("mesh 3"). The displacement fields u_x and u_y are depicted in Figures 65 and 66, respectively. Figures 67, 68 and 69 provide the normal stress fields σ_{xx} and σ_{yy} and the shear stress field τ_{xy}.

Where recognizable, at the transition from the boundary to the interior of the domain contour lines (isolines) of the cross-section and the longitudinal section coincide with those of the boundary. This again shows how accurate interior results near the boundary can be computed when applying the regularized Somigliana Identities provided that already boundary results are accurate. Note, also the singular stress behaviour of normal stresses σ_{xx} and σ_{yy} at the corners of the closed tunnel ends can be seen clearly in Figures 67 and 68. It already occurs for boundary results and thus continuing for interior results.

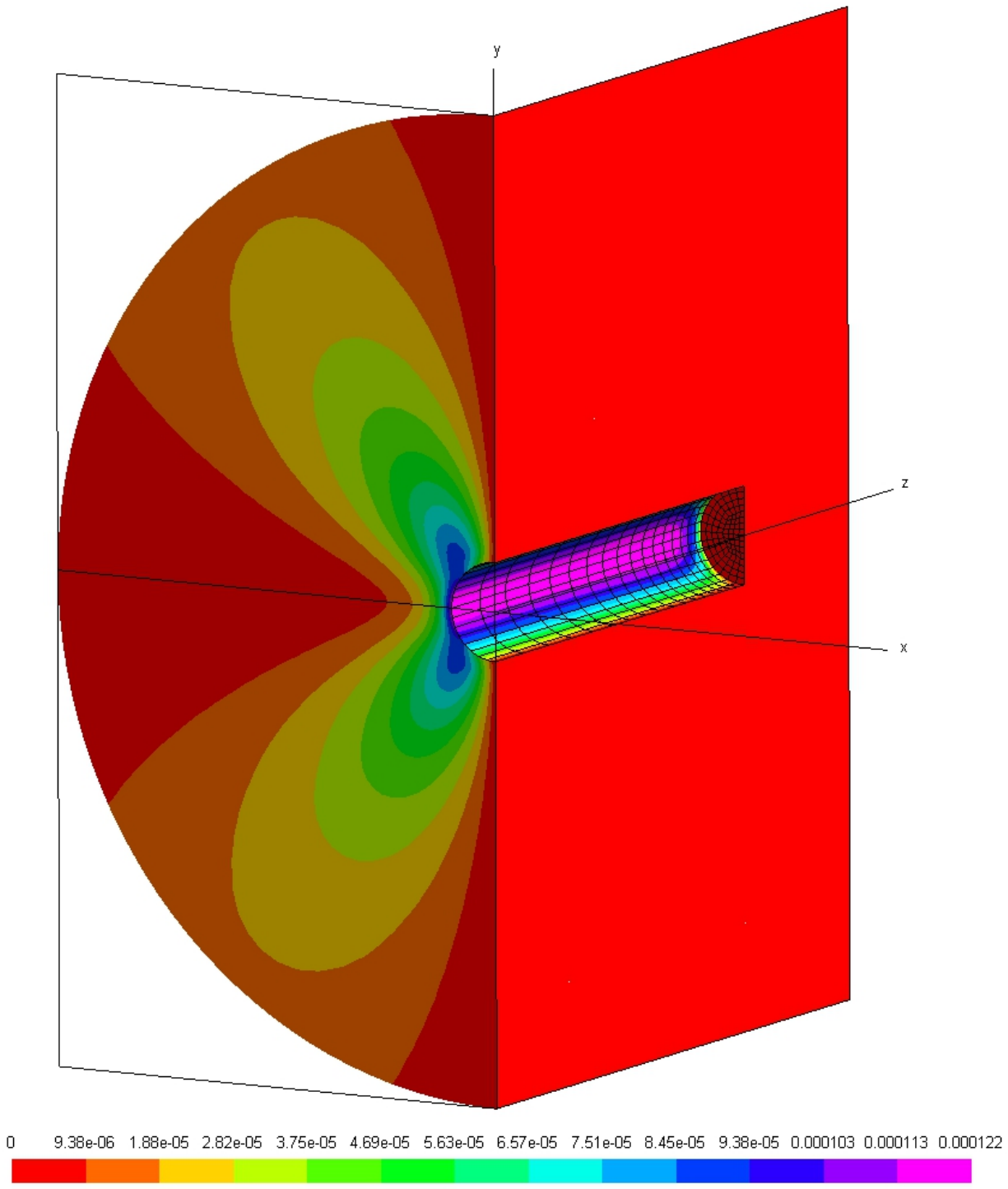

Fig. 65: displacement field u_x [m]

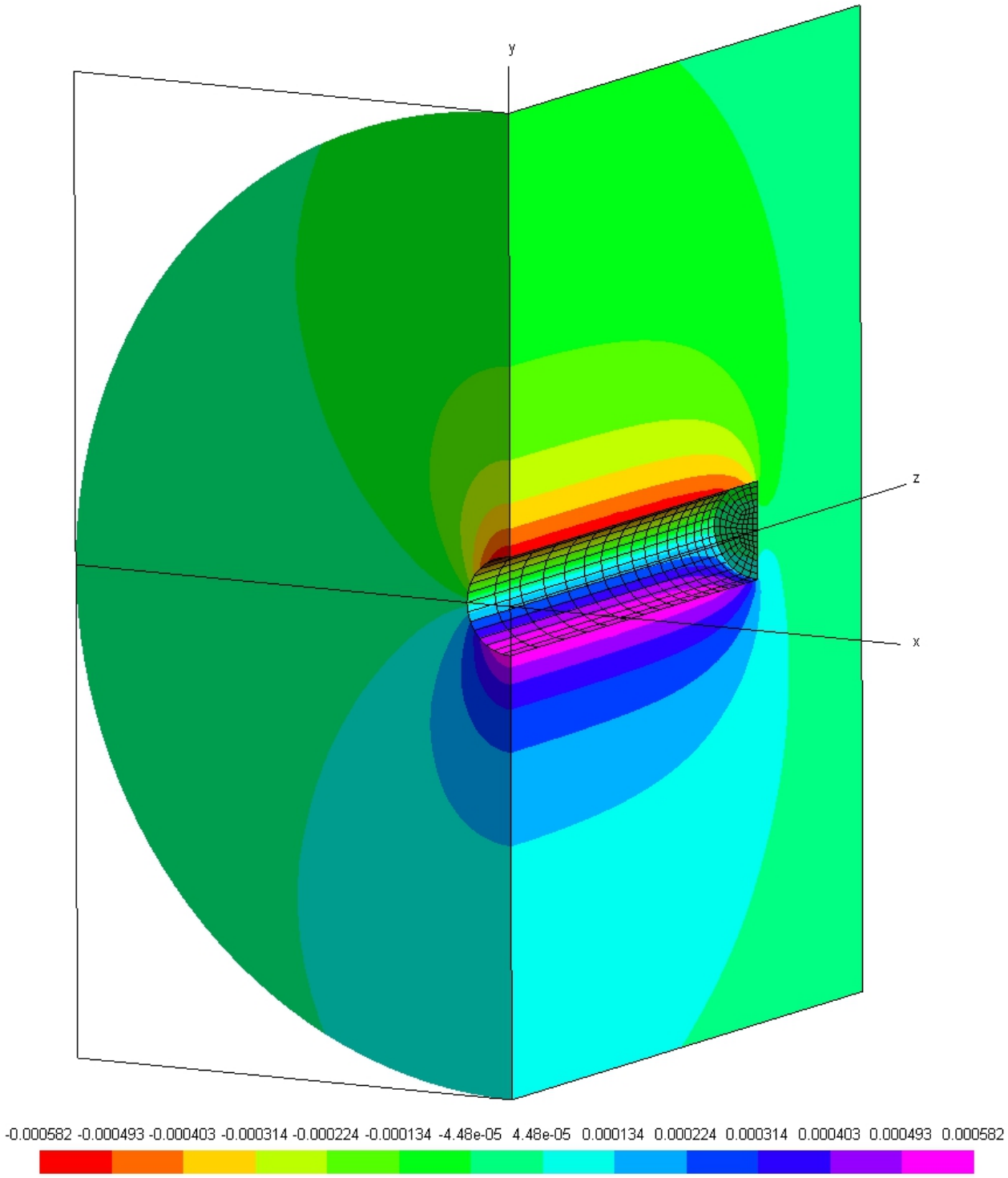

Fig. 66: displacement field u_y [m]

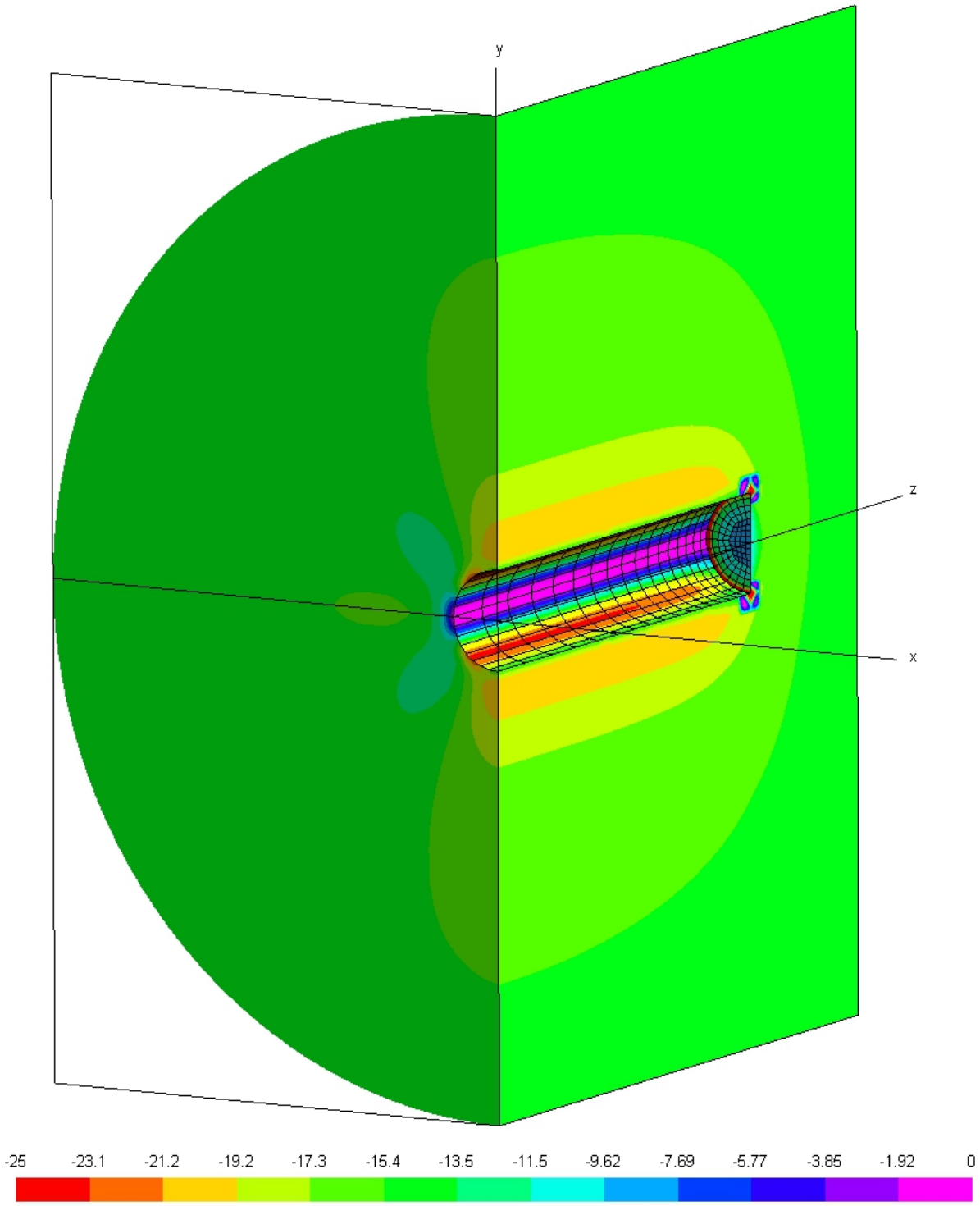

Fig. 67: normal stress field σ_{xx} [MPa]

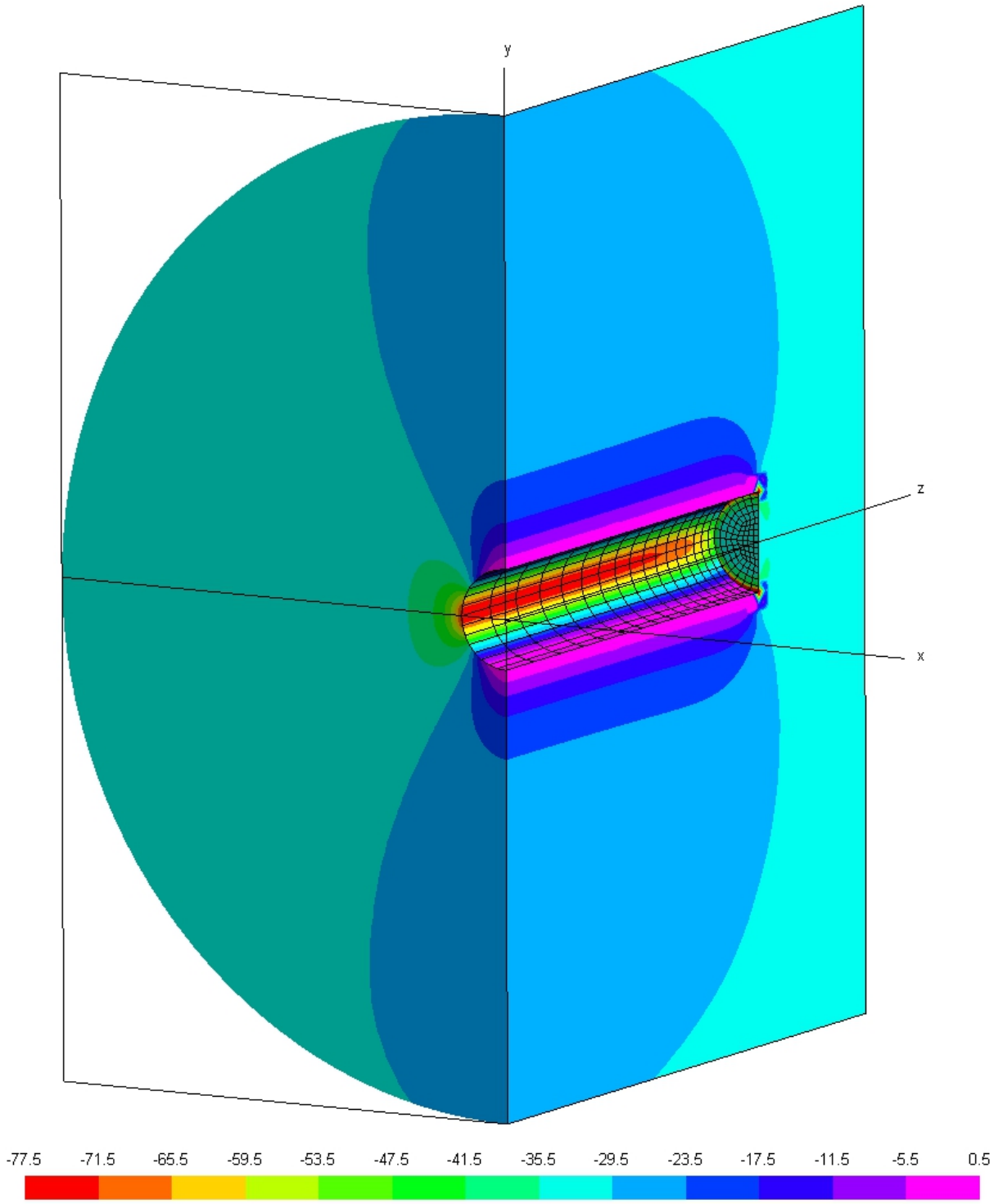

Fig. 68: normal stress field σ_{yy} [MPa]

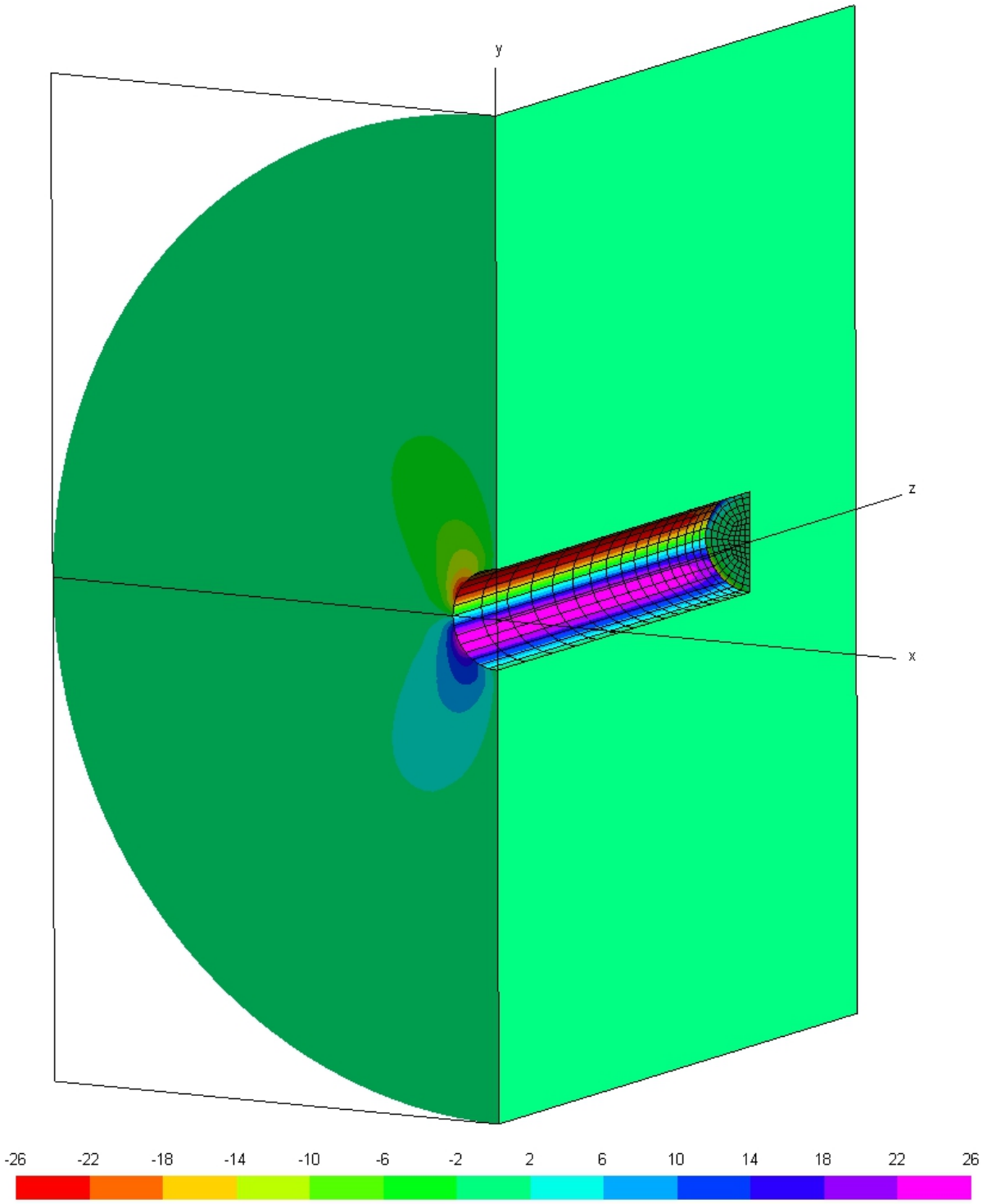

Fig. 69: shear stress field τ_{xy} [MPa]

5 Concluding remarks

The main aim of the present work was to study how regularization of the nearly singular Somigliana Displacement and Stress Identities for 3-D elasticity problems improve interior results at points close to the boundary. Therefore, numerical results obtained with the developed BEM-application were discussed by four examples. For comparison, numerical results with the standard formulations of the Somigliana Identities were calculated, too. The relevant integral equations including the Displacement Boundary Integral Equation and its discretizations were described and explained.

The numerical results of the examples investigated in this work clearly illustrates the difference between the regularized and non-regularized (standard) formulations of the nearly singular Somigliana Displacement and Stress Identities. Provided that already boundary results are sufficiently accurate, interior results near the boundary obtained from the regularized formulations show very high accuracy and excellent stability as expected. On the contrary, interior results obtained from the non-regularized formulations near the boundary are very inaccurate and therefore useless. Thus, it is inevitable applying regularization to obtain accurate results close to the boundary. The reason for the excellent accuracy and stability of interior results near the boundary obtained from the regularized Somigliana Identities is that regularization almost eliminates the impact of the nearly singular integrals of the standard Somigliana Identities. Moreover, numerical integration of the regularized formulations of the Somigliana Displacement and Stress Identity requires no special integration scheme as it does for the standard formulations. This makes the implementation much easier. The only additional expense is the determination of the regularizing point P on the boundary and its displacements, strains and stresses which in particular leads to increasing computation times.
The results of the examples also show no significant difference between both formulations when they are obtained at points with a sufficient great distance away from the boundary. Thus, regularization of the nearly singular Somigliana Identities may only be applied for results close to the boundary when element subdivision for the standard formulations would be necessary. All other interior results may be obtained from the standard formulations of the Somigliana Identities to make computation more efficient. This approach would combine the advantages of both formulations of the Somigliana Identities, namely accurate results near the boundary and decreasing computation times.
It also can be found from the examples that displacements usually converging better than stresses. This is because boundary displacements are evaluated directly from the displacement BIE, whereas boundary stresses are recovered by means of Hook's law from boundary displacements and tractions and thus becoming more inaccurate. Convergence of stresses may be improved by applying the stress BIE (or its regularized formulation) to compute boundary stresses directly.

References

[1] *Allplan v.2015 (student license), Nemetschek Group, Konrad-Zuse-Platz 1, 81829 München, Germany.* URL: https://www.nemetschek.com/en/.

[2] F.E.S. Anacleto et al. "An object oriented tridimensional self-regular boundary element method implementation". In: *Engineering Analysis with Boundary Elements* 37 (2013), pp. 1276–1284.

[3] G. Beer, I. Smith, and Ch. Dünser. *The Boundary Element Method with Programming.* 2008.

[4] T.A. Cruse and J.D. Richardson. "Non-Singular Somigliana Stress identities in Elasticity". In: *International Journal for Numercial Methods in Engineering.* 39 (1996), pp. 3273–3304.

[5] T.A. Cruse and W. Suwito. "On the Somigliana stress identity in elasticity". In: *Computational Mechanics* 11 (1993), pp. 1–10.

[6] L. Gaul, M. Kögl, and M. Wagner. *Boundary Element Methods for Engineers and Scientists. An Introductory Course with Advanced Topics.* 2003.

[7] C. Geuzaine and J.-F. Remacle. "Gmsh: a three-dimensional finite element mesh generator with built-in pre- and post-processing facilities". In: *International Journal for Numerical Methods in Engineering* 79(11) (2009), pp. 1309–1331.

[8] J.C. Lachat and J.O. Watson. "Effective numerical treatment of boundary integral equations: a formulation for three-dimensional elastostatics". In: *International Journal for Numercial Methods in Engineering.* 10 (1976), pp. 991–1005.

[9] *Latex, The Latex Project. Mainz, Germany.* URL: https://www.latex-project.org/.

[10] *MATLAB and Statistics Toolbox Release 2017b, The MathWorks, Inc., Natick, Massachusetts, United States.* URL: https://de.mathworks.com/products/matlab.html?s_tid=hp_products_matlab.

[11] C. Somigliana. "Sopra l'equilibrio di un corpo elastico isotropo". In: *Il nuovo cimento* 3 (1885/86), pp. 17–20.